INVESTIGATION OF ADVANCED LIGHT TRAPPING CONCEPTS FOR PLASMA-DEPOSITED SOLID PHASE CRYSTALLISED POLYCRYSTALLINE SILICON THIN-FILM SOLAR CELLS ON GLASS

YING HUANG

NATIONAL UNIVERSITY OF SINGAPORE

2014

INVESTIGATION OF ADVANCED LIGHT TRAPPING CONCEPTS FOR PLASMA-DEPOSITED SOLID PHASE CRYSTALLISED POLYCRYSTALLINE SILICON THIN-FILM SOLAR CELLS ON GLASS

YING HUANG

(M.Sc., NTU)

A THESIS SUBMITTED

FOR THE DEGREE OF DOCTOR OF PHILOSOPHY

DEPARTMENT OF ELECTRICAL AND COMPUTER ENGINEERING
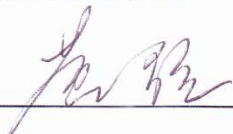
NATIONAL UNIVERSITY OF SINGAPORE

2014

DECLARATION

I hereby declare that the thesis is my original work and it has been written
by me in its entirety.

I have duly acknowledged all the sources of information which have been
used in this thesis.

This thesis has also not been submitted for any degree in any university
previously.

Name: YING HUANG

Signature: _____

Date: 12 May 2014

Acknowledgements

Table of Contents

Abstract

Effective light trapping is vital for polycrystalline silicon (poly-Si) thin-film solar cells on glass. This thesis aims to develop a light trapping system to enable a short-circuit current density (J_{SC}) of over 30 mA/cm^2 for plasma-deposited solid phase crystallized (SPC) poly-Si thin-film solar cells on glass.

Highly scattering aluminium-induced texture (AIT) glass sheets are successfully produced on pilot line-scale (30 cm × 40 cm) with good optical uniformity (non-uniformity < ± 2.5 %). By introducing a double diffusion barrier (silicon nitride and silicon dioxide) and by increasing the amorphous silicon (a-Si:H) precursor diode deposition temperature from 500 °C to 550 °C, an average 1-Sun open-circuit voltage (V_{OC}) of 484 mV and an average pseudo fill factor (*pFF*) of 78.2 % for 2 μm thick poly-Si thin-film solar cells on pilot line-scale AIT glass are achieved.

The solid state reaction between aluminium and borosilicate glass at an annealing temperature of about 500 °C is studied in detail. Crystalline silicon (c-Si) clusters are found to form on the glass surface and the c-Si clusters are surrounded by aluminium oxide (Al_2O_3). Crater shaped nodules, mainly consisting of Al_2O_3, are embedded in the glass. By adjusting the Al deposition thickness and/or annealing temperature, the Al_2O_3 nodules' size, depth and lateral separation can be controlled. As a result, the AIT glass texturing method can be further optimized.

A phase model based on the scalar scattering theory is demonstrated to be able to accurately estimate the haze and angular intensity distribution (AID) of rough

surfaces in poly-Si thin-film solar cells on textured glass superstrates. By combining the scalar scattering theory with the ASA thin-film solar cell simulator, the parasitic glass absorption and the c-Si absorption for poly-Si thin-film solar cells on textured glass can be separately estimated. The one-sun current density is estimated to increase by 7.3 % if the glass is thinned from 3.3 to 0.3 mm, assuming a 3 μm thick c-Si film on AIT glass and a stack of silicon dioxide and aluminium as the back surface reflector. Using the optical simulation method proposed in this thesis, the light trapping performance of poly-Si thin-film solar cells on textured glass can be evaluated more accurately.

A highly scattering rear Si surface texture is realized by plasma etching of poly-Si thin-film solar cells on glass. The resulting rear Si texture (RST) shows reflection haze values of more than 95 % at the Si-air interface. The poly-Si thickness consumed by plasma etching is estimated to be around 500 nm for this texture. The average feature size of the texture is around 200 nm. Combining this sub-micron RST with a micrometre-scale AIT glass texture can produce a multi-scale rear Si surface texture. The multi-scale rear Si surface texture can enhance the J_{SC} by 3 - 5 %, based on ASA optical simulation results.

By incorporating the AIT glass texture, a plasma-etched RST, a thinner glass sheet (0.5 mm), and a high-quality back surface reflector (a stack of silicon dioxide and silver), a 2 μm thick poly-Si thin-film solar cell on glass is shown to have a J_{SC} potential of 31 mA/cm^2.

List of Tables

List of Figures

List of Symbols

α	absorption coefficient
A	absorptance
d	physical thickness of glass
E_a	activation energy
H_T	transmission haze
H_R	reflection haze
I_0	intensity of incident light
I_{SC}	short-circuit current
J_{SC}	short-circuit current density
J_{ph}	current density
FF	fill factor
pFF	pseudo fill factor
λ	wavelength
n	real part of refractive index
κ	imaginary part of refractive index
k	Boltzmann constant
r	Fresnel reflectivity
R	reflectance
T	temperature
T	transmittance
V_{OC}	open-circuit voltage

Chapter 1   Introduction

1.1   Motivation for solar cells

Energy from the Sun ('solar energy') is abundant (over 165,000 TW reach the Earth's upper atmosphere) and available for every country and person in the world for free. Photovoltaic (PV) devices, or solar cells, generate electricity directly from sunlight. Figure 1-1 shows that solar cell production in 2011 was about 184 times higher than in 1999. A recent study by the European Photovoltaic Industry Association (EPIA) showed that the total deployed solar electric capacity had reached more than 100 GW by the end of 2012. As a green and renewable alternative to the conventional fossil fuel based electricity generation, PV has a bright future.
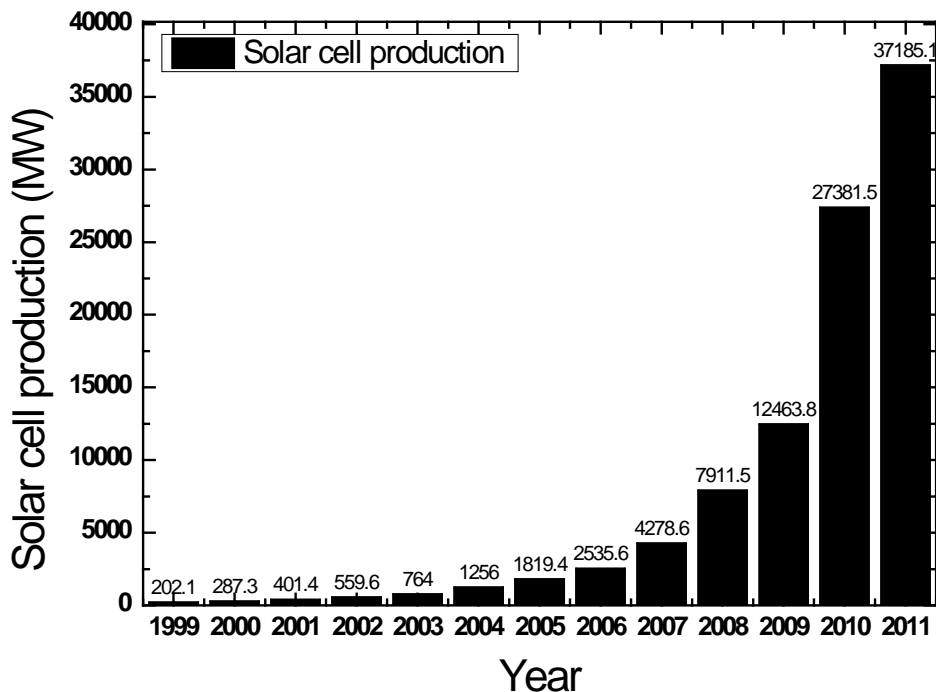
Figure 1-1: Yearly world solar cell production from 1999 to 2011. From Ref. [1].

1.2 Thin-film solar cell technologies

Among all the solar cell technologies, solar cells fabricated with crystalline silicon (c-Si) wafers had a market share of about 88 % in 2011 [1]. Almost a half of c-Si PV module fabrication cost was due to the starting material, i.e., the unprocessed Si wafers [2]. One possible path towards further improving the cost effectiveness of PV electricity is thin-film solar cells, as these use much less semiconductor material than wafer based technologies [3].

There are several types of thin-film solar cells in commercial production. The first is based on amorphous silicon (a-Si) and was introduced by Carlson in 1974 [4]. Amorphous silicon is cheap and with high absorption coefficient. However, it is difficult for the large scale a-Si PV module to reach stabilized efficiency above 10% due to light-induced degradation [5]. Another important Si thin-film solar cells technology is 'micromorph' tandem solar cell proposed by University of Neuchatel [6], which stacks one a-Si thin-film solar with a microcrystalline silicon (μc-Si) thin-film solar cell. Stabilized PV module efficiency above 11% was achieved for this technology [8, 41]. One weakness of this technology is the high capital cost of the deposition tool for the μc-Si [3].

Presently, the commercially most successful thin-film solar cell technology is cadmium telluride (CdTe) [7]. First Solar Inc, USA, is the largest CdTe PV module manufacturer in the world, with a production capacity of over 1 GW per year. At the pilot scale, the company has reported modules with an area of 7200 cm^2 reaching efficiencies of up to 16.1 % in 2012 [8]. The main limitations of this

technology are that Cd is a very toxic material and Te is a scarce material on earth [9].

Another promising thin-film PV technology is copper indium gallium selenide (CIGS). CIGS solar cells with efficiencies of more than 20 % have been made by both the National Renewable Energy Laboratory (NREL) and the Zentrum für Sonnenenergie und Wasserstoff-Forschung (ZSW), which is the record to date for any single-junction thin-film solar cell [10, 11]. The best CIGS module was reported by Miasole, USA. The company demonstrated 15.7 % module efficiency on a 0.97-m^2 glass substrate [8]. Despite the high efficiency potential and the relatively low manufacturing cost, CIGS PV industry expansion could be limited by the scarcity of indium (In) [9].

Perovskite compound thin-film solar cells are a rapidly emerging thin-film PV technology. Perovskite material was first used to make solar cells in 2009, giving efficiency of up to 3.5 %, as reported by Kojima *et al.* in 2009 [12]. In two Nature papers published in 2013, authors from two different research groups demonstrated perovskite thin-film solar cells with an efficiency of 15% [13, 14]. When a new semiconductor material is introduced to make solar cells, it usually takes more than a decade for researchers to improve the efficiency to 15%. Hence, the rate of efficiency improvement of the perovskite solar cell technology is impressive. Moreover, the material cost and process cost of perovskite solar cells are low. It is said that this technology could lead to solar panels that cost just US$ 0.10-0.20/W [15].

Due to their inherent advantages, thin-film solar cells are the 'holy grail' of photovoltaics. However, a lot of R&D is still required to develop these technologies

further and to bring them to a level where they can compete, and possibly even displace, silicon wafer based PV technologies. This thesis tries to contribute to this international effort, by investigating polycrystalline silicon thin-film solar cells on glass.

1.3 Polycrystalline Si thin-film solar cells

The polycrystalline Si (poly-Si) thin-film solar cell technology is another important thin-film PV technology. Compared to the above mentioned thin-film technologies, poly-Si PV technology can combine the advantages of the silicon wafer-based technology, namely Si abundance, mature technology, environmental friendliness with the advantages of thin-film technology, mainly low material usage and cost [16-18]. Three technological methods to fabricate poly-Si thin-film solar cells on foreign substrates are described here: solid phase crystallization (Section 1.3.1), seed layer approach (Section 1.3.2), and liquid phase crystallization (Section 1.3.3).

1.3.1 Solid phase crystallization

The solid phase crystallization (SPC) process converts amorphous silicon (a-Si) to poly-Si by thermal annealing at around 600°C. Matsuyama *et al.* from Sanyo Electric Co. produced SPC poly-Si thin-film solar cells on metal substrates based on the plasma-enhanced chemical vapour deposition (PECVD) approach [19-21]. A remarkable efficiency of 9.7 % and a record open-circuit voltage (V_{oc}) of 553 mV for a SPC poly-Si thin-film solar cell based on the PECVD approach was

demonstrated in 1996 [21]. The record SPC poly-Si thin-film solar cell based on the PECVD approach was developed by CSG Solar, with an efficiency of 10.4 % demonstrated in 2007 [22]. SPC poly-Si thin-film solar cells on glass based on the electron beam (e-beam) evaporation approach were developed in UNSW [23-25]. Compared to PECVD with a typical a-Si deposition rate of 0.1-1 nm/s [26], e-beam evaporation has a much higher deposition rate (5-20 nm/s). However, the electronic quality of SPC films is drastically reduced when the films are deposited on textured glass sheets [27]. Therefore, the evaporation has to be done onto quasi-flat substrates and non-conventional light trapping techniques such as plasmonic nanoparticles at the Si rear surface [28] or Si rear surface texture [25] need to be applied. The best SPC poly-Si thin-film solar cell based on e-beam evaporation was developed by UNSW, with an efficiency of 7.1% demonstrated in 2011 [25].

1.3.2 Seed layer approach

The seed layer approach is based on first growing a very thin silicon seed layer with excellent crystallographic properties as a template and then transferring the structural information into the solar cell absorber material by epitaxial thickening. Aluminium induced crystallization (AIC) has attracted considerable interest in the PV community as a seed layer growth technique [29-32]. The highest V_{OC} of 534 mV [31] and the highest efficiency of 8.5% [32] for poly-Si thin-film solar cells relying on an AIC seed layer have been developed by IMEC, Belgium.

5

1.3.3 Liquid phase crystallization

In the past few years, the development of the silicon liquid phase crystallization (LPC) process has made substantial progress. The thermal budget inside the substrate is reduced by focusing the energy mainly into the silicon layer. LPC methods generally achieve much higher V_{OC} values than SPC methods. An impressive V_{OC} of 582 mV was recently achieved with an e-beam crystallized poly-Si thin-film solar cell [33]. A remarkable stabilized efficiency of 10.4 % for a laser-crystallized poly-Si thin-film solar cell on glass was demonstrated by UNSW in 2013 [34]. A very recent work [35] showed that it is possible to stabilize the efficiency of laser-crystallized poly-Si thin-film solar cells by applying laser firing to the rear point contacts of the solar cells. It is likely for LPC approaches to surpass 11 % efficiency in the near future.

1.4 The need for light trapping in poly-Si thin-film solar cells

One challenge for poly-Si thin-film solar cell is to achieve reasonably high short-circuit current density (J_{SC}), because thin silicon has quite weak absorption for near-infrared wavelengths. Figure 1-2 shows that a large fraction of the light in the 500-1100 nm wavelength range will escape from a 2 µm thick c-Si layer assuming a single pass of the incident light. For a 2 µm thick poly-Si thin-film solar cell grown on a planar glass sheet and with air as the back surface reflector (BSR), the J_{SC} is only 15.6 mA/cm^2 [36]. Assuming a V_{OC} of 500 mV and a fill

factor (*FF*) of 70%, this corresponds to an efficiency of 5.5 %, which is much lower than the efficiency limit of 19.8 % for a 1 µm thick c-Si cell [37].
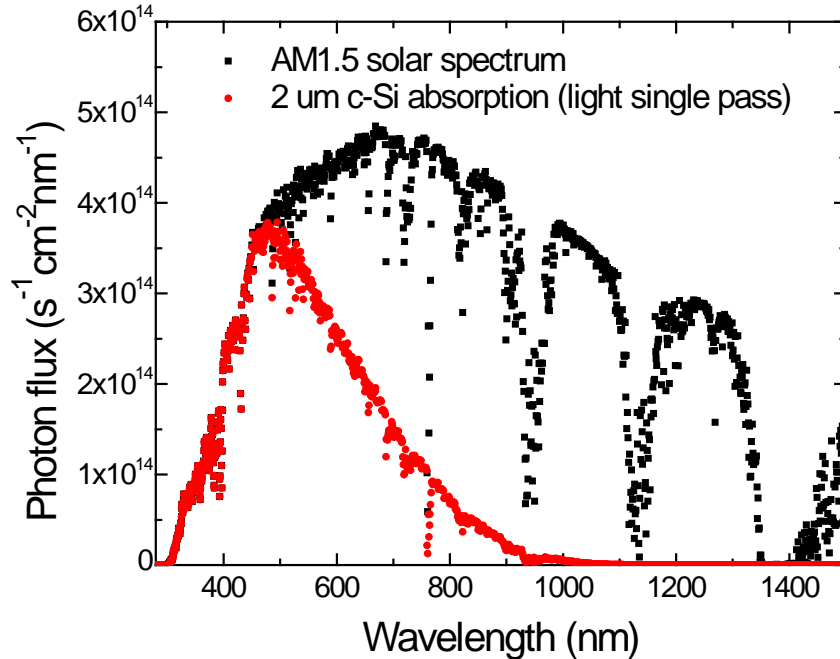
Figure 1-2: Photon flux absorbed by a 2 µm thick c-Si layer, assuming a single pass of the incident light. The AM1.5 solar spectrum is shown as the reference.

1.5   Scientific-technical problems addressed in this thesis

To enhance the optical absorptance in poly-Si thin-film solar cells on glass, light trapping methods have to be adopted which enhance the optical pathlength of weakly absorbed wavelengths inside the thin Si layer. Glass texturing [22, 38] and rear Si surface texturing [25] are two possible paths to achieve good light trapping inside the poly-Si thin-film layer. The aluminium (Al) induced glass texturing (AIT) process [39], which roughens the glass surface by annealing a thin layer of Al on glass and subsequent wet-chemical removal of the reaction

product, is a promising light trapping method for the poly-Si on glass thin-film PV technology.

To achieve good light trapping for poly-Si thin-film solar cells on glass, the research problems addressed in this thesis are:

- Scale up the AIT glass texturing process to pilot line scale glass sheets (> 30 cm × 30 cm).

- Develop a phenomenological model of the AIT process

- Establish an optical simulation method to evaluate the optical performance of poly-Si solar cells on AIT glass

- Investigate parasitic glass absorption for poly-Si thin-film solar cells on AIT glass

- Develop a rear Si surface texturization process by plasma etching. Integrate this rear surface texture with poly-Si solar cells deposited on AIT glass sheets.

1.6 Thesis organization

The structure of this thesis is as follows:

Chapter 1 introduces the motivation for solar cell devices. A brief review of the main thin-film solar cell technologies is given. Three main technological methods to produce poly-Si for poly-Si thin-film solar cells are introduced. The rationale for

implementing light trapping methods in poly-Si thin-film solar cells on glass sheets is given. The layout of the thesis is also described.

In **Chapter 2**, fabrication process flows of poly-Si thin-film solar cells on glass sheets used in our research group at the Solar Energy Research Institute of Singapore (SERIS) are described. Glass texturing and c-Si rear surface texturing methods which have been used for thin-film light trapping applications are briefly reviewed. The main processing equipment, characterization methods and thin-film solar cell simulator (ASA) used in this work are introduced.

Chapter 3 describes the baseline setup for the AIT process in our group at SERIS, using both Borofloat glass sheets from Schott AG, Germany, and boro-silicate glass sheets from a Chinese glass manufacturer (He Ping Glass, China [40]). The scalability of the AIT process to pilot-line scale for both kinds of glass sheets, with very good optical uniformity, is demonstrated. Optimization of the process conditions of poly-Si thin-film on pilot-line scale AIT glasses is described.

Chapter 4 presents a phenomenological model of the AIT glass texturing process. The redox reaction between aluminium (Al) and silicon dioxide (SiO_2) inside the glass sheet is studied in detail in this chapter.

Chapter 5 presents a phase model based on the scalar scattering theory to calculate two important scattering properties - haze and angular intensity distribution (AID) - of textured surfaces. Parasitic glass absorption and c-Si absorption is estimated by combining the phase model based on the scalar scattering theory and ASA optical simulations. The impact of the glass thickness on the short-circuit current loss due to the parasitic glass absorption is evaluated.

Chapter 6 is devoted to rear c-Si surface texturization by plasma etching. The prospect of applying c-Si rear surface texturization on poly-Si thin-film solar cells on AIT glass sheets to further enhance the short-circuit current density is demonstrated.

Chapter 7 summarises the work performed in this thesis, lists the original contributions made, and provides suggestions for further work for PECVD SPC poly-Si thin-film solar cells on glass.

References (Chapter 1)

[1] G. Hering, Cell production 2011 survey, Photon International, pp. 132-161, 2012.

[2] PV technology and Cost Outlook, 2013-2017, Available: http://www.greentechmedia.com/research/report/pv-technology-and-cost-outlook-2013-2017. (accessed on 05 December 2013).

[3] A.G. Aberle, Thin-film solar cells, Thin Solid Films, 517 (2009) 4706-4710.

[4] D.E. Carlson, Amorphous-silicon solar cells, Electron Devices, IEEE Transactions on, 36 (1989) 2775-2780.

[5] D.L. Staebler, C.R. Wronski, Reversible conductivity changes in discharge-produced amorphous Si, Applied Physics Letters, 31 (1977) 292-294.

[6] J. Meier, S. Dubail, R. Fluckiger, D. Fischer, H. Keppner, A. Shah, Intrinsic microcrystalline silicon (µc-Si:H) - A promising new thin film solar cell material, Proc. 1st WCPEC, (1994) 409-412.

[7] N. Rommel, Z. Ken, High-Efficiency CdTe and CIGS Thin-Film Solar Cells: Highlights and Challenges, in: Conference Record of the 2006 IEEE 4th World Conference on Photovoltaic Energy Conversion, 2006, pp. 317-320.

[8] M.A. Green, K. Emery, Y. Hishikawa, W. Warta, E.D. Dunlop, Solar cell efficiency tables (version 42), Progress in Photovoltaics: Research and Applications, vol. 21, pp. 827-837, 2013.

[9] C. Candelise, M. Winskel, R. Gross, Implications for CdTe and CIGS technologies production costs of indium and tellurium scarcity, Progress in Photovoltaics: Research and Applications, vol. 20, pp. 816-831, 2012.

[10] I. Repins, M.A. Contreras, B. Egaas, C. DeHart, J. Scharf, C.L. Perkins, B. To, R. Noufi, 19.9%-efficient ZnO/CdS/CuInGaSe2 solar cell with 81.2% fill factor, Progress in Photovoltaics: Research and Applications, vol. 16, pp. 235-239, 2008.

[11] P. Jackson, D. Hariskos, E. Lotter, S. Paetel, R. Wuerz, R. Menner, W. Wischmann, M. Powalla, New world record efficiency for Cu(In,Ga)Se2 thin-film solar cells beyond 20%, Progress in Photovoltaics: Research and Applications, vol. 19, pp. 894-897, 2011.

[12] A. Kojima, K. Teshima, Y. Shirai, T. Miyasaka, Organometal Halide Perovskites as Visible-Light Sensitizers for Photovoltaic Cells, Journal of the American Chemical Society, 131 (2009) 6050-6051.

[13] J. Burschka, N. Pellet, S.J. Moon, R. Humphry-Baker, P. Gao, M.K. Nazeeruddin, M. Grätzel, Sequential deposition as a route to high-performance perovskite-sensitized solar cells, Nature, 499 (2013) 316-319.

[14] M. Liu, M.B. Johnston, H.J. Snaith, Efficient planar heterojunction perovskite solar cells by vapour deposition, Nature, 501 (2013) 395-398.

[15] A Material That Could Make Solar Power "Dirt Cheap", Available: http://www.technology review.com/news/517811/a-material-that-could-make-solar-power-dirt-cheap (accessed on 06 Dec 2013).

[16] M.A. Green, P.A. Basore, N. Chang, D. Clugston, R. Egan, R. Evans, D. Hogg, S. Jarnason, M. Keevers, P. Lasswell, J. O'Sullivan, U. Schubert, A. Turner, S.R. Wenham, T. Young, Crystalline silicon on glass (CSG) thin-film solar cell modules, Solar Energy, 77 (2004) 857-863.

[17] A.G. Aberle, Progress with polycrystalline silicon thin-film solar cells on glass at UNSW, Journal of Crystal Growth, 287 (2006) 386-390.

[18] P.A. Basore, CSG-1: Manufacturing a new polycrystalline silicon PV technology, in: Conference Record of the 2006 IEEE 4th World Conference on Photovoltaic Energy Conversion, 2006, pp. 2089-2093.

[19] T. Matsuyama, K. Wakisaka, M. Kameda, M. Tanaka, T. Matsuoka, S. Tsuda, S. Nakano, Y. Kishi, Y. Kuwano, Preparation of High-Quality n-Type Poly-Si Films by the Solid Phase Crystallization (SPC) Method, Japanese Journal of Applied Physics, 29 (1990), pp. 2327 - 2331.

[20] T. Matsuyama, M. Tanaka, S. Tsuda, S. Nakano, Y. Kuwano, Improvement of n-type poly-Si film properties by solid phase crystallization method, Japanese Journal of Applied Physics, Part 1: Regular Papers and Short Notes and Review Papers, 32 (1993) 3720-3728.

[21] T. Matsuyama, N. Terada, T. Baba, T. Sawada, S. Tsuge, K. Wakisaka, S. Tsuda, High-quality polycrystalline silicon thin film prepared by a solid phase crystallization method, Journal of Non-Crystalline Solids, 198-200 (1996) 940-944.

[22] M. Keevers, T.L. Young, U. Schubert, R. Evans, R.J. Egan, M.A. Green, 10% Efficient CSG minimodules, in: 22nd European Photovoltaic Solar Energy Conference, Milan, 2007, pp. 1783.

[23] M.L. Terry, A. Straub, D. Inns, D. Song, A.G. Aberle, Large open-circuit voltage improvement by rapid thermal annealing of evaporated solid-phase-crystallized thin-film silicon solar cells on glass, Applied Physics Letters, 86 (2005) 172108.

[24] D. Song, D. Inns, A. Straub, M.L. Terry, P. Campbell, A.G. Aberle, Solid phase crystallized polycrystalline thin-films on glass from evaporated silicon for photovoltaic applications, Thin Solid Films, 513 (2006) 356-363.

[25] T. Soderstrom, Q. Wang, K. Omaki, O. Kunz, D. Ong, S. Varlamov, Light confinement in e-beam evaporated thin film polycrystalline silicon solar cells, Physica Status Solidi - Rapid Research Letters, 5 (2011) 181-183.

[26] G. Parascandolo, R. Bartlome, G. Bugnon, T. Söderström, B. Strahm, A. Feltrin, C. Ballif, Impact of secondary gas-phase reactions on microcrystalline silicon solar cells deposited at high rate, Applied Physics Letters, 96 (2010) 233508.

[27] H. Cui, P.R. Campbell, M.A. Green, Compatibility of glass textures with E-beam evaporated polycrystalline silicon thin-film solar cells, Applied Physics A: Materials Science and Processing, 111 (2013) 935-942.

[28] Z. Ouyang, S. Pillai, F. Beck, O. Kunz, S. Varlamov, K.R. Catchpole, P. Campbell, M.A. Green, Effective light trapping in polycrystalline silicon thin-film solar cells by means of rear localized surface plasmons, Applied Physics Letters, 96 (2010) 261109.

[29] P.I. Widenborg, A.G. Aberle, Surface morphology of poly-Si films made by aluminium-induced crystallisation on glass substrates, Journal of Crystal Growth, 242 (2002) 270-282.

[30] P.I. Widenborg, A. Straub, A.G. Aberle, Epitaxial thickening of AIC poly-Si seed layers on glass by solid phase epitaxy, Journal of Crystal Growth, 276 (2005) 19-28.

[31] I. Gordon, L. Carnel, D. Van Gestel, G. Beaucarne, J. Poortmans, 8% efficient thin-film polycrystalline-silicon solar cells based on aluminum-induced crystallization and thermal CVD, Progress in Photovoltaics: Research and Applications, 15 (2007) 575-586.

[32] Y. Qiu, O. Kunz, S. Venkatachalam, D. Van Gestel, R. Egan, I. Gordon, J. Poortmans, 8.5% efficiency for thin-film polycrystalline silicon solar cells: a study of hydrogen plasma passivation, in: the 25th European Photovoltaic Conference 2010, Valencia, Spain, 2010, pp. 3363.

[33] J. Haschke, L. Jogschies, D. Amkreutz, L. Korte, B. Rech, Polycrystalline silicon heterojunction thin-film solar cells on glass exhibiting 582 mV open-circuit voltage, Solar Energy Materials and Solar Cells, 115 (2013) 7-10.

[34] J. Dore, D. Ong, S. Varlamov, R. Egan, M.A. Green, Progress in Laser-Crystallized Thin-Film Polycrystalline Silicon Solar Cells: Intermediate Layers, Light Trapping, and Metallization, IEEE Journal of Photovoltaics, 4 (2013) 33-39.

[35] M. Weizman, H. Rhein, J. Dore, S. Gall, C. Klimm, G. Andrä, C. Schultz, F. Fink, B. Rau, R. Schlatmann, Efficiency and stability enhancement of laser-crystallized polycrystalline silicon thin-film solar cells by laser firing of the absorber contacts, Solar Energy Materials and Solar Cells, 120, Part B (2014) 521-525.

[36] Z. Ouyang, Electron-Beam Evaporated Polycrystalline Silicon Thin-film Solar Cells: Paths to Better Performance, PhD thesis, The University of New South Wales, Sydney, 2011.

[37] M.A. Green, Limiting efficiency of bulk and thin-film silicon solar cells in the presence of surface recombination, Progress in Photovoltaics: Research and Applications, 7 (1999) 327-330.

[38] G. Jin, P.I. Widenborg, P. Campbell, S. Varlamov, Lambertian matched absorption enhancement in PECVD poly-Si thin film on aluminum induced textured glass superstrates for solar cell applications, Progress in Photovoltaics: Research and Applications, 18 (2010) 582-589.

[39] A.G. Aberle, P.I. Widenborg, N. Chuangsuwanich, Glass texturing, European Patent EP1613562B1, 2011.

[40] Available: http://www.hepingglass.com/ (accessed on 06 Dec 2013).

[41] A. Lambertz, T. Grundler, F. Finger, Hydrogenated amorphous silicon oxide containing a microcrystalline silicon phase and usage as an intermediate reflector in thin-film silicon solar cells, Journal of Applied Physics, 109 (2011), 113109.

Chapter 2   Experimental

2.1   Introduction

In this chapter, the fabrication procedure used at SERIS for poly-Si thin-film solar cells on glass is introduced (Section 2.2). This is followed by a brief review of the various glass texturing methods (Section 2.3.1) and Si texturing methods (Section 2.3.2). Two important parameters to describe the optical scattering efficiency of rough surfaces - haze and angular intensity distribution (AID) - are introduced in Section 2.4.1. Various optical models adopted to calculate surface scattering properties are briefed in Section 2.4.2. This is followed by an intro-duction to a commercial thin-film solar cell simulator ASA (Section 2.4.3) and the main characterization methods (Section 2.5) used in this thesis.

2.2 Fabrication procedure of poly-Si thin-film solar cells on glass at SERIS

2.2.1 Poly-Si fabrication and treatment

In our research group at SERIS, we use a similar approach as that of CSG Solar [1] to fabricate poly-Si thin-film solar cells on glass. Plasma-enhanced chemical vapour deposition (PECVD) is used to deposit an amorphous Si (a-Si:H) pre-cursor diode and then to crystallize this diode using the solid phase crystallization (SPC) method [2]. Figure 2-1 is a schematic drawing of a PECVD SPC poly thin-film solar cell on a planar glass sheet. The commercially available 3.3 mm thick borosilicate glass sheets (30×40 cm^2, planar) are cleaned in a glass washer. The glass sheets are then coated with ~ 70 nm of silicon nitride (SiN_x). The SiN_x layer serves as both a diffusion barrier and an anti-reflection coating [3]. After the SiN_x deposition, an 1-3 μm thick a-Si:H $n^+/p^-/p^+$ diode is deposited by PECVD. The details of the a-Si:H diode PECVD deposition can be found in Ref. [4]. The a-Si:H diode then undergoes solid phase crystallization in a nitrogen purged oven at 600 °C for 12 hours [5-7], followed by 1 minute of rapid thermal processing (RTP) at 1050 °C [4] to activate dopants and anneal defects, and finally a hydrogen passivation in a microwave powered plasma [8].
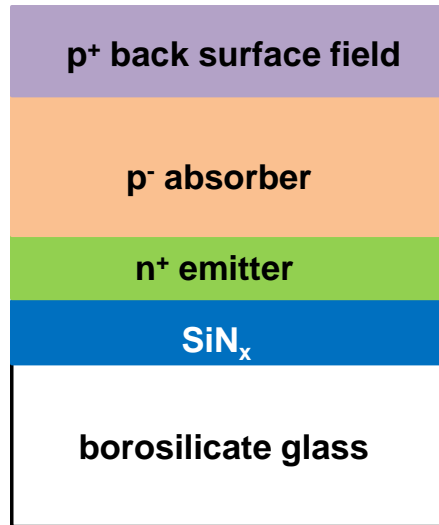
Figure 2-1: Schematic structure of a PECVD SPC poly-Si thin-film solar cell on a planar glass sheet. Note that the structure is presented upside down (i.e., it is illuminated from the bottom).

2.2.2 Metallization

An interdigitated metallization scheme developed in UNSW [9, 10] is used by our group. A schematic representation of the metallization method is shown in Figure 2-2. The aluminium (Al) above the silicon dioxide serves as the rear (i.e., air side) electrode of the cell, which is in contact with the p$^+$ back surface field. The Al deposited inside the grove serves as the front electrode of the cell, which is in contact with the n$^+$ emitter. The details of the metallization process can be found in Ref. [11].
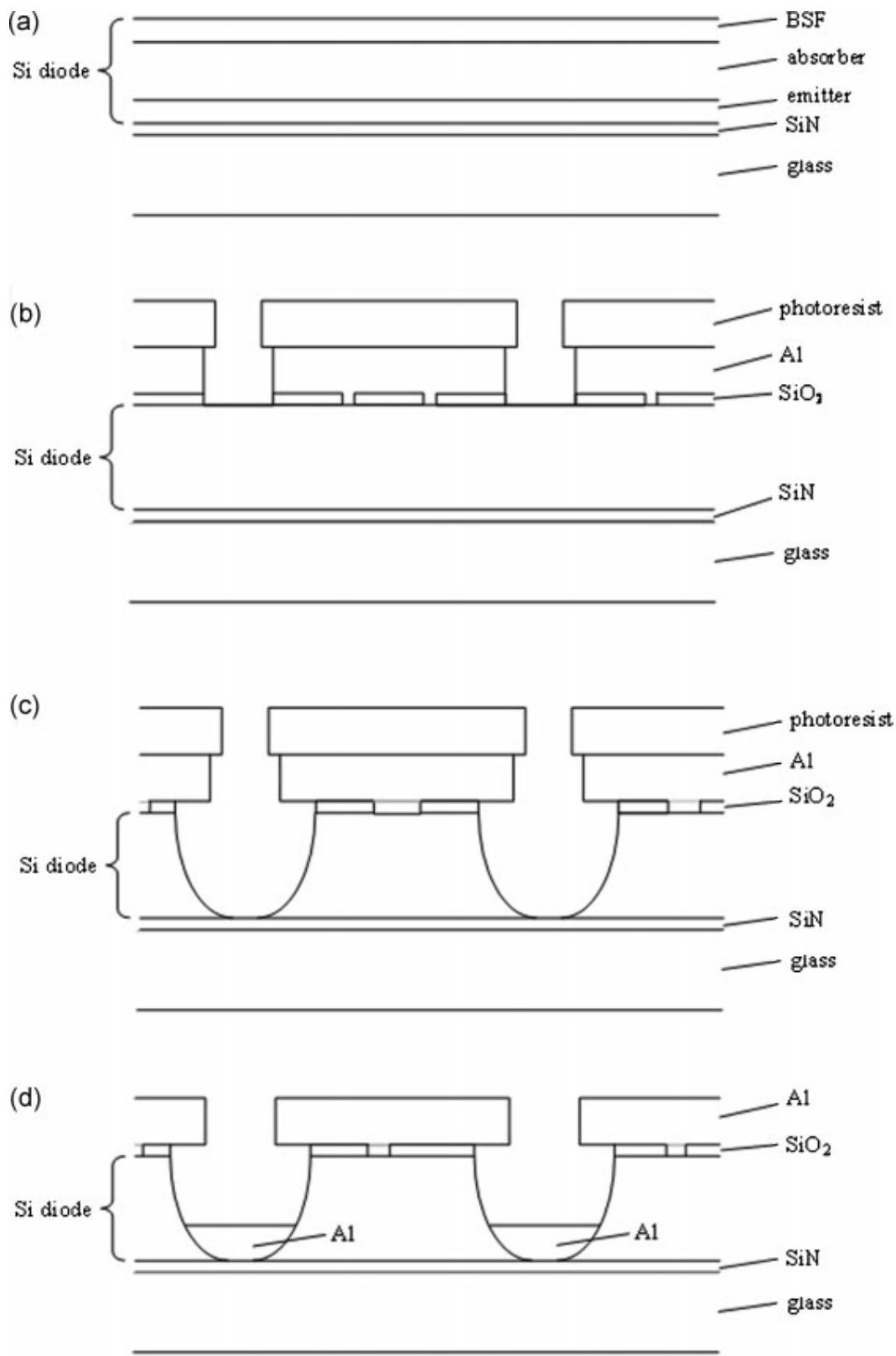
Figure 2-2: Schematic drawing of the interdigitated metallization scheme developed in UNSW for poly-Si thin-film solar cells on glass [11].

2.3 Glass and Si texturing techniques

2.3.1 Glass texturing techniques

For amorphous silicon thin-film solar cells [12] and the micromorph silicon thin-film solar cell [13], the silicon is deposited onto a transparent conductive oxide (TCO) which is suitably textured either by the TCO growth process itself or by a post-TCO deposition etching process. However, the high post-SPC thermal annealing temperature (above 900 °C) precludes poly-Si thin-film solar cell technologies from using TCO as a front electrode. Furthermore, a TCO layer adds significantly to the cost of the solar cell. Consequently, glass texturing is usually adopted for SPC poly-Si thin-film cells. Several glass texturing techniques developed in recent years for thin-film PV technologies are discussed below.

2.3.1.1 Abrasion-etch texture

The abrasion-etch texture method was developed by CSG Solar [3]. The glass surface undergoes sand blasting with SiC grit, followed by wet etching in HF acid. The HF etching is used to remove the most severe glass surface damage caused by the sand blasting process. Figure 2-3 is a scanning electron microscope (SEM) cross-sectional view of a poly-Si thin-film solar cell deposited on an abrasion-etch textured glass sheet. A 10 % efficient poly-Si thin-film minimodule on glass with the highest short-circuit current density (J_{SC}) of 29.5 mA/cm^2 reported so far was fabricated on a glass sheet prepared by the abrasion-etch method [3].
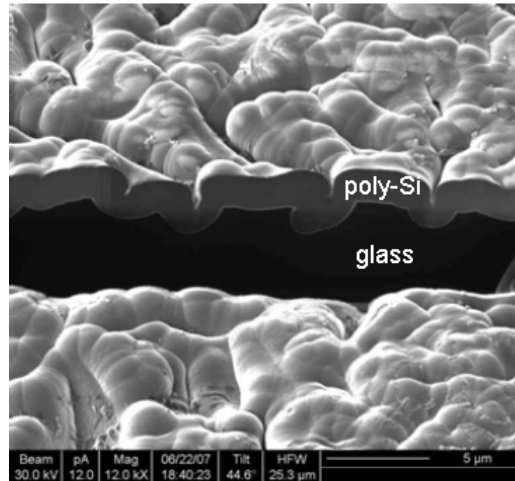
Figure 2-3: Scanning electron microscope (SEM) cross-sectional view of a poly-Si thin-film solar on a glass sheet prepared by the abrasion-etch method [3].

2.3.1.2 Glass beads

Bead-based texturing is another glass texturing technique developed by CSG Solar [14]. A glass sheet is coated with silica beads with size range of 0.3 to 2 µm, using a sol-gel process. However, low surface coverage of beads on glass (as shown in Figure 2-4) is one limiting issue of this texturing technique for light trapping applications.
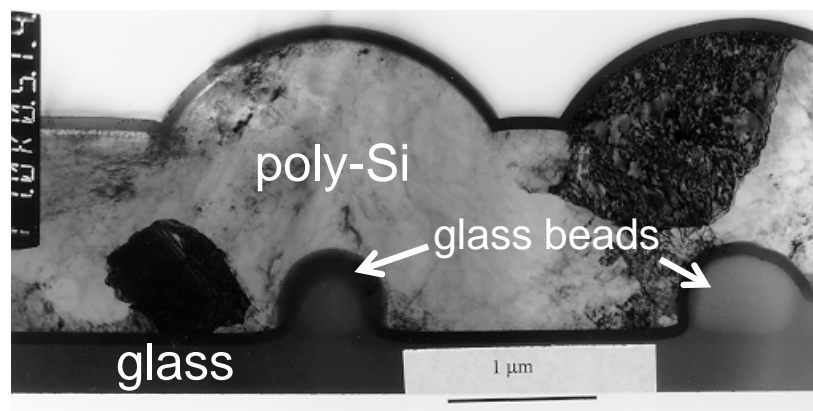
Figure 2-4: Cross-sectional transmission electron microscope (TEM) image of a poly-Si thin-film solar cell on a glass bead textured glass sheet [3].

19

2.3.1.3   Textured zinc oxide (ZnO) pattern transfer by ion beam etching

Figure 2-5 shows the process flow to prepare textured glass by the ZnO pattern transfer method [15]. A ZnO film is deposited by sputtering and then wet-chemically textured (Figure 2-5a). The textured ZnO layer is used as a three-dimensional etching mask for a following ion beam etching process. The glass surface areas where the overlying ZnO was fully etched will be etched first by the ion beam etching process (Figure 2-5(b) & (c)). With increasing ion beam etching time, the texture pattern of the ZnO layer is transferred to the glass surface (Figure 2-5d). One disadvantage of this method is the extra cost associated with the sacrificial ZnO layer.
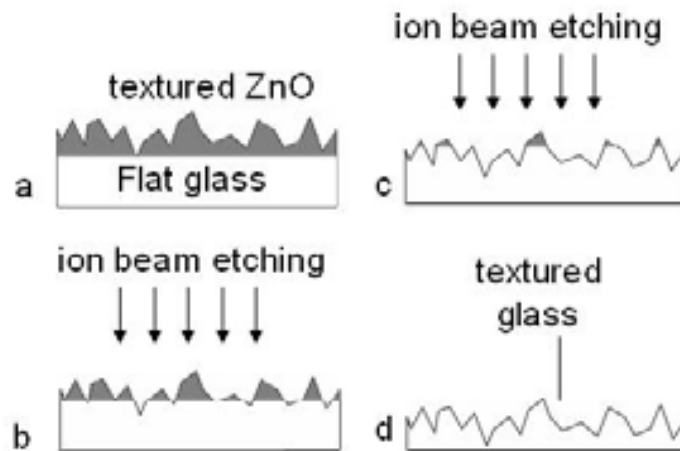
Figure 2-5: Schematic drawing to illustrate the procedures of ZnO texture pattern transformation by ion beam etching [15].

2.3.1.4   Aluminium induced texturing (AIT)

The aluminium induced texturing (AIT) method is an innovative glass texturing method developed and patented by Per Widenborg and Armin Aberle when they

did research on the poly-Si thin-film PV technology in The University of New South Wales (UNSW) during the last decade. A schematic process flow of the AIT method is shown in Figure 2-6. It consists of four process steps:

- Chemical cleaning and drying of planar glass

- Aluminium (Al) deposition on planar glass

- Thermal annealing at > 500 °C to stimulate a solid state reaction of the Al with the silicon dioxide (SiO_2) in the glass, presumably following the reaction $4Al + 3SiO_2 \rightarrow 2Al_2O_3 + 3Si$

- A textured glass surface is created by chemically removing the reactants in a $HF:HNO_3$ etch solution

Absorption close to the Lambertian limit has been demonstrated for poly-Si thin-film solar cells on AIT glass [16]. The impact of feature sizes and roughness of AIT glass sheets on light trapping performance has been studied in Ref. [16] and [47]. The highest reported J_{SC} so far for a poly-Si thin-film solar cell on AIT glass is 29 mA/cm^2, using a Si thickness of about 3 μm [11].

Step 1	Step 2
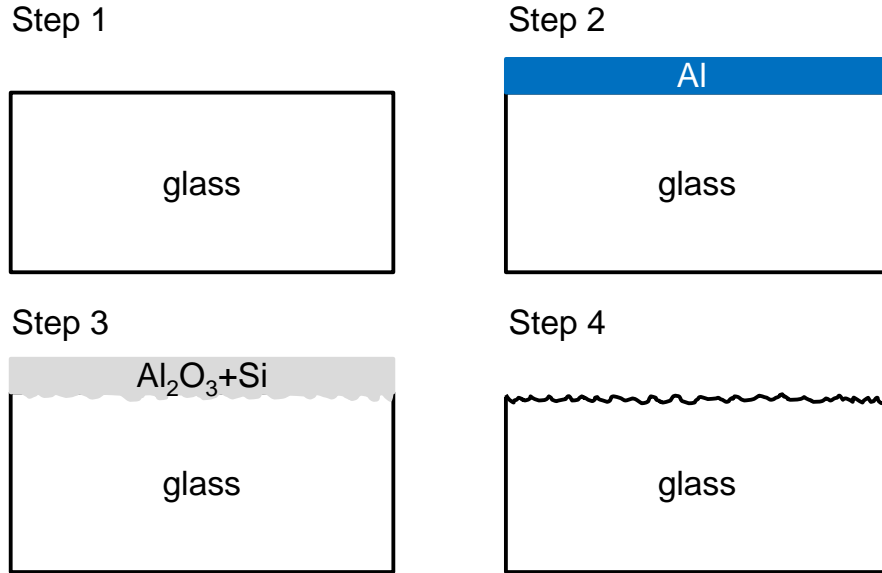
Figure 2-6: Schematic process flow of the AIT method. Step 1: Chemical cleaning and drying of a planar glass sheet. Step 2: Al deposition on one surface of the glass sheet. Step 3: Al reacts with glass at high temperature and thereby roughens the glass surface, with the reactants Al_2O_3 and Si non-uniformly distributed. Step 4: Removal of reactants and further texturing of the glass surface by $HF:HNO_3$ wet etching.

2.3.1.5   Nano-imprinting

Cui *et al.* developed a nano-imprinting process to reproduce AIT glass texture patterns [17]. Figure 2-7 is the flow chart of the nano-imprinting process. The authors of Ref. [17] successfully completed the pattern transfer from an AIT glass to a sol-gel. However, drastic quantum efficiency (QE) degradation was observed for poly-Si thin-film solar cells on sol-gel coated glass, because sol-gel is not compatible with the high-temperature rapid thermal annealing process [17].
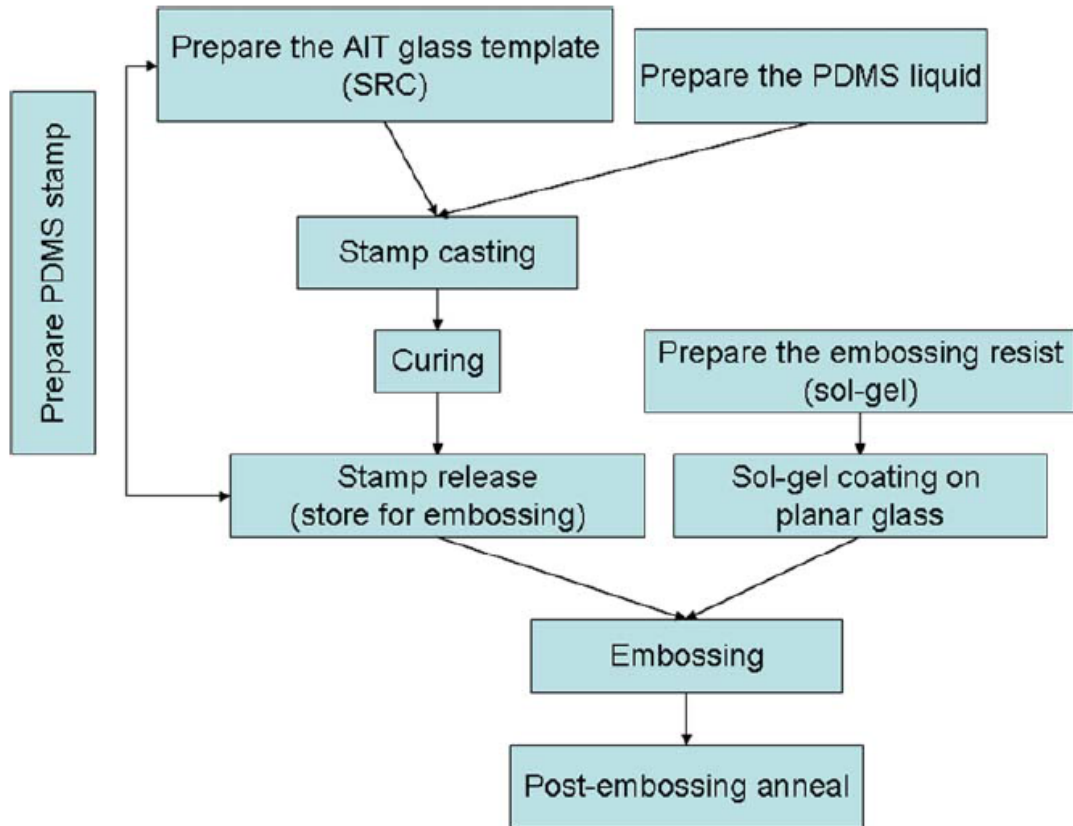
Figure 2-7: The flow chart of the nano-imprinting process to reproduce AIT patterns [17].

2.3.2 Si texturing techniques

2.3.2.1 Rear poly-Si thin-film surface texturing by wet etching

Besides glass texturing methods to enhance light trapping, texturing the rear Si surface by KOH wet etching is another effective light trapping method for poly-Si solar cells on planar glass sheets [18]. The wet etching method produces micron-size features. Using e-beam deposited a-Si, a SPC poly-Si thin-film solar cell with a short-circuit current density of 26.6 mA/cm^2 has been reported for an absorber layer thickness of 3.6 μm [18]. However, for this device, 2 μm of poly-Si material had to be removed by wet etching, which significantly increased the material consumption.

2.3.2.2 Front multicrystalline Si wafer surface texturing by plasma etching

'Black silicon' is a Si surface structure that has very low reflection. It can be produced by SF_6/O_2 reactive ion etching (RIE) [19]. A schematic to illustrate the reaction forming black silicon is shown in Figure 2-8. SF_6/O_2 is fed into the chamber and then partially ionized by the plasma. The F and O ions are then accelerated to the Si surface. F radicals chemically etch away Si. O radicals together with Si and F form the volatile polymer product $Si_xO_yF_z$, which masks the Si from etching by the F radicals. This competition between F chemical etching and $Si_xO_yF_z$ by-product formation results in an uneven etch rate across the whole Si surface, producing a surface texture. Si surface texturing of multicrystalline Si wafer solar cells by dry plasma etching was studied by several research groups [20-24]. The authors of Refs. 20-24 demonstrated that dry plasma etching is a feasible method to achieve higher PV efficiency for multicrystalline Si wafer solar cells, by improving J_{SC} and without deteriorating V_{OC} and *FF*.
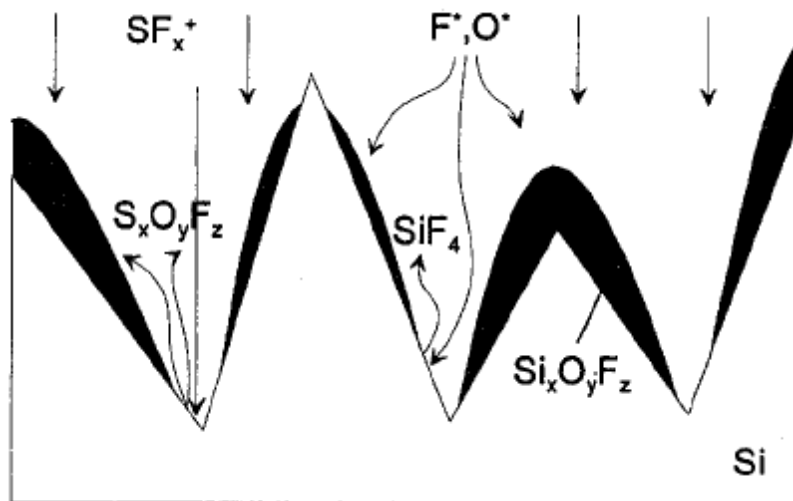
Figure 2-8: Schematic of the reaction forming black silicon by regenerated and self-induced masking [21]

2.4 Scattering parameters, scattering simulation models, and commercial thin-film solar cell simulator ASA

2.4.1 Scattering parameters of rough surfaces

In this thesis, we use two types of scattering parameters to characterize the optical scattering process at a rough interface: (i) haze, and (ii) angular intensity distribution (AID) [25]. When incident light arrives at the interface of two materials, total transmission T_{tot} (and total reflection R_{tot}) consists of two components: specular transmission T_{spe} (specular reflection R_{spe}), and diffuse transmission T_{dif} (diffuse reflection R_{dif}), as shown in Figure 2-9. The haze parameters, in transmission H_T and in reflection H_R, are defined by $H_T = T_{dif} / T_{tot}$ and $H_R = R_{dif} / R_{tot}$, respectively. The haze can be measured with a spectrophotometer with an integrating sphere (further details are given in Section 2.5.2.3). The AID parameter describes the distribution of the scattered light intensity in every scattering angle. It can be measured with a goniometer (further details are given in Section 2.5.3).
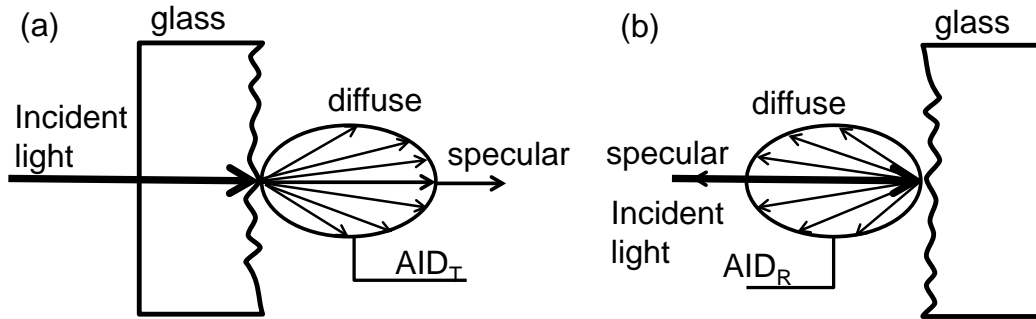
Figure 2-9: Illustration of haze and AID of textured glass/air interface in transmission (a) and in reflection (b).

2.4.2 Optical models to simulate scattering at rough surfaces

The scattering modelling methods of textured surfaces mainly consist of three categories: i) rigorous solvers of the Maxwell equations, such as the finite difference time domain (FDTD) method [26, 27] and finite element method [28]; ii) scalar scattering theory utilizing diffraction integrals, such as the model based on the first-order Born approximation developed by Jäger and Zeman [29], the grating model formulated by Bittkau *et al.* [30], and the phase model developed by Dominé *et al.* based on the Rayleigh-Sommerfeld diffraction integral [31, 32]; and iii) ray-tracing method based on geometric optics [16, 33].

2.4.3 Commercial thin-film solar cell simulator ASA

ASA (Advanced Semiconductor Analysis) is an one-dimensional (1D) opto-electronic solar cell simulator [34, 35] developed by Delft University of Technology, Netherlands. In this thesis, haze and AID of textured surfaces are entered into ASA to perform optical simulations of poly-Si thin-film solar cells on

glass. All ASA input files (ASCII files with file extension "cas") used in this thesis are in the CD submitted together with the hard copy of this thesis. Details of the software can be found on its official website at Delft University of Technology [36].

2.5 Characterization methods

2.5.1 Microscopy

2.5.1.1 Optical microscope (OM)

Dark field optical microscopy on uncoated textured glass was found to be a simple and effective method to predict the absorption-enhancing potential of a glass texture [16]. In dark field optical microscope images, features with higher scattering efficiency appear brighter than features with lower scattering efficiency. In this thesis, an Olympus STM6 measuring microscope was used to do optical microscopy on AIT glass samples fabricated in SERIS.

2.5.1.2 Atomic force microscope (AFM)

The AFM is a scanning microscopy method originally developed to study single atoms and molecules. Van der Waals interaction between atoms and molecules is the main principle used in AFM techniques. The AFM has been adopted by the optics community to study fine details on small surface areas (usually < 100 μm × 100 μm). Figure 2-10 illustrates the setup of a typical AFM measurement. The AFM consists of a micro-scale cantilever with a sharp tip (probe) at its end that is used to scan the specimen's surface. The tip is brought into proximity of the sample surface, where forces between the tip and the sample lead to a deflection

of the cantilever according to Hooke's law. The deflection is measured using a laser spot reflected from the top of the cantilever into an array of photodiodes. The tip is driven by a feedback mechanism to adjust the tip-to-sample distance to maintain a constant force or a constant distance between the tip and the sample. The cantilever is mounted on a piezoelectric tube, which can move in the z direction for maintaining a constant force or distance, and the x and y directions for scanning the sample. The AFM can be operated in three different modes: i) contact mode: the tip is dragged along a sample's surface; ii) non-contact or intermittent mode: the cantilever oscillates above the sample's surface and is affected by surface/tip forces (Van der Waals) that change the resonant frequency of the cantilever; and iii) tapping mode: the AFM tip taps the sample surface during the closest point of approach of an oscillation cycle and detects variations in topography by changes in the cantilever oscillation frequency or amplitude. More details of the AFM technique can be found in Ref. [37]. A Veeco Dimension 3100 AFM was used in this thesis to characterize surface profiles of various textured surfaces.
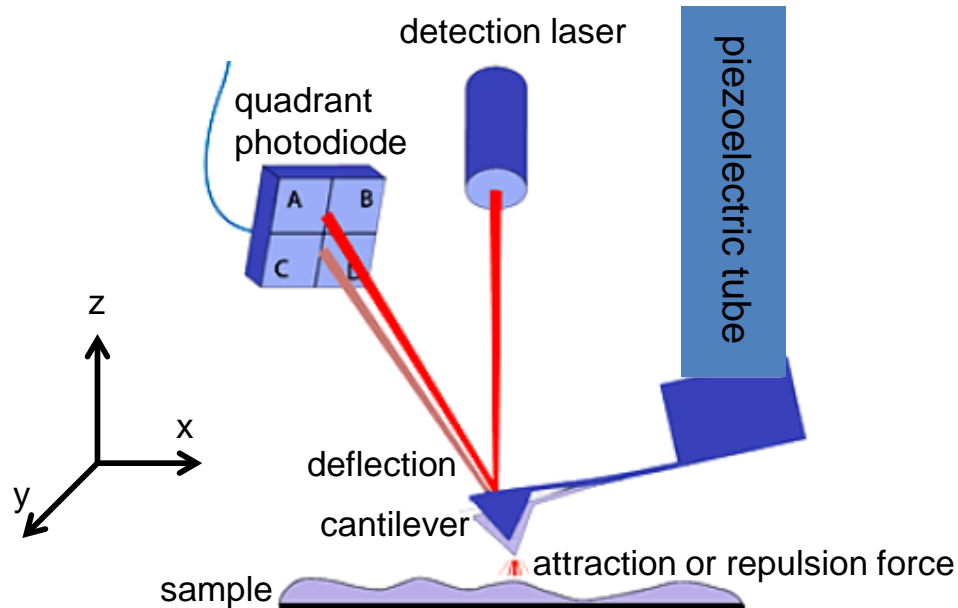
Figure 2-10: Setup of a typical AFM measurement.

2.5.1.3 Scanning electron microscope (SEM)

The SEM technique produces images of a sample by scanning it with a focused beam of electrons. One of the most striking features of the SEM is that it enables studying topography of a sample with nanometre scale resolution, which cannot be achieved by optical microscopy techniques. A Zeiss AURIGA crossbeam workstation was used in this thesis to characterize topographies. The magnification of the AURIGA SEM tool is in the range of 12 times to one million times.

2.5.2 Spectroscopy

2.5.2.1　　　Raman spectroscopy

Raman scattering was discovered by C.V. Raman in 1928. It is a spectroscopic technique used to observe vibrational, rotational, and other low-frequency modes in a system. It relies on inelastic scattering, or Raman scattering, of mono-chromatic light, usually from a laser in the visible, near infrared, or near ultraviolet range, whereby the energy of the scattered photons is lower or higher than the energy of the incident photons. A comprehensive introduction to the Raman spectroscopy method is given in Ref. [38]. A Renishaw inVia Raman spectro-meter with a laser wavelength of 514 nm and a laser spot size of 1 μm is used in Chapter 4 of this thesis to study the AIT glass texture process.

2.5.2.2　　　Energy-dispersive X-ray spectroscopy (EDX or EDS)

An energy-dispersive X-ray (EDX) spectrometer is attached to a SEM instrument to perform elemental composition analysis of all elements down to atomic number 5 (boron). The operating principle of the EDX method can be found in Ref. [39]. An AMETEK EDAX system attached to a NOVA NanoSEM 230 SEM station is used in Chapter 4 of this thesis to study the AIT glass texturing process.

2.5.2.3　　　Ultra-violet (UV), visible (Vis), near infrared (NIR) spectroscopy

The total and diffuse transmittances (T_{tot} & T_{dif}), as well as the total and diffuse reflectances (R_{tot} & R_{dif}) of glass and poly-Si thin-films on glass are measured in this work with a PerkinElmer UV/Vis/NIR Lambda 950 dual beam spectrometer having a 150 mm integrating sphere. Light sources used in the Lambda 950 are

a halogen lamp for operation in the Vis and NIR ranges, and a deuterium lamp for operation in the UV range. A monochromatic beam (the sample beam in Figure 2-11) produced by a grating monochromator over the wavelength range from 200 nm to 2500 nm is directed on the sample through the entrance port of the integrating sphere. Another monochromatic beam (the reference beam in Figure 2-11) enters the sphere through another entrance port. Two detectors (a Peltier cooled PbS detector and a Hamamatsu R-955 photomultiplier tube) are placed inside the integrating sphere to measure the intensities of the sample beam and the reference beam.

Before a measurement is taken on a sample, a calibration of the system is performed by measuring a 100% background, whereby a 100% reflecting white standard (Spectralon^{TM}) is placed in the "sample" position in Figure 2-11(b). Then, for the transmittance measurement, the sample is mounted at the entrance port of the sphere (Figure 2-11(a)). Correspondingly, for the reflectance measurement, it is mounted at the rear of the integrating sphere (Figure 2-11(b)). Absorptance (A) is calculated via $A = 1 - T_{tot} - R_{tot}$ [40]. To measure the diffuse transmittance and reflectance, the port opposite the sample must be opened (see Figure 2-11(a) and (b)). In this thesis, both transmittance and reflectance measurements are done in the superstrate configuration, i.e., the incident beam enters the sample from the glass side.

(a) Transmittance measurements   (b) Reflectance measurements
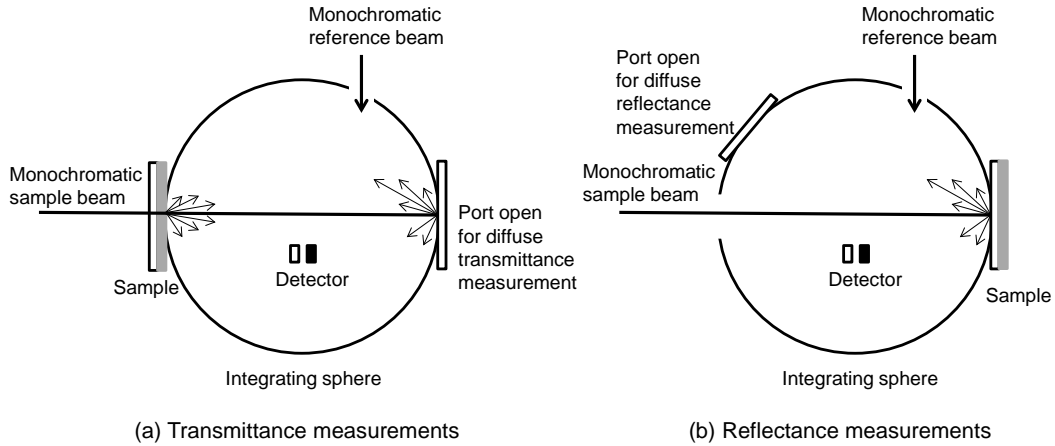
Figure 2-11: Schematic drawing to show transmittance (a) and reflectance (b) measurements using an integrating sphere.

It is important to note that, for PECVD SPC poly-Si thin-film solar cells on glass, the absorption calculated via $A = 1 - R - T$ is overestimated in the NIR wavelength region if the sample features any type of light trapping mechanism (like a textured glass surface or a textured rear Si surface). This is because R and T are both underestimated due to measurement errors [41]. In the R and T measurements, a fraction of the incident light travels laterally inside the thick (3.3 mm) glass sheet and thus these photons never enter the integrating sphere, see for example ray 1 in Figure 2-12 (a) and rays 2 and 3 in Figure 2-12 (b).
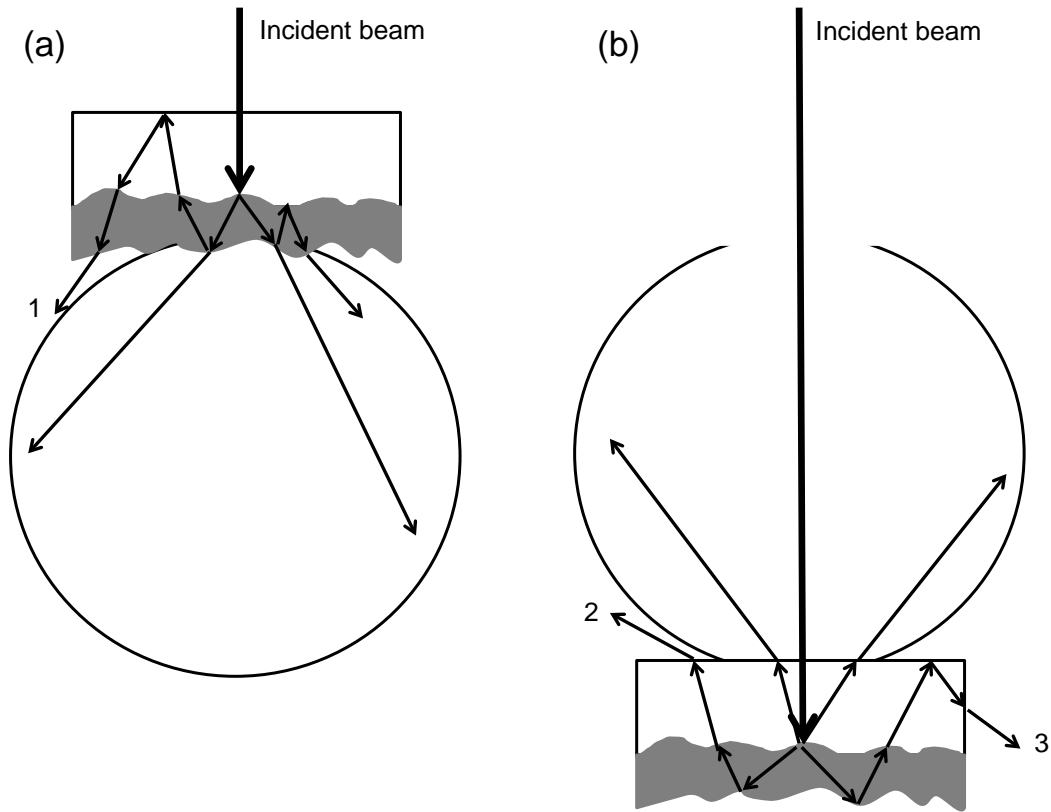
Figure 2-12: A schematic to demonstrate rays not entering the integrating sphere in (a) transmittance measurements, and (b) reflectance measurements.

The measurement errors for *R* and *T* can be avoided if absorptance is directly measured by placing the measured sample in the centre of the integrating sphere ('centre mount measurement'). In Ref. [41], Campbell *et al.* measured the absorptance of poly-Si thin-film solar cells on AIT glass using both methods (i.e., the *A = 1 - R -T* method and the centre mount method). The measured absorptance results of Ref. [41] are shown in Figure 2-13. The difference in Ref. [41] between the measured absorptance using both methods is insignificant at wavelengths below 1000 nm. In the wavelength range from 1000 nm to 1100 nm, the difference in absorptance increases gradually to about 10%. In the wavelength range from 1100 nm to 1500 nm, the measured absorptance by using the

centre mount method was about 20%, which is consistently ~ 10% lower than the measured absorptance via the *A = 1 - R - T* method. The difference of about 10% (absolute) in the 1100 - 1500 nm range represents the measurement error resulting from the *A = 1 - R - T* method. The measured absorptance of ~ 20% in the centre mount method in the 1100 - 1500 nm range indicates that there is ~20% absorption due to materials other than silicon (glass in this case). Parasitic glass absorption will be discussed in detail in Chapter 5.
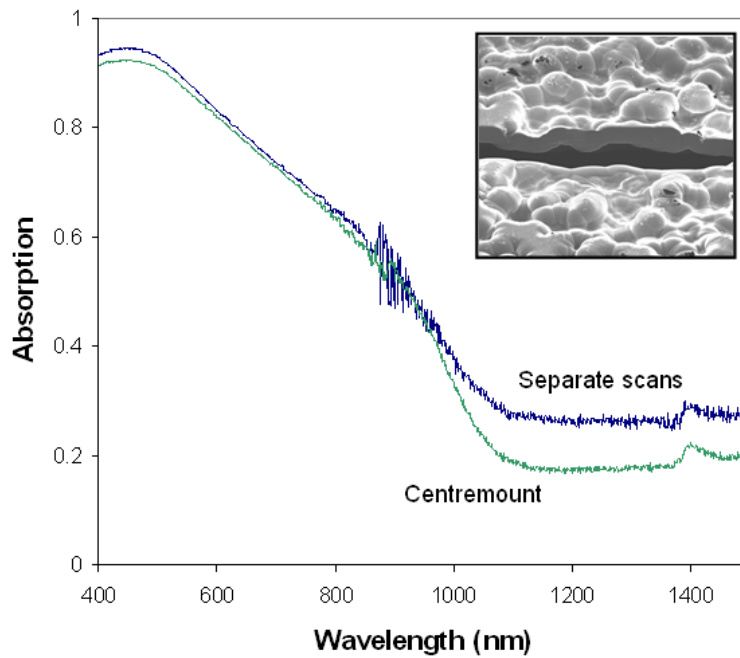
Figure 2-13: The absorptance measured using separate R and T scans and the centre mount method. Inset is a cross section image of a poly-Si thin-film on textured glass [41].

Generally, the absorptance results obtained via *A = 1 - R -T* are treated with care in this thesis. The principles are:

i) Absorptance data below a wavelength of 1000 nm are more trust-worthy;

ii) A relative light trapping performance comparison based on absorptance data of devices with similar light trapping structures are trusted.

2.5.3 Goniophotometre

A commercial goniophotometre (pgII) from pab advanced technologies GmbH, Germany [42, 43] is used in this thesis to measure the angular intensity distribution (AID) in transmission for AIT glass sheets. Figure 2-14 is an isometric view of the goniophotometre. It consists of three main components: i) a light source; ii) a sample holder; and iii) a detector. The light source used in this thesis is a halogen lamp. A quasi-monochromic light beam is generated by inserting an optical filter into the beam of the halogen lamp. The AIDs in transmission at three wavelengths (520, 620 and 780 nm) are measured for AIT glass in this thesis. The detector arm of the goniophotometre scans both the transmission hemi-sphere and the reflection hemisphere, to capture the scattered light intensity distribution in both hemispheres.
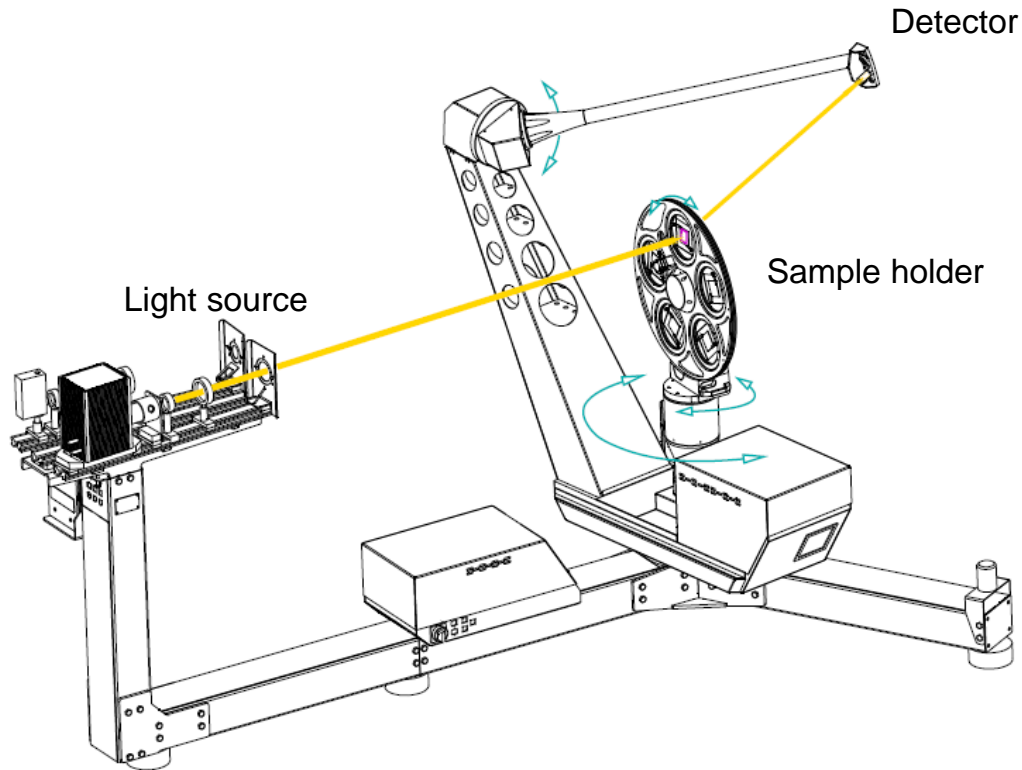
Figure 2-14: An isometric view of the pgII goniophotometre [42].

2.5.4 X-ray diffraction (XRD)

XRD is a crystallographic technique based on Bragg's law to determine the atomic and molecular structure of a crystal. The operating principles of a XRD are illustrated in Ref. [44]. In Chapter 4 of this thesis, a Panalytical X'pert Pro XRD equipped with a high-temperature chamber (Anton Paar, HTK1200N) is used to identify silicon peaks and to obtain the activation energy of the redox reaction between Al and glass.

2.5.5 Suns-V_{OC}

The Suns-V_{OC}, or quasi-steady-state V_{OC} (QSS V_{OC}) measurement technique was introduced by Sinton and Cuevas in 2000 [45]. One big advantage of this

technique is that it can characterize solar cells without metallization, which provides early feedback on device performance and hence is well suited for process optimization purposes. A home-built Suns-V_{OC} system at SERIS [46] is used in this thesis to evaluate the electrical poly-Si diode quality in Chapter 3.

References (Chapter 2)

[1] P.A. Basore, CSG-1: Manufacturing a New Polycrystalline Silicon PV Technology, in: Conference Record of the 2006 IEEE 4th World Conference on Photovoltaic Energy Conversion, 2006, pp. 2089-2093.

[2] T. Matsuyama, K. Wakisaka, M. Kameda, M. Tanaka, T. Matsuoka, S. Tsuda, S. Nakano, Y. Kishi, Y. Kuwano, Preparation of High-Quality n-Type Poly-Si Films by the Solid Phase Crystallization (SPC) Method, Japanese Journal of Applied Physics, 29 (1990), pp. 2327 - 2331.

[3] M. Keevers, T.L. Young, U. Schubert, R. Evans, R.J. Egan, M.A. Green, 10% Efficient CSG minimodules, in: 22nd European Photovoltaic Solar Energy Conference, Milan, 2007, pp. 1783.

[4] H. Hidayat, A. Kumar, F. Law, C. Ke, P.I. Widenborg, A.G. Aberle, Impact of rapid thermal annealing temperature on non-metallised polycrystalline silicon thin-film diodes on glass, Thin Solid Films, 534 (2013) 629-635.

[5] F. Law, B. Hoex, J. Wang, J. Luther, K. Sharma, M. Creatore, M.C.M. Van De Sanden, Kinetic study of solid phase crystallisation of expanding thermal plasma deposited a-Si:H, Thin Solid Films, 520 (2012) 5820-5825.

[6] F. Law, H. Hidayat, A. Kumar, P. Widenborg, J. Luther, B. Hoex, On the transient amorphous silicon structures during solid phase crystallization, Journal of Non-Crystalline Solids, 363 (2013) 172-177.

[7] F. Law, P.I. Widenborg, J. Luther, B. Hoex, Medium range order engineering in amorphous silicon thin films for solid phase crystallization, Journal of Applied Physics, 113 (2013), 193511 - 193511-6.

[8] H. Hidayat, P.I. Widenborg, A. Kumar, F. Law, A.G. Aberle, Static large-area hydrogenation of polycrystalline silicon thin-film solar cells on glass using a linear microwave plasma source, IEEE Journal of Photovoltaics, 2 (2012) 580-585.

[9] P.I. Widenborg, A.G. Aberle, Polycrystalline silicon thin-film solar cells on AIT-textured glass superstrates, Advances in OptoElectronics, 2007 24584.

[10] P.I. Widenborg, S.V. Chan, T. Walsh, A.G. Aberle, Thin-film poly-SI solar cells on AIT-textured glass - Importance of the rear reflector, in, 33rd IEEE Photovoltaic Specialists Conference, 2008, p. 1-3.

[11] P.J. Gress, P.I. Widenborg, S. Varlamov, A.G. Aberle, Wire bonding as a cell interconnection technique for polycrystalline silicon thin-film solar cells on glass, Progress in Photovoltaics: Research and Applications, 18 (2010) 221-228.

[12] D.E. Carlson, Amorphous-silicon solar cells, IEEE Transactions on Electron Devices, 36 (1989) 2775-2780.

[13] J. Meier, S. Dubail, R. Fluckiger, D. Fischer, H. Keppner, A. Shah, Intrinsic microcrystalline silicon (μc-Si:H) - A promising new thin film solar cell material, Proc. 1st World Conference on Photovoltaic Energy Conversion, (1994) 409-412.

[14] J.J. Ji, Z.R. Shi, Texturing of glass by SiO$_2$ film, US patent 6420647B1, 2002.

[15] W. Zhang, E. Bunte, J. Worbs, H. Siekmann, J. Kirchhoff, A. Gordijn, J. Hüpkes, Rough glass by 3d texture transfer for silicon thin film solar cells, physica status solidi (c), 7 (2010) 1120-1123.

[16] G. Jin, P.I. Widenborg, P. Campbell, S. Varlamov, Lambertian matched absorption enhancement in PECVD poly-Si thin film on aluminum induced textured glass superstrates for solar cell applications, Progress in Photovoltaics: Research and Applications, 18 (2010) 582-589.

[17] H. Cui, P. Campbell, M.A. Green, Nano-imprinting for polycrystalline silicon thin-film solar cells on glass superstrate application, in: 27th European PV Solar Energy Conference and Exhibition (EUPVSEC), Frankfurt, 2012, pp. 2408 - 2412.

[18] T. Soderstrom, Q. Wang, K. Omaki, O. Kunz, D. Ong, S. Varlamov, Light confinement in e-beam evaporated thin film polycrystalline silicon solar cells, Physica Status Solidi - Rapid Research Letters, 5 (2011) 181-183.

[19] H. Jansen, M. d. Boer, R. Legtenberg, M. Elwenspoek, The black silicon method: a universal method for determining the parameter setting of a fluorine-based reactive ion etcher in deep silicon trench etching with profile control, Journal of Micromechanics and Microengineering, 5 (1995) 115.

[20] D.S. Ruby, W.L. Wilbanks, C.B. Fleddermann, M.D. Rosenblum, S. Roncin, S. Narayanan, Optimization of plasma deposition and etching processes for commercial multicrystalline silicon solar cells, in: Conference Record of the Twenty Fifth IEEE Photovoltaic Specialists Conference, 1996, pp. 637-640.

[21] M. Schnell, R. Ludemann, S. Schaefer, Plasma surface texturization for multicrystalline silicon solar cells, in: Conference Record of the Twenty-Eighth IEEE Photovoltaic Specialists Conference, 2000, pp. 367-370.

[22] O. Schultz, G. Emanuel, W. Glunz, G.P. Willeke, Texturing of multicrystalline silicon with acidic wet chemical etching and plasma etching, in: Proceedings of 3rd World Conference on Photovoltaic Energy Conversion, 2003, pp. 1360-1363 Vol.1362.

[23] D.H. Macdonald, A. Cuevas, M.J. Kerr, C. Samundsett, D. Ruby, S. Winderbaum, A. Leo, Texturing industrial multicrystalline silicon solar cells, Solar Energy, 76 (2004) 277-283.

[24] K.-S. Lee, M.-H. Ha, J.H. Kim, J.-W. Jeong, Damage-free reactive ion etch for high-efficiency large-area multi-crystalline silicon solar cells, Solar Energy Materials and Solar Cells, 95 (2011) 66-68.

[25] J. Krč, M. Zeman, O. Kluth, F. Smole, M. Topič, Effect of surface roughness of ZnO:Al films on light scattering in hydrogenated amorphous silicon solar cells, Thin Solid Films, 426 (2003) 296-304.

[26] K.S. Yee, Numerical solution of initial boundary value problems involving Maxwell's equations in isotropic media, IEEE Transactions on Antennas and Propagation, 14 (1966) 302-307.

[27] A. Taflove, S.C. Hagness, Computational Electrodynamics: The Finite-Difference Time-Domain Method, 3rd ed., Artech House, 2005.

[28] J. Jin, The finite element method in electromagnetics, Wiley, 1993.

[29] K. Jäger, M. Zeman, A scattering model for surface-textured thin films, Applied Physics Letters, 95 (2009), 171108.

[30] K. Bittkau, M. Schulte, T. Beckers, R. Carius, Fourier analysis for the study of light scattering properties of randomly textured ZnO films, Proceedings of SPIE - The International Society for Optical Engineering, 7725 (2010).

[31] D. Domine, F.-J. Haug, C. Battaglia, C. Ballif, Modeling of light scattering from micro- and nanotextured surfaces, Journal of Applied Physics, 107 (2010) 044504.

[32] K. Jäger, M. Fischer, R.A.C.M.M. Van Swaaij, M. Zeman, A scattering model for nano-textured interfaces and its application in opto-electrical simulations of thin-film silicon solar cells, Journal of Applied Physics, 111 (2012) 083108.

[33] M. Schulte, K. Bittkau, B.E. Pieters, S. Jorke, H. Stiebig, J. Hüpkes, U. Rau, Ray tracing for the optics at nano-textured ZnO-Air and ZnO-Silicon interfaces, Progress in Photovoltaics: Research and Applications, 19 (2011) 724-732.

[34] M. Burgelman, J. Verschraegen, S. Degrave, P. Nollet, Modeling thin-film PV devices, Progress in Photovoltaics: Research and Applications, 12 (2004) 143-153.

[35] M. Zeman, J. Krc, Optical and electrical modeling of thin-film silicon solar cells, Journal of Materials Research, 23 (2008) 889-898.

[36] "ASA software official website", Available: http://www.ewi.tudelft.nl/en/the-faculty/departments/ electrical-sustainable-energy/photovoltaic-materials-and-devices/asa-software (accessed on 17 Dec 2013)

[37] L. Mattsson, Scanning probe microscopy, in: D. Brune, R. Hellborg, H.J. Whitlow, O. Hunderi (Eds.) Surface Characterization: A User's Sourcebook, Wiley VCH, Weinheim, Germany, 1997, pp. 77-81.

[38] E.J. Samuelsen, Raman spectroscopy, in: D. Brune, R. Hellborg, H.J. Whitlow, O. Hunderi (Eds.) Surface Characterization: A User's Sourcebook, Wiley VCH, Weinheim, Germany, 1997, pp. 390-392.

[39] K. Kristiansen, Scanning electron microscope with energy-and wavelength-dispersive spectrometry, in: D. Brune, R. Hellborg, H.J. Whitlow, O. Hunderi (Eds.) Surface Characterization: A User's Sourcebook, Wiley VCH, Weinheim, Germany, 1997, pp. 111-128.

[40] ASTM, E903-12: Standard Test Method for Solar Absorptance, Reflectance, and Transmittance of Materials Using Integrating Spheres, in, 2012.

[41] P. Campbell, P.I. Widenborg, A.B. Sproul, A.G. Aberle, surface textures for large-grained poly-silicon thin-film solar cells on glass using the AIT method, Tech. Digest 15th International Photovoltaic Science and Engineering Conference (PVSEC), Shanghai, China, 2005, pp. 859-860.

[42] P. Apian-Bennewitz, New scanning gonio-photometer for extended BRTF measurements, in SPIE proceedings on Instruments and Applications II, vol. 7792, 2010, 77920O.

[43] L.O. Grobe, S. Wittkopf, P. Apian-Bennewitz, J.C. Jonsson, M. Rubin, Experimental validation of bidirectional reflection and transmission distribution measurements of specular and scattering materials, in Proc. SPIE 7725, Photonics for Solar Energy Systems III, 2010, 772510.

[44] B.D. Cullity, S.R. Stock, Elements of X-ray Diffraction, 3rd ed., Prentice-Hall, 2001.

[45] R.A. Sinton, A. Cuevas, A Quasi-Steady-State Open-Circuit Method for Solar Cell Characterization, Proc. 16th EU PVSEC, Glasgow, Scotland, 2000, pp. 1152-1155.

[46] H. Hidayat, P.I. Widenborg, A.G. Aberle, Large-area Suns-V_{oc} Tester for Thin-film Solar Cells on Glass Superstrates, Energy Procedia, 15 (2012) 258-264.

[47] H. Cui, M. Green, P. Campbell, O. Kunz, S. Varlamov, A photovoltaic light trapping estimation method for textured glass based on surface decoupling calculation, Solar Energy Materials and Solar Cells, 109 (2013) 82-90.

Chapter 3 Pilot line-scale fabrication of AIT glass and poly-Si thin-film solar cells on AIT glass

3.1 Introduction

Previous work done at the University of New South Wales (UNSW) [1, 2] showed that the AIT glass texturing method is a very effective light trapping technique for PECVD SPC poly-Si thin-film solar cells on glass. Therefore, in the present work, the AIT technique was used as the glass texturing method for SERIS' PECVD SPC poly-Si thin-film solar cells on glass. In this chapter, a stable pilot line-scale AIT glass texturing process with reproducible high scattering efficiency and optical uniformity has been set up (Section 3.2). The fabricated pilot line-scale AIT glass sheets have a high optical scattering efficiency and good optical uniformity. Furthermore, the process to fabricate poly-Si thin-film solar cells on AIT glass has been improved, as described in Section 3.3.

3.2 AIT glass fabrication

3.2.1 Qualification of commercial borosilicate glass from a Chinese supplier

Borosilicate float glass ('Borofloat33') from Schott AG, Germany [3] with a thickness of 3.3 mm was used in UNSW and CSG Solar as the substrate for SPC poly-Si thin-film growth. The cost of Borofloat33 glass sheets is high for PV applications and hence significantly increases the materials cost of PECVD SPC poly-Si thin-film solar cells. To reduce the fabrication cost, we tried an alternative glass supplier from China (Heping Glass Pte. Ltd [4]) who are selling borosilicate glass sheets with the same glass sheet thickness and size as Borofloat33 glass, but at a much lower cost. The significantly lower glass cost motivated us to qualify this alternative glass supplier.

Two 10 cm × 10 cm glass samples from Schott and the Chinese supplier were named Schott 1 and China 1, respectively. Their transmittances (T) and reflectances (R) were measured with an UV-Vis-NIR spectrophotometer (PerkinElmer, Lambda 950), which has a 150 mm diameter integrating sphere. These two samples then went through a rapid thermal process (RTP) at 1050 °C for 1 minute. A commercial infrared lamp based RTP system from CVD Equipment Corporation, USA, was used to do the RTP. The process was performed in a nitrogen-purged atmospheric pressure environment. Then, T and R of both glass samples were measured again with the spectrophotometer. The absorptances (A)

of the samples Schott 1 and China 1 before and after the RTP were calculated via $A = 1 - R - T$.

There was no visible glass sheet deformation due to the rapid thermal process, for both samples. This shows that the borosilicate glass from the Chinese supplier is able to withstand the high temperatures of our poly-Si solar cell process. Figure 3-1 shows the measured absorptances (A) of samples Schott 1 and China 1, before and after the rapid thermal process. It can be seen that the optical performance in the spectral range of interest (300 to 1500 nm) is almost identical for both samples.

Given that the borosilicate glass from the Chinese supplier has similar thermal and optical properties as Schott's Borofloat33 glass, we concluded that this glass is well suited for making PECVD SPC poly-Si thin-film solar cells on glass.
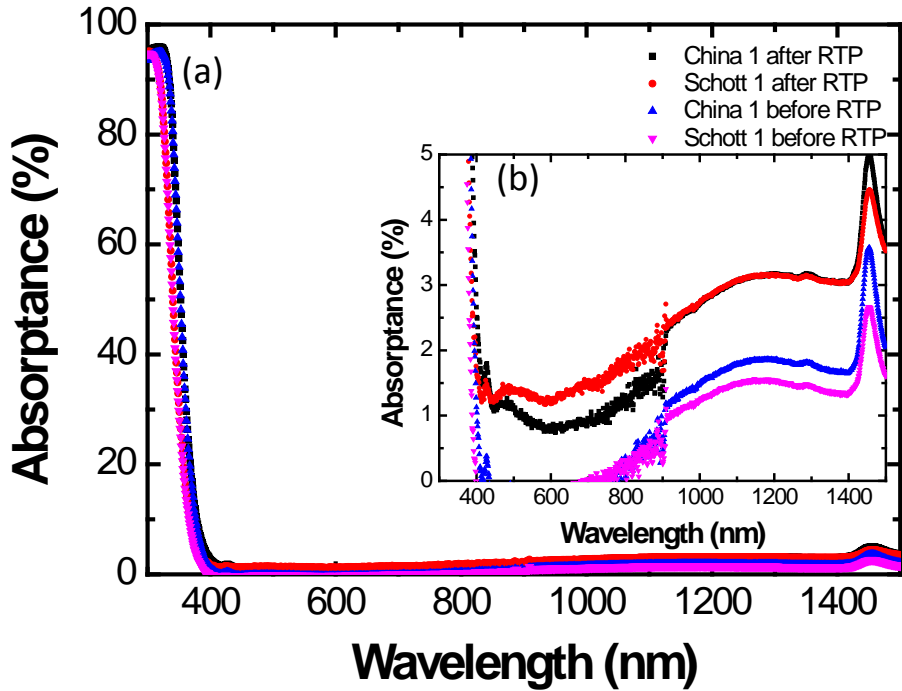
Figure 3-1: (a): Absorptance results of glass sheet samples Schott 1 and China 1 before & after RTP. (b) Glass absorptance data with smaller y axis scale in wavelength range 400-1500 nm.

3.2.2 AIT glass fabrication process in SERIS

Table 3-1 shows the detailed fabrication sequence of AIT glass in SERIS for borosilicate glass, from both Schott and the Chinese supplier. First, each glass sheet is cleaned in a dish washer (Miele, G7883CD) to remove both organic and inorganic contaminations at the glass surfaces. For the borosilicate glass from China, an additional manual isopropyl alcohol (IPA) clean was applied before putting it into the Miele glass washer. Then, the glass sheet is baked at 150 °C for 30 minutes in a baking chamber of a cluster tool from MVSystems (USA), to evaporate water residues. Next follows a cool-down step to room temperature (during ~30 minutes) inside a sputtering chamber of the cluster tool. One surface of the glass sheet is then coated with Al by DC sputtering, using an argon (Ar) atmosphere. The deposition parameters are as follows: RF power 215 W, pressure 0.003 mTorr, Ar gas flow 25 sccm, and deposition time 40 minutes. The estimated Al thickness is 120 nm. The Al-coated glass sheet is then annealed in a nitrogen-purged atmospheric-pressure box furnace at about 570 °C for 4 hours, to ensure that the Al has fully reacted with the glass (mainly SiO_2). The temperature ramp-up rate is 10 °C/minute. After the annealing, the glass sheet is cooled down naturally inside the box furnace to about 100 °C and is then taken out of the furnace to further cool down to room temperature. A photo of a glass sheet after the annealing step is shown in Figure 3-2(a). The annealed glass sheet is then wet-chemically etched using a $HF:HNO_3$ solution to remove the reaction products, followed by a 10-minute rinse in DI water. A photo of a glass sheet after the wet etching and DI water rinse is shown in Figure 3-2(b).

Table 3-1: Fabrication sequence of AIT glass for both Borofloat33 glass and borosilicate glass from China.

Process	Borofloat33 glass	Borosilicate glass from China
Isopropyl alcohol (IPA) clean	Not applicable	Manually clean glass surfaces
Glass wash	Program E (universal) of Miele G7883CD glass washer	
Baking	150 ºC for 20 minutes	
Cool down	30 minutes in low vacuum condition at room temperature	
Al deposition by DC sputtering	120 nm thick Al at a rate of 3 nm/minute	
Thermal annealing	570 ºC for 4 hours	
Wet etching	49 wt% HF : 63 wt% HNO$_3$ 5 : 5 litres 10 seconds	
DI water rinse	10 minutes	
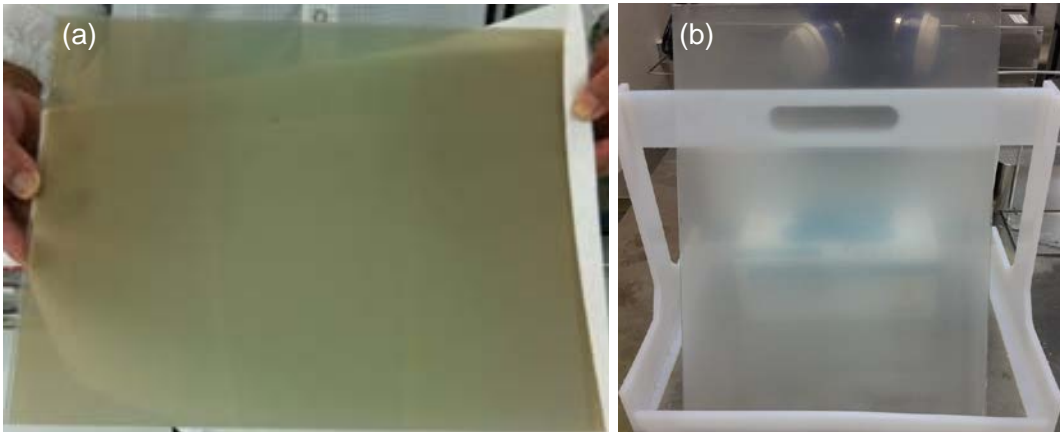
Figure 3-2: A glass sheet (a) after the AIT anneal and (b) after the AIT wet etching and DI water rinse.

3.2.2.1　　AFM and SEM images of a typical AIT glass sheet

Figure 3-3 shows an AFM surface plot and a SEM top view of a typical AIT glass sheet fabricated using SERIS' baseline process recipe. It can be seen that nearly the entire glass surface is textured, which is good for optical scattering [5]. The craters formed in the glass surface have a feature size in the 1-5 μm range. These feature sizes are comparable to the thickness of the poly-Si thin-film diode, which is good enough for light trapping [2].
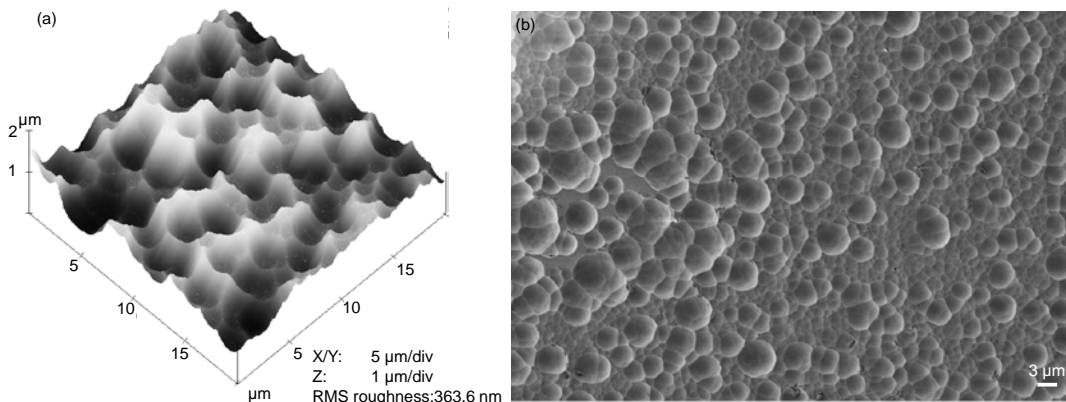
Figure 3-3: (a) AFM surface plot and (b) SEM top view of a typical AIT glass sheet fabricated in SERIS.

3.2.2.2　　Reflectance of AIT glass vs. planar glass

The total and diffuse reflectances of a Borofloat33 glass sheet textured with the baseline AIT process and a planar Borofloat33 glass sheet were measured with the spectrophotometer (PerkinElmer, Lambda 950), as shown in Figure 3-4. The AIT glass sheet has about 1-2% lower total reflectance than the planar glass sheet. Moreover, it has a significantly higher diffuse reflectance than the bare glass sheet. The reflection peak at ~350 nm should be related to iron impurity

level inside the Borofloat33 glass [11]. Reflectance measurements were performed with light incident on the textured glass surface, i.e. in substrate configuration.
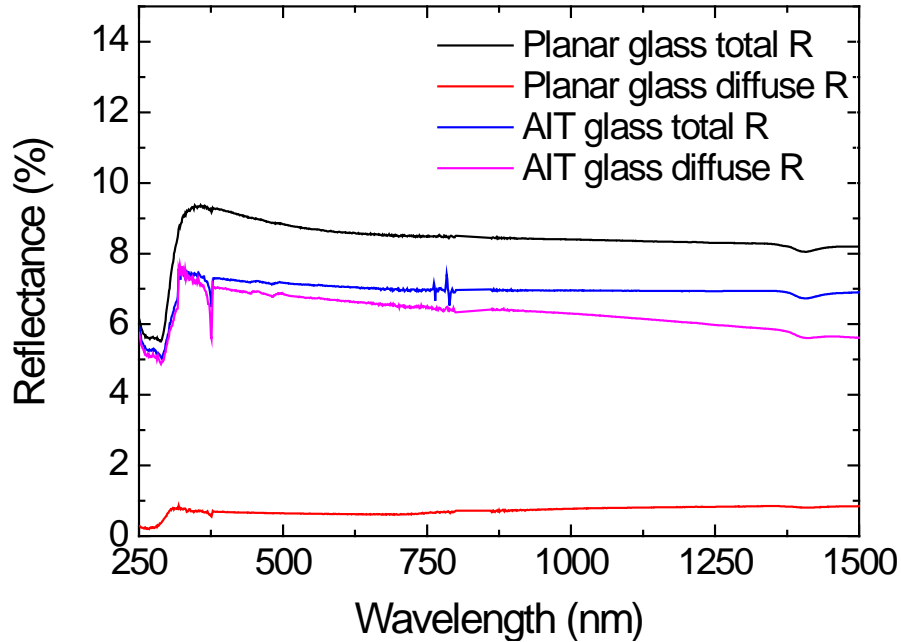
Figure 3-4: Total and diffuse reflectance of an AIT textured borosilicate glass sheet and a planar glass sheet.

3.2.3 Investigation of impact of HF:HNO$_3$ acid ratio on scattering efficiencies of AIT glass

The objective of this study is to investigate the impact of the HF:HNO$_3$ ratio on the optical scattering efficiency of AIT glass. A 30 × 40 cm^2 Schott Borofloat33 glass sheet was cleaned, sputter deposited with an Al film, and then annealed using the process recipe described in Table 3-1. After the annealing it was cut into 12 equal pieces (each with a size of 10 cm × 10 cm). The samples were named BF 1 to BF 12. BF 1 & 2, 3 & 4, 5 & 6, 7 & 8, 9 & 10, and 11 & 12 were

wet etched inside 49 wt% HF : 63 wt% HNO_3 acid mixture with a volume ratio of 1:1, 1:2, 1:3, 1:4, 1:5, and 1:6, respectively. The wet etching time was fixed at 10 seconds for every sample. All samples were then DI water rinsed for 10 minutes and dried by a nitrogen purge. All rinsed & dried glass sheets were studied using an Olympus STM6 optical microscope (OM) in dark field (DF) reflective mode at a magnification of 50 times. Exposure time of an Olympus DP25 digital camera of the optical microscope was set at 1400 ms for every glass sheet. The camera measured the intensity of each pixel of the DF image and gave it a grey-level value. Higher grey-level value means higher brightness of the pixel and hence higher scattering level in the pixel. Mean of the grey level values for each textured glass sheet was retrieved from Olympus analySIS FIVE software of the optical microscope. Haze in transmission at glass/air interface of each glass sheet was measured by the PerkinElmer Lambda 950 spectrophotometer.

Figure 3-5 shows the mean values of DF OM images grey level intensities for samples BF 1 to BF 12. It shows that samples which were wet etched in the acid mixture at a higher HNO_3 volume ratio generally have lower grey level intensity means. The DF OM image is brighter, i.e., has higher grey level intensity mean value, when the glass texture features have a higher scattering efficiency. In other words, according to the data of Figure 3-5, textures generated by the acid mixture with a HF:HNO_3 volume ratio of 1:1 have the highest grey level intensity means and hence the highest scattering efficiency. When the HF acid is diluted with more HNO_3 acid, the scattering efficiencies of the resulting glass textures gradually decrease. Figure 3-6 shows box plots of haze in transmission from 250 to 1500 nm wavelength for samples BF 1 to BF 12. The average haze (small rectangle inside each box in Figure 3-6) gradually decreases when the HNO_3

volume is increased. Based on the data of Figure 3-5 and Figure 3-6, an HF:HNO$_3$ volume ratio of 1:1 was chosen for the AIT glass fabrication in SERIS.
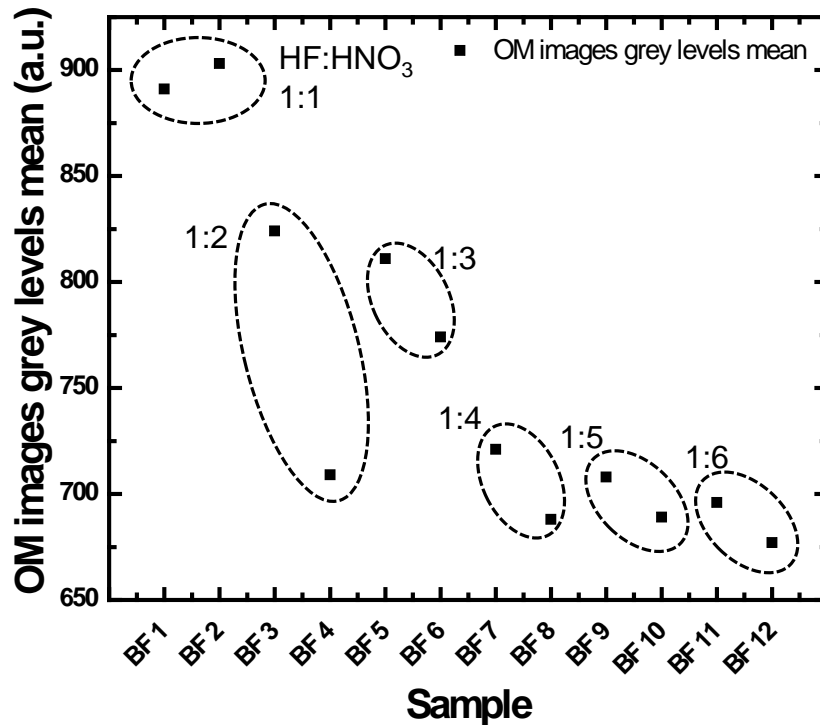
Figure 3-5: Average grey level intensities of optical microscope images for samples BF 1 to BF 12.
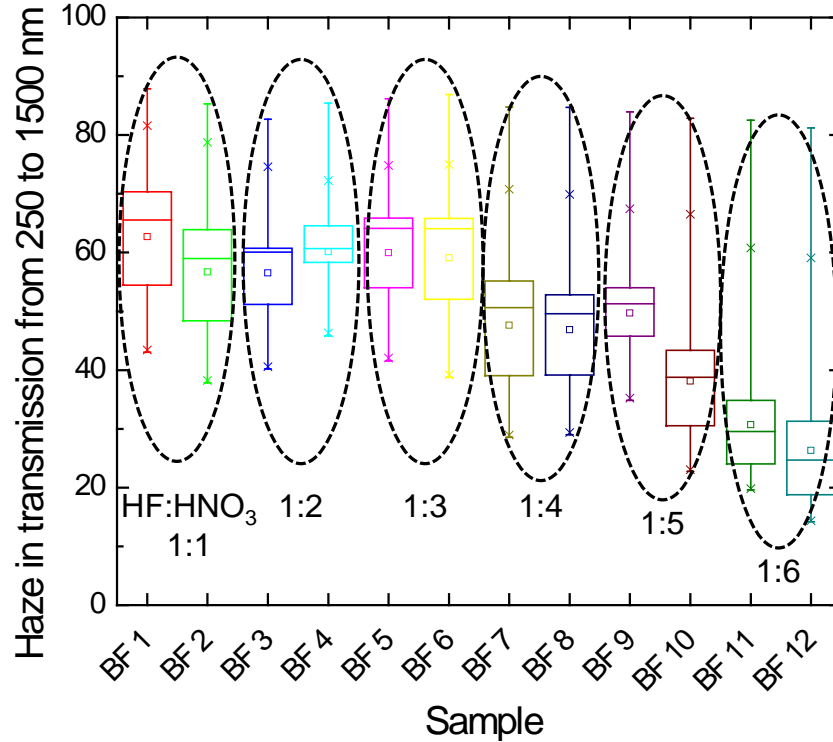
Figure 3-6: Box plots of haze in transmission from 250 to 1500 nm wavelength for samples BF 1 to BF 12.

3.2.4 Up-scaling of the AIT process to pilot line-scale borosilicate glass sheets

3.2.4.1   Introduction

Excellent light trapping approaching the Lambertian limit has recently been reported for SPC poly-Si films formed on AIT glass superstrates with a size of 15 cm × 15 cm [2]. In the present work, we successfully scaled-up the AIT process to a glass size of 30 cm × 40 cm, using 3.3 mm thick borosilicate glass sheets obtained from two manufacturers (Schott, Germany, and Heping Glass Pte. Ltd., China) [6].

3.2.4.2 Experimental details

Four different glass sheets named A-1, A-2, B-1 and B-2 were used in the following experiment. Samples A-1 & A-2 were Borofloat33 glass from Schott, samples B-1 & B-2 were borosilicate glass from the Chinese supplier. They went through the AIT baseline fabrication process as described in Section 3.2.2. An optical microscope (OM) in the reflectance mode (dark field) was used to check the surface topography of the textured glass sheets.

Fabrication of poly-Si thin-film solar cells on the textured glass sheets consisted of the following steps:

- ~70 nm SiN_x by PECVD

- ~2.7 μm (except for sample B-2 which used ~2.0 μm) thick a-Si:H precursor diode deposition by PECVD and then solid-phase crystallization (SPC) at about 600°C for 12 hours.

- Rapid thermal processing (RTP) at a very high temperature (~1000°C) for 1 minute to activate the dopants and remove defects.

To obtain accurate optical measurements, the slightly warped edge regions after RTP were cut off, giving a sample size of about 25 cm × 25 cm. These samples were then divided into 12 pieces of equal size (each ~6 cm × 8 cm). Trans-mittance (T) and reflectance (R) of each sample in superstrate configuration were then measured with an UV-Vis-NIR spectrophotometer (PerkinElmer, Lambda 950) equipped with an integrating sphere. Figure 3-7 illustrates a sample in superstrate configuration. Absorptance (A) was then calculated via $A = 1 - R - T$. Figure 3-8 shows the locations of the spectrophotometer measurements over the 25 cm × 25 cm area.

Incident light

Textured glass

SiN$_x$ AR layer
n$^+$ emitter
p$^-$ absorber
p$^+$ back surface field
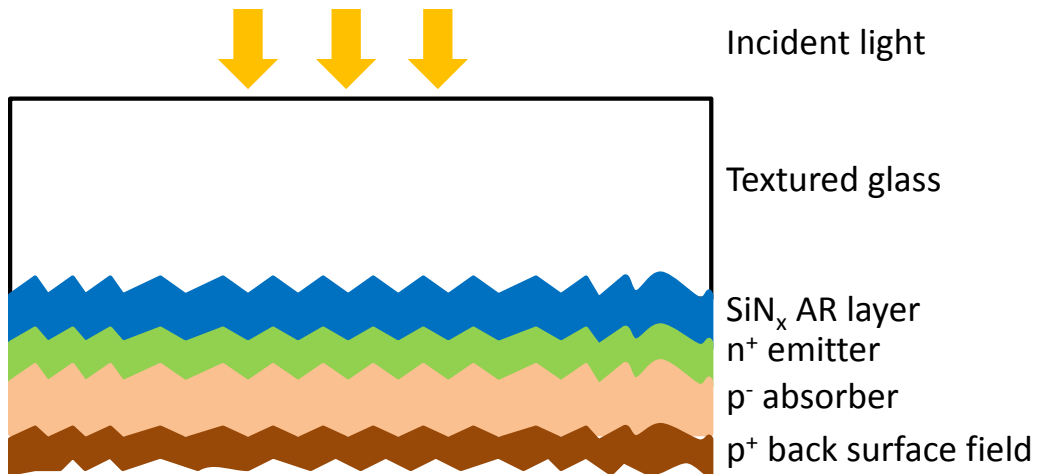
Figure 3-7: Schematic of investigated samples (layer thicknesses not to scale). In superstrate configuration, the incident light enters the solar cell through the glass superstrate.
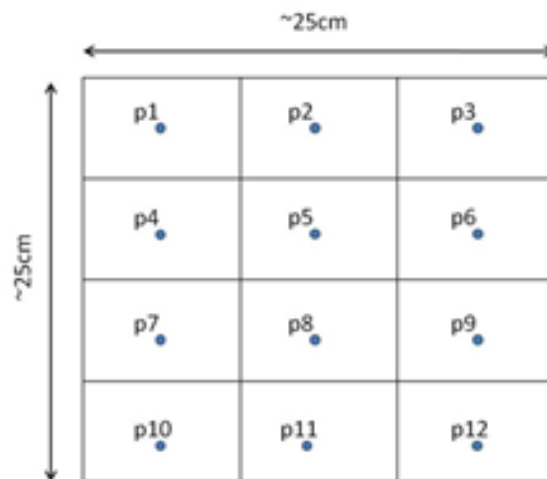
Figure 3-8: Locations of the spectrophotometer measurements on the 25 cm × 25 cm glass sheets.

3.2.4.3   Results and discussion

Figure 3-9 shows the dark field (DF) images of sample A-1 before the SiN$_x$ deposition. More than 95% of the entire glass surface is textured (weakly textured or non-textured areas appear black in a DF image), and thus this texturing process is regarded to be good. It is also seen that the feature size of the texture is in the 1-5 µm range. A few defects are present, whereby these are

52

mostly close to the edge of the glass sheet, as can be seen in Figure 3-9 (b). Theses defects are textured as well and, according to the DF images, do not significantly deteriorate the light scattering properties. Apart from these defects, the glass texture is uniform over the 30 cm × 40 cm area.
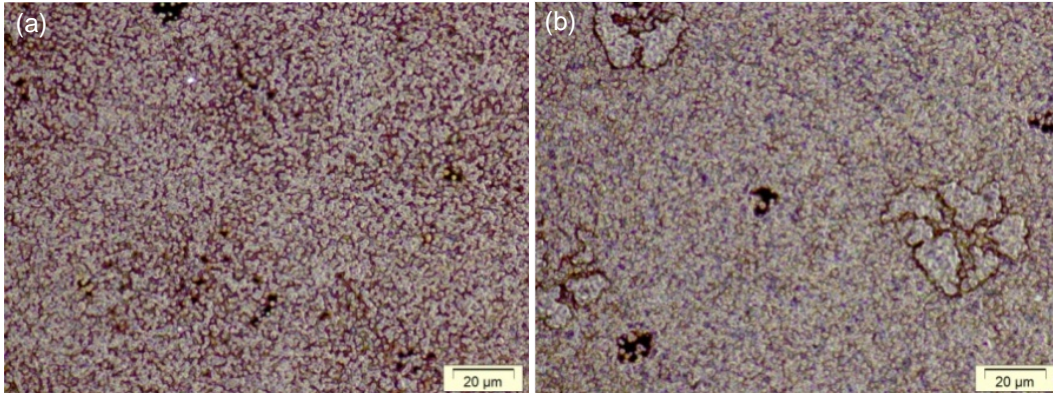
Figure 3-9: Optical microscope dark-field images of AIT textured glass before SiN$_x$ deposition. (a) Centre zone of the A3 sheet. (b) Edge zone (inside 25 cm × 25 cm area). Scattering efficiency in both zones is high. The defects seen in edge zone are textured and do not seem to significantly deteriorate the light scattering performance provided by the textured glass sheet.

The absorptance value at 800 nm wavelength is a good gauge to evaluate the light trapping enhancement resulting from the glass texture [2]. Table 3-2 summarizes the absorptance values at 800 nm of samples A-1 and A-2. The investigated sample structure is shown in Figure 3-7. According to these data, both samples have an average absorptance of ~83% at 800 nm, which matches the calculated absorptance (~81% [2]) if one assumes Lambertian scattering at the cell surfaces. Moreover, the variation of the absorptance across the sample surface is within ± 2.5%, demonstrating that the optical performance of the textured samples is laterally uniform.

Table 3-2: Absorptance values of samples A-1 and A-2 at 800 nm wavelength. The average absorptance value (~83%) matches the Lambertian limit value (~81% [2]). The variation of the absorptance across the sample surface is in the acceptable range (within ± 2.5%).

Sample A-1		Sample A-2	
Location	Absorptance at 800 nm	Location	Absorptance at 800 nm
1	83.7	1	84.1
2	82.7	2	82.9
3	81.5	3	82.6
4	84.2	4	83.3
5	84.2	5	83.6
6	83.7	6	83.9
7	84.4	7	83.0
8	83.7	8	83.5
9	83.8	9	84.0
10	83.2	10	82.9
11	81.5	11	81.0
12	80.6	12	80.5
Average	83.1	Average	82.9
Range	+1.3/-2.5	Range	+1.1/-2.5
Lambertian value	81.1	Lambertian value	81.1

To further compare the experimental absorptance data with the Lambertian limit value for the full wavelength range, the pieces with the highest/lowest 800 nm absorptance values of both samples are chosen. The absorptance results for the wavelength range 300-1500 nm are shown in Figure 3-10. At short wavelengths (300-500 nm), the measured values are generally higher than the calculated values, which is attributed to the reduced reflection losses due to the surface texture ('multi-bounce' effect [2]). In the wavelength range 500-800 nm, the agreement between measured and calculated absorptance values is quite good. In the long-wavelength range (800-1500 nm) the measured values are much higher than the calculated values. This can be explained by: i) measured absorptance above wavelength 800 nm is overestimated due to measurement error, as described in Section 2.5.2.3; and ii) the calculated values likely under-estimate the glass absorption in wavelength range 800-1500 nm. Works done in

this PhD study to estimate glass absorption will be presented in detail in Chapter 5.
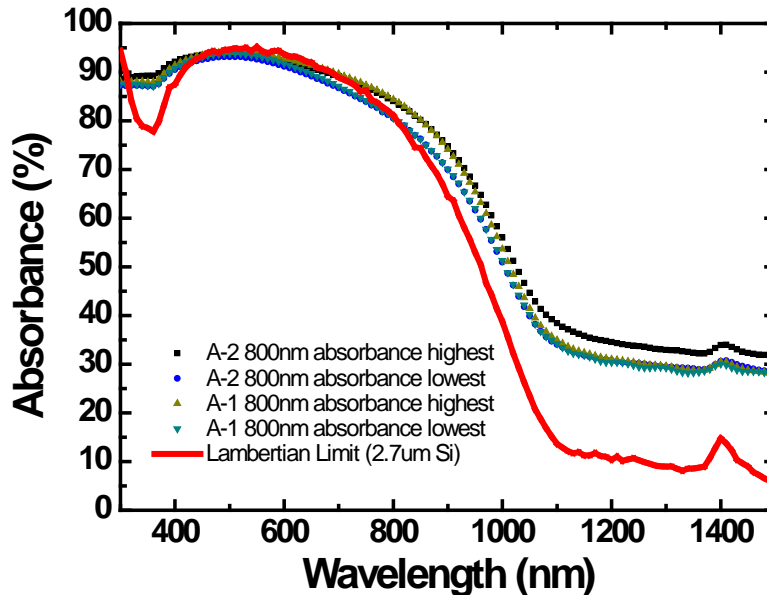
Figure 3-10: Measured absorptance curves of samples A-1 and A-2 (symbols). The variation among the measured four locations is small. Also shown (red line) is the calculated absorptance for a poly-Si thickness of 2.7 µm, assuming Lambertian scattering at the cell surfaces [2].

For sample B-1, 3 points on its 20 cm × 20 cm surface were chosen to measure the absorptance. Each point is ~3 cm away from the nearest edge. The measured absorptance curves of the poly-Si sample are plotted in Figure 3-11, together with the calculated Lambertian limit curve [2]. The average absorptance at a wavelength of 800 nm is ~80%. The absorptance plot shows the same trend as seen in Figure 3-10. At intermediate wavelengths, the measured absorptance also agrees well with the calculated Lambertian limit curve for a 2.7 µm thick poly-Si film. The variation between the three measured locations is small, which implies a good uniformity.
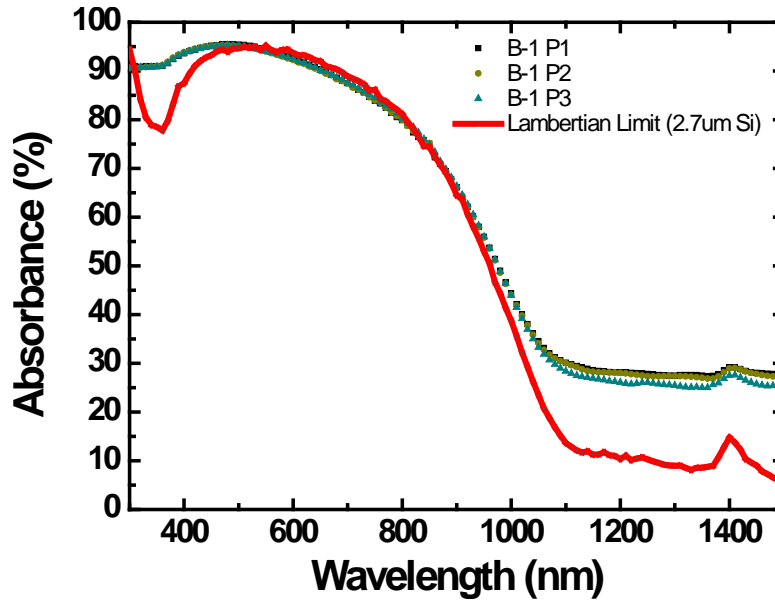
Figure 3-11: Measured absorptance curves of sample B-1 (symbols). The variation among the measured three locations is small. Also shown (red line) is the calculated absorptance for a poly-Si thickness of 2.7 μm, assuming Lambertian scattering at the cell surfaces [2].

For sample B-2 (area 25 cm × 25 cm, poly-Si thickness 2.0 μm), the absorptances were measured at five locations (1, 2, 4, 7 and 8 in Figure 3-8). The measured absorptance curves are again compared with the calculated Lambertian limit curve, as shown in Figure 3-12. At intermediate wavelengths, the measured absorptance curves agree reasonably well with the calculated curve.
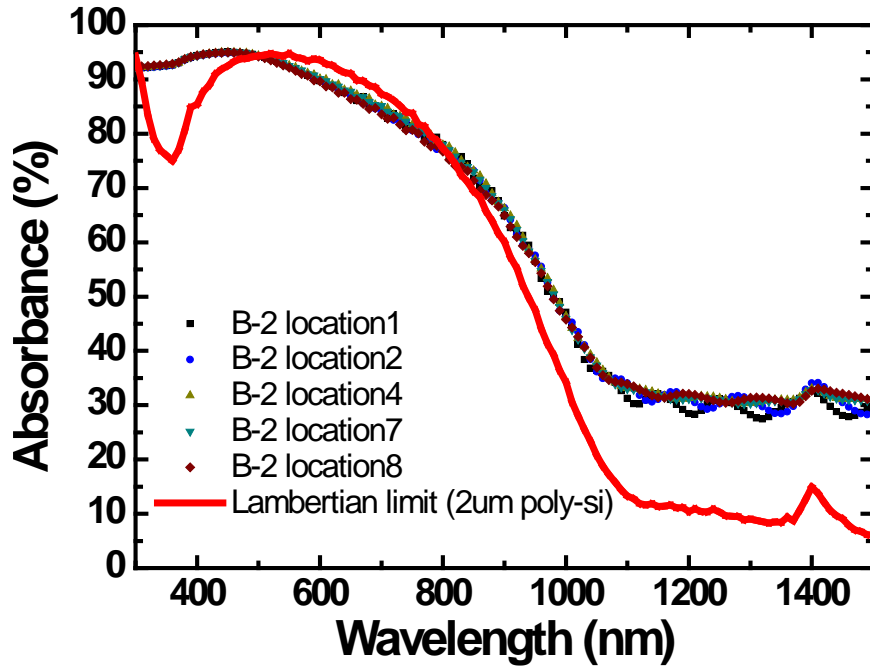
Figure 3-12: Measured absorbances of sample B-2 (symbols). The variation among the measured five locations is small. Also shown (red line) is the calculated absorptance for a poly-Si thickness of 2.0 μm, assuming Lambertian scattering at the cell surfaces [2].

3.2.4.4   Conclusions

In this work, the AIT (aluminium-induced texture) glass texturing process was successfully scaled up to pilot line-scale borosilicate glass sheets measuring 30 cm × 40 cm. The glass sheets were obtained from two different manufacturers, demonstrating that the AIT process can be applied to a variety of borosilicate glasses. Poly-Si thin-film solar cells fabricated on these AIT glasses show a good lateral uniformity of the optical absorption (non-uniformity below ± 2.5%). The optical absorption of poly-Si films made by SPC on these AIT glass sheets is excellent. The AIT process is thus a promising glass texturing method for PECVD SPC poly-Si thin-film solar cells on glass.

3.3   Fabrication of poly-Si films on pilot line-scale AIT glass

In this section, some process changes introduced to improve the SPC poly-Si diode quality on AIT glass are described. The 1-Sun V_{OC} and the pseudo fill factor (*pFF*) are significantly enhanced by introducing double barriers between the AIT glass sheet and the poly-Si thin-film and by increasing the a-Si:H precursor PECVD deposition temperature (Section 3.3.1). A partially masked AIT method is developed to help characterize poly-Si thin-films on AIT glass (Section 3.3.2).

3.3.1 Double barriers (SiN$_x$ + SiO$_2$) and increased a-Si:H precursor PECVD deposition temperature

After optimizing the emitter doping concentration [7], the RTP process [8], and the hydrogenation process [9], 2 μm thick poly-Si thin-film solar cells on A3 size planar glass sheets (samples PS1_500C and PS2_500C in Figure 3-13 (a)&(b)) with average 1-Sun V_{OC} of 461 mV and average *pFF* of 75.6% were fabricated. However, 2 μm thick poly-Si thin-film solar cells on AIT glass fabricated using the same process conditions (samples AS1_500C and AS2_500C in Figure 3-13 (a)&(b)) were found to have much lower 1-Sun V_{OC} (with average of 430 mV) and *pFF* (with average of 71.6%). The diode quality on AIT glass was found to improve by depositing an additional 100 nm thick silicon dioxide (SiO$_2$) barrier layer between the AIT glass surface and the silicon nitride layer. The average 1-Sun V_{OC} improved to 463 mV and the average *pFF* improved to 75.8% for 2 μm

58

thick poly-Si thin-film solar cells on AIT glass with double barriers (samples AD1_500C, AD2_500C and AD3_500C in Figure 3-13 (a) & (b)). The benefit of the additional barrier on the diode quality can be explained by i) less metal and nitrogen contaminations in the Si film; or ii) a more favourable stress in the Si during crystallization [5]. By increasing the deposition temperature of the a-Si:H precursor diode, the diode quality can be further improved for poly-Si thin-film solar cells on AIT glass with double barriers. An average 1-Sun V_{OC} of 484 mV and an average *pFF* of 78.2% for 2 µm thick poly-Si thin-film solar cells on AIT glass with double barriers and with the PECVD temperature increased from 500 °C to 550 °C were achieved (sample AD1_550C in Figure 3-13 (a)&(b)). With some more efforts, we believe that we can meet the voltage benchmark (500 mV) and the *pFF* benchmark (80%) [10].
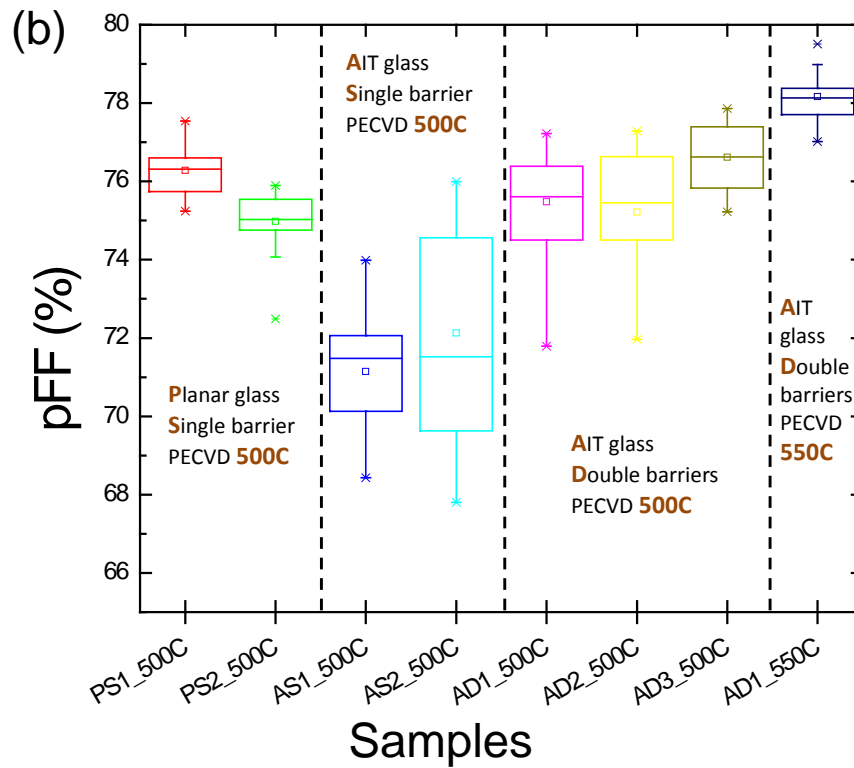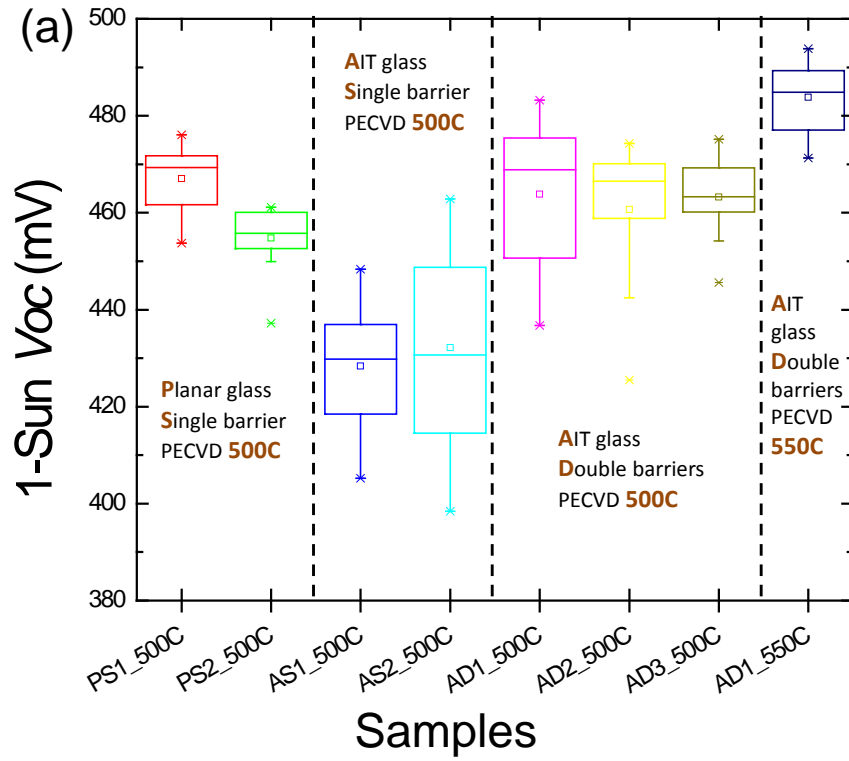
Figure 3-13: Box plots of (a) 1-Sun V_{OC} and (b) pFF for 2 μm thick poly-Si thin-film solar cells on planar/AIT glass, with single/double barriers, and with PECVD a-Si:H deposition temperature of 500°C and 550°C.

3.3.2 Partially masked AIT method

The partially masked AIT method is developed to produce a flat or un-textured zone on an A3 size AIT glass sheet. Therefore poly-Si thin-film solar cells on both flat and textured glass surfaces can be fabricated in the same process run. The poly-Si solar cells on the flat glass zone can serve as benchmarking devices of poly-Si solar cells on textured glass surfaces.

Figure 3-14 shows how the masked AIT process works so that both planar and textured areas can be created on the same glass sheet. A 3-inch diameter Si wafer was used as a mask and attached to an A3 size glass sheet, as shown in Figure 3-14(a). The A3 size glass sheet was then coated with Al by sputtering, whereas the glass surface masked by the Si wafer remained free of Al (Figure 3-14(b)). The Si wafer was then detached from the glass sheet, see Figure 3-14(c). The glass sheet was then annealed at 570°C. Since there was no Al coated at the previously masked glass surface, there was no redox reaction and hence no glass roughening after the annealing in the previously masked glass surface (Figure 3-14(d)). The glass sheet was then wet etched in an $HF:HNO_3$ acid mixture and rinsed by DI water, resulting in the structure shown in Figure 3-14(e).
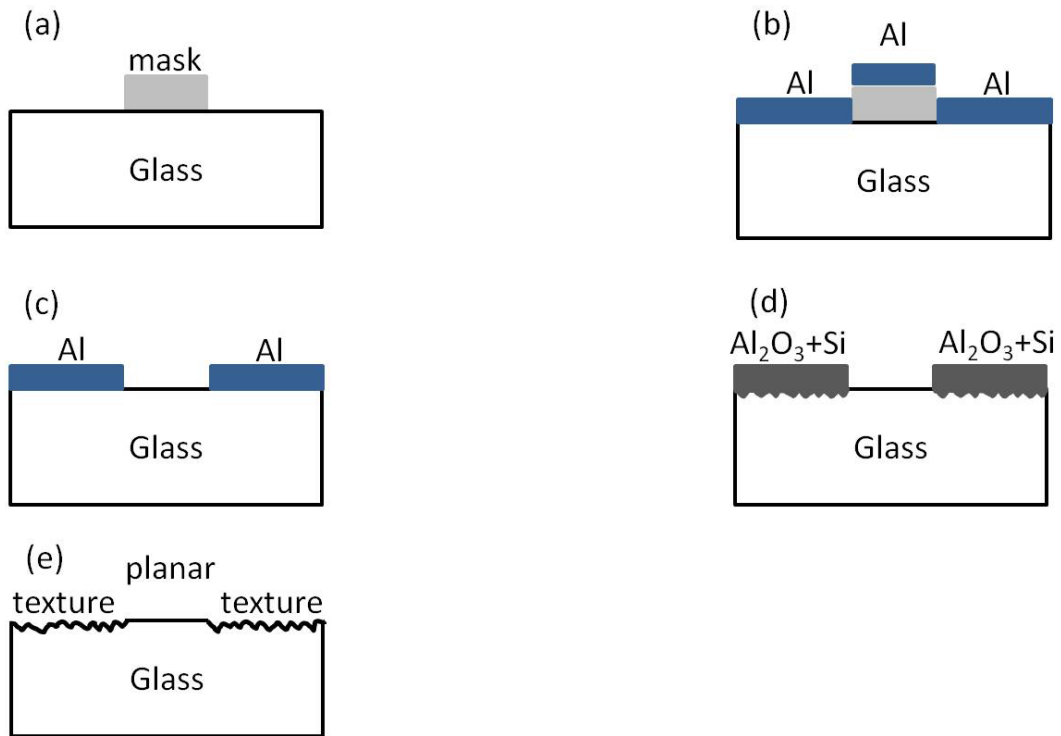
Figure 3-14: Schematic of the masked AIT method. (a) A mask is put on the glass sheet before Al deposition; (b) Al deposition; (c) Mask removal; (d) after AIT annealing; and (e) after HF:HNO$_3$ wet etch.

A photo of an A3 size borosilicate glass sheet after the HF:HNO$_3$ wet etch and DI water rinse is shown in Figure 3-15. The circular area in the centre is flat and transparent, whereas the other areas are textured and hazy.
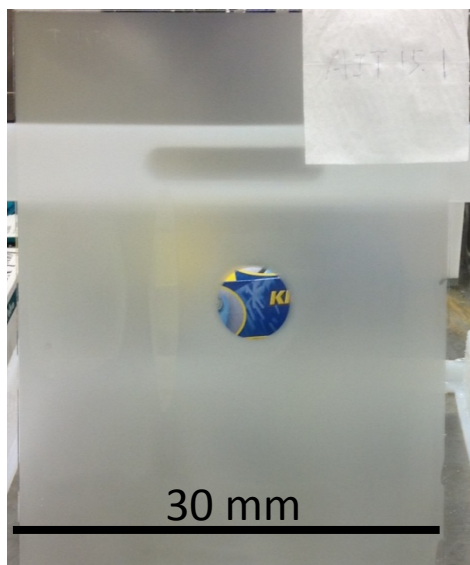
Figure 3-15: An A3 size glass sheet processed with the partially masked AIT method. The circle in the centre is planar glass whereas the remaining regions of the glass sheet are textured.

3.4 Summary

In this chapter, a process was developed to fabricate AIT glass in pilot line scale (30 cm × 40 cm). It is demonstrated that the AIT glass texturing technique is scalable with good optical uniformity. The quality of SPC poly-Si diodes on AIT glass has been significantly improved by introducing an additional SiO_2 barrier and by increasing the deposition temperature of the a-Si:H precursor diode. Poly-Si thin-film solar cells on AIT glass with a 1-Sun V_{OC} of 500 mV and *pFF* of 80% are within reach. A partially masked AIT glass texturing process was developed for pilot line-scale glass sheets. The masked AIT technique will be beneficial in the future for better controlling and further optimising the fabrication process of SPC poly-Si solar cells on AIT glass sheets.

References (Chapter 3)

[1] P.J. Gress, P.I. Widenborg, S. Varlamov, A.G. Aberle, Wire bonding as a cell interconnection technique for polycrystalline silicon thin-film solar cells on glass, Progress in Photovoltaics: Research and Applications, 18 (2010) 221-228.

[2] G. Jin, P.I. Widenborg, P. Campbell, S. Varlamov, Lambertian matched absorption enhancement in PECVD poly-Si thin film on aluminum induced textured glass superstrates for solar cell applications, Progress in Photovoltaics: Research and Applications, 18 (2010) 582-589.

[3] H. Cui, M. Green, P. Campbell, O. Kunz, S. Varlamov, A photovoltaic light trapping estimation method for textured glass based on surface decoupling calculation, Solar Energy Materials and Solar Cells, 109 (2013) 82-90.

[4] Available: http://www.hepingglass.com/ (accessed on 6 December 2013)

[5] M. Keevers, T.L. Young, U. Schubert, R. Evans, R.J. Egan, M.A. Green, 10% efficient CSG minimodules, Proc. 22nd European Photovoltaic Solar Energy Conference, Milan, 2007, pp. 1783.

[6] Y. Huang, P.I. Widenborg, A.G. Aberle, Up-scaling of the AIT glass texturing method to pilot line-scale borosilicate glass sheets, in: Proc. 26th European Photovoltaic Solar Energy Conference, Hamburg, 2011, pp. 2750 - 2753.

[7] A. Kumar, H. Hidayat, C. Ke, S. Chakraborty, G.K. Dalapati, P.I. Widenborg, C.C. Tan, S. Dolmanan, A.G. Aberle, Impact of the n+ emitter layer on the structural and electrical properties of p-type polycrystalline silicon thin-film solar cells, Journal of Applied Physics, 114 (2013), 134505.

[8] H. Hidayat, A. Kumar, F. Law, C. Ke, P.I. Widenborg, A.G. Aberle, Impact of rapid thermal annealing temperature on non-metallised polycrystalline silicon thin-film diodes on glass, Thin Solid Films, 534 (2013) 629-635.

[9] H. Hidayat, P.I. Widenborg, A. Kumar, F. Law, A.G. Aberle, Static large-area hydrogenation of polycrystalline silicon thin-film solar cells on glass using a linear microwave plasma source, IEEE Journal of Photovoltaics, 2 (2012) 580-585.

[10] H. Hidayat, Post-crystallisation treatment and characterisation of polycrystalline silicon thin-film solar cells on glass, PhD thesis, National University of Singapore, 2013.

[11] P.K. Whitman, D. Hahn, T. Soules, M. Norton, S. Dixit, E.E. Donohue, J. Folta, W. Hollingsworth, M. Maienschein-Cline, Performance of thin borosilicate glass sheets at 351-nm, in: Proceedings of SPIE - The International Society for Optical Engineering, 2005, pp. 333-342.

Chapter 4   A phenomenological model of the AIT process

4.1   Introduction

The solid state reaction between aluminium and silicon oxide has been investigated by several authors. In the temperature range between 400 °C and the melting point of Al (~660 °C), Prabriputaloong and Piggott [1] observed that quartz (i.e., crystalline silicon oxide) has a higher activation energy (2.78 eV) than vitreous silica (1.34 eV) when reacting with evaporated aluminium. Black [2] used the white light interferometry method to measure the remaining thermally grown SiO_2 (original oxide thickness 900 nm) after reaction with evaporated aluminium and obtained an activation energy of 2.56 eV in the temperature range 400-550 °C. Godfrey and Green [3] observed that the electrical degradation of the $Al/SiO_x/p$-Si contact of MIS solar cells in the temperature range 270-400 °C is governed by an activation energy of 2.56 eV, which they attributed to the reduction of the silicon oxide by the aluminium layer. Forbes and Zukotynski [4] measured an activation energy of 2.3 eV in the temperature range 440-500 °C, using 1000 nm thermally grown silicon oxide and 2000 nm evaporated aluminium. A very low activation energy of 0.98 eV for ultrathin SiO_x (1.3 nm) in the temperature range 213-369°C was reported by Brendel and Hezel [5]. Using a

thermal pyrogenic oxide and sputtered aluminium (containing 2 % copper and 0.5 % silicon), Dadabhai *et al.* [6] found that the activation energy for the reaction is approximately 2 eV. Although the solid state reaction between Al and SiO_2 has been extensively studied in microelectronic technologies, there has been no detailed study about the key feature of the AIT method, the solid phase reaction between aluminium and glass.

The scope of this chapter is to gain a deeper understanding of the physical mechanisms behind the AIT process to enable further improvement of the glass texture and, in the end, improved performance of solar cells. In particular, the details of the silicon growth process during the reaction between Al and glass (consisting mainly of SiO_2) are studied. Raman, energy-dispersive X-ray spectroscopy (EDX) and X-ray diffraction (XRD) show that in the AIT process, Si is reduced out from SiO_2 and forms crystalline silicon (c-Si) crystals growing upwards from the glass-aluminium interface while, simultaneously, Al_2O_3 grows into the glass as crater shaped nodules and also into the aluminium over-layer. The *in-situ* XRD method is used to extract the activation energy for the c-Si growth occurring in the AIT process. Finally, a phenomenological model of the AIT process is proposed. The results of this work were published in Ref. [7].

4.2   Experimental details

Borosilicate glass sheets with a thickness of 3.3 mm were used in this study. The chemical composition of the used borosilicate glass is approximately 81 % SiO_2,

13 % B_2O_3, 4 % Na_2O/K_2O, and 2 % Al_2O_3 [8]. Cleaning of the glass sheets (30×40 cm^2, planar) occurred in a dish washer (Miele) using alkaline detergent (STERIS CIP100) and acid detergent (CIP200), followed by drying in the dish washer. Then, an Al film was deposited onto one surface by RF sputtering in argon atmosphere. The rectangular Al target with a dimension of 43.2 cm (L) $\times$ 5.72 cm (W) $\times$ 0.64 cm (H) had a purity of 99.999 %. The deposition parameters were: power 215 W, pressure 0.003 Torr, Ar gas flow 25 sccm, deposition time 40 minutes. During the deposition, the non-heated substrate carrier was oscillating over the Al target to achieve good film uniformity. The resulting Al thickness was about 120 nm, with a uniformity of $\pm$ 8 %. The sheet was then cut into 4 samples of equal size (15 cm $\times$ 20 cm) labelled A1, A2, A3, and A4. Each sample was then annealed at 570 °C in a nitrogen-purged atmospheric-pressure box furnace. The annealing time for each sample was: A1 0.5 hour, A2 1 hour, A3 2 hours, and A4 3 hours. The centre zones of the annealed samples were then checked by using an optical microscope (OM) in the bright-field (BF) reflective mode. Raman measurements were then performed using a Raman microscope (Renishaw, InVia) with a laser wavelength of 514 nm and a laser spot size of 1 μm. The Raman exposure time was set to 1 second. The laser power reaching the sample surface was about 19 mW.

An 1 cm $\times$ 1 cm fully reacted piece labelled A4-1 was then cut from sample A4. The Al_2O_3 was selectively wet etched using a standard RCA-1 clean (1 NH_4OH : 1 H_2O_2 : 3 DI water at 80 °C for about 5 minutes), and followed by a DI water rinse. As a result, the glass surface with the grown c-Si crystals was exposed. The surface morphology of sample A4-1 was then studied by scanning electron microscopy (SEM) (Zeiss, Auriga CrossBeam FIB/SEM workstation) and tapping-

mode AFM (Veeco, Dimension). The cross-section profile was characterized by SEM (milled by FIB Ga ions and imaged by SEM). To protect the glass surface during FIB Ga ion milling, a 20(L) $\times$ 3(W) μm^2 platinum layer was coated on the surface by FIB before trench milling. Energy-dispersive X-ray spectroscopy (EDX) analysis was then used to identify the elemental composition of the crater shaped nodules. The EDX analysis was performed in an AMETEK EDAX system attached to a NOVA NanoSEM 230 SEM station.

To understand the kinetics of the c-Si growth in aluminium and at the glass interface, *in-situ* XRD was used (Panalytical, model X'pert Pro equipped with Anton Paar HTK1200N high-temperature chamber). A wavelength of 1.54 Å (copper target) was used and the high-temperature chamber was maintained at a pressure of 6×10^{-6} mbar. To identify the silicon peaks, sample A4-1 was scanned from 20 ° to 70 ° using XRD.

Four 0.8 cm $\times$ 0.8 cm planar 3.3 mm thick borosilicate glass sheets (B1, B2, B3, and B4) with 120 nm sputtered Al on one surface were then annealed in the high-temperature chamber at 4 different temperatures (500, 510, 520 and 530 °C) to obtain the activation energy of the reaction.

4.3 Results and discussion

4.3.1 Investigation of Al/glass samples using optical microscopy

Optical microscope bright field images on samples annealed at 570 °C for different times are shown in Figure 4-1. Before the anneal process, the Al film was uniform and showed a white appearance in the bright field image (not shown here). After 0.5 hour annealing we observed two objects 1 and 2, see Figure 4-1(a). The thermal expansion coefficient difference between the borosilicate glass sheet and the Al film results in a large thermal stress [9]. As a result, hillocks were formed in some regions of the Al film, see object 1 in Figure 4-1(a), while in some other regions of the Al film voids were formed (object 2 in Figure 4-1(a)), thereby exposing the glass surface. After 1 hour annealing, in Figure 4-1(b), besides Al hillocks and Al voids, we observed another object (3). Object 3 was green coloured under the optical microscope and had a dendritic growth pattern. The size of object 3 is less than 5 μm in Figure 4-1(b). The dendritic objects get larger with increasing annealing time. They are numerically labelled as 4–6 in Figure 4-1(c) after 2 hours annealing and 7 in Figure 4-1(d) after 3 hours annealing. After 3 hours of annealing, no further changes were observed, indicating that the reaction had stopped.
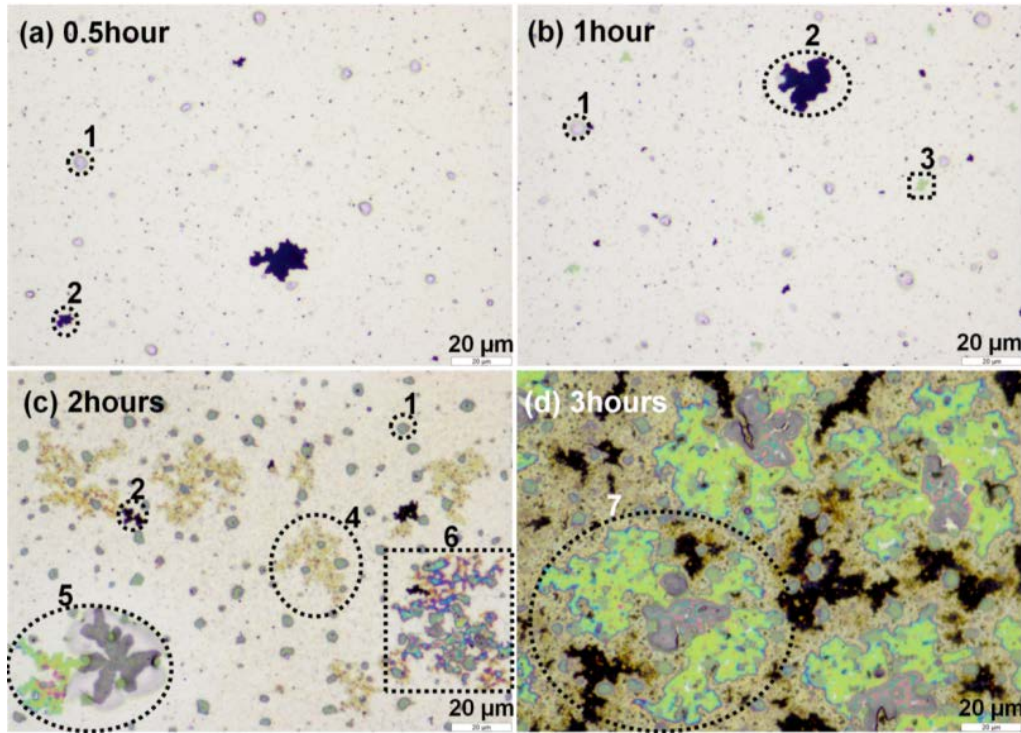
Figure 4-1: Optical microscope images taken in the bright field reflective mode. (a) centre area of sample A1 after 0.5 hour annealing at 570 °C, (b) centre area of sample A2 after 1 hour annealing, (c) centre area of sample A3 after 2 hours annealing, and (d) centre area of sample A4 after 3 hours annealing. The scale bar is 20 μm for all images. Objects observed are numbered and marked with a dashed line.

4.3.2 Raman spectroscopy analysis

All objects marked in Figure 4-1 were examined by Raman spectroscopy. Figure 4-2 shows the Raman spectrum of object 3 observed in Figure 4-1(b). The narrow Raman peak at 519 cm^{-1} indicates that object 3 is crystalline silicon (c-Si) [10]. Objects 4-7 had all similar peaks (not shown here) at 519 cm^{-1} and hence also consist of c-Si. Only objects 1 and 2 in Figure 4-1 did not contain any c-Si according to Raman measurements.
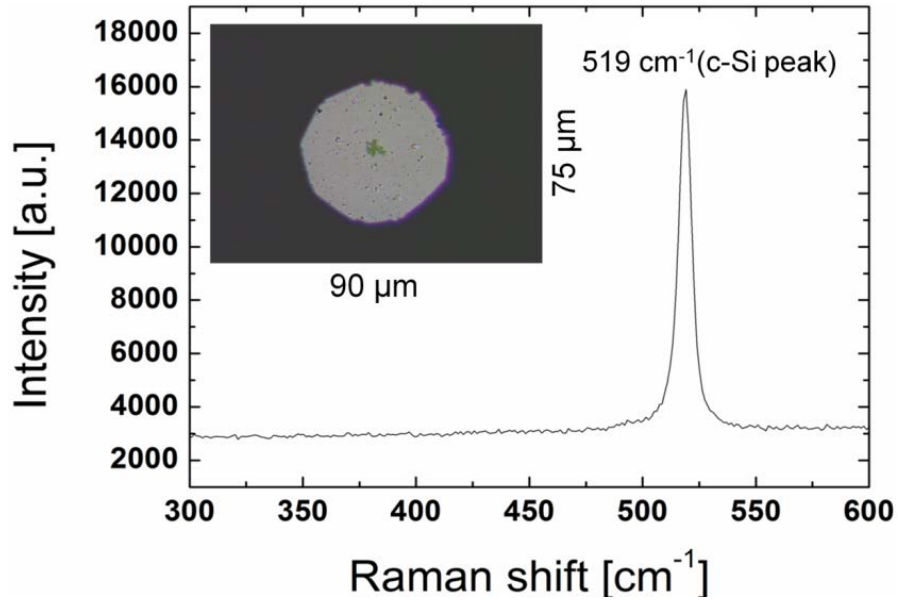
Figure 4-2: Raman spectrum of object 3 of Figure 4-1(b). The inset was the view under the Raman tool's microscope. The green dendritic object in the centre was illuminated by the Raman laser beam (diameter ~1 µm).

4.3.3 Morphology study by SEM, AFM, and element analysis by EDX

4.3.3.1 Plan-view SEM analysis

After receiving a RCA treatment sample A4-1 was examined by SEM, see Figure 4-3. Some charging effects are present in the SEM image in Figure 4-3(a) despite the use of a low gun energy of 0.5 keV. The dendritic objects in Figure 4-3(a) were c-Si (confirmed by Raman spectroscopy). For the fully annealed sample A4-1, the c-Si was not joined together to form a continuous film but appeared as standalone clusters. The cluster size is of the order of 100 µm. To minimize the charging effect and to obtain informative images under a higher magnification, A4-1 was sputter coated with a ~8 nm thick layer of gold. A SEM plan-view image of the surface area among silicon clusters was then taken under higher magnification, as shown in Figure 4-3(b). The surface between the Si

clusters of sample A4-1 consists of numerous small-area zones with rough surfaces, which are labelled "nodule" in Figure 4-3(b), surrounded by smooth surface areas. The nodules have a size of the order of 1 μm. The nodules are randomly distributed, with a typical spacing of a few μm.
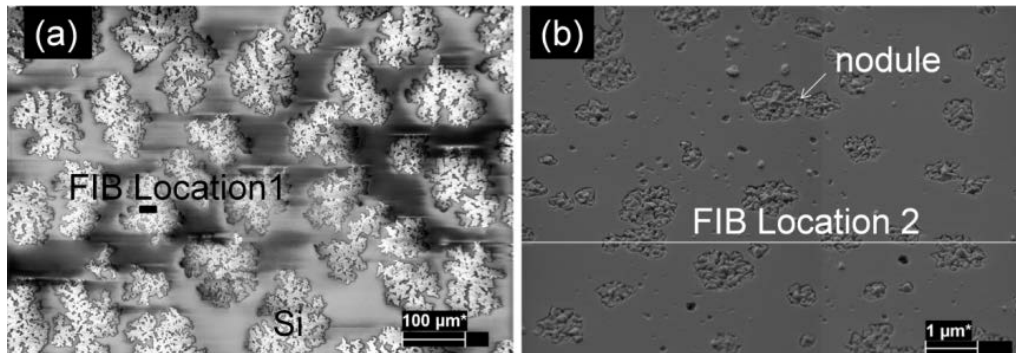
Figure 4-3: SEM plan-view image of sample A4-1. (a) Low-magnification (142X) view of silicon clusters; (b) higher-magnification view (11000X) of surface area in between the silicon clusters seen in (a). FIB locations 1 and 2 (see lines in images) represent two different FIB cross section locations discussed in section 4.3.3.2. Location 1 is on top of a silicon cluster. Location 2 crosses several nodules observed on the glass surface in between the silicon clusters. Image (a) was taken using electron beam energy of 0.5 keV to lower the charging effect, while image (b) was taken using electron beam energy of 5 keV after coating the sample with a ~8 nm thick layer of gold.

4.3.3.2   Cross-sectional SEM analysis

After milling trenches with the FIB, SEM was used to investigate the cross-sectional profile at the two FIB locations as shown in Figure 4-3(a) and (b). Location 1 represents the silicon cluster covered area. Location 2 represents the area that is free of silicon clusters. As can be seen in Figure 4-4, nodules are embedded in the glass and exist both in the area free of Si clusters (as shown in Figure 4-4 (a) & (b)) and under Si clusters, as can be seen in Figure 4-4(c). Based on Figure 4-3 and Figure 4-4, it is reasonable to conclude that the nodules are present everywhere along the glass surface. The sizes of nodules and distances between them are in the order of 1 μm. The nodules are crater shaped

with width < 5 µm and depth < 1 µm, as can be seen in Figure 4-4 (b) and (c). The silicon layer of the silicon clusters is continuous, but is not of uniform thickness. The average thickness of the Si layer seen in Figure 4-4(c) is at an order of 100 nm.
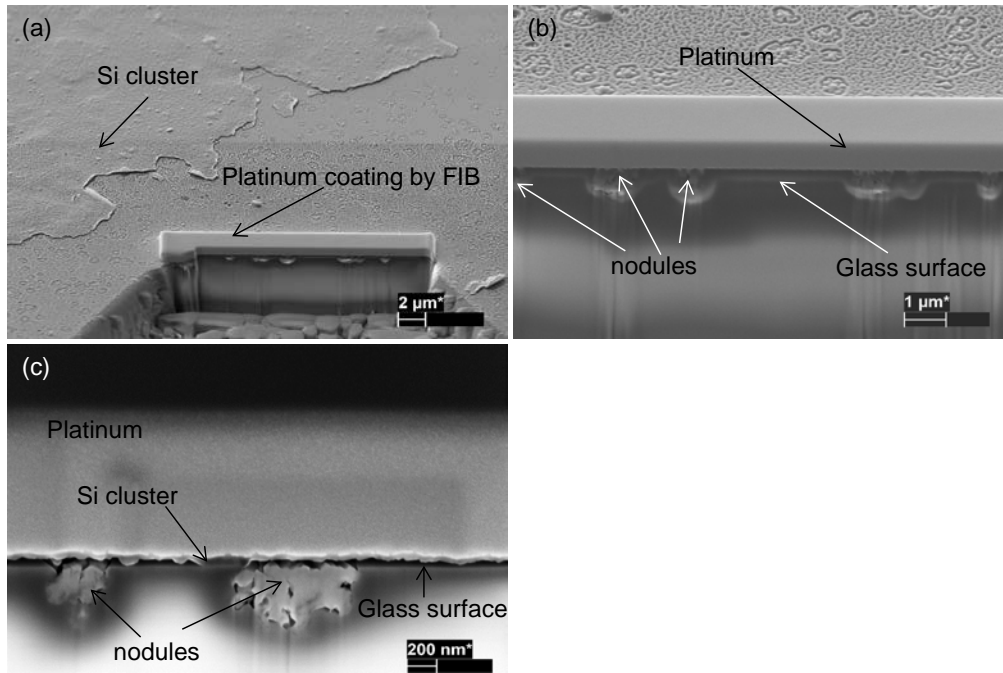
Figure 4-4: SEM cross-sectional view of sample A4-1. Images (a) and (b): SEM cross-section at Si cluster free area – corresponding to location 2 in Figure 4-3(b); and image (c): Si cluster - corresponding to location 1 in Figure 4-3(a). The 20(L) × 3(W) µm2 platinum layer visible in (a) and (b) was coated onto the surface by FIB before trench milling to protect the glass surface during FIB milling. All SEM images were taken using electron beam energy of 5 keV.

4.3.3.3   EDX analysis

To further investigate the nodule structures visible in Figure 4-3 and Figure 4-4, EDX was used. Figure 4-5 shows the EDX result of nodules observed in Figure 4-4 (b) and (c), demonstrating that the nodule structures mainly contain the elements Al and O, most likely in the form of Al_2O_3. As mentioned previously, sample A4-1 had an RCA-1 treatment which would etch Al_2O_3. As can be seen in Figure 4-4(b), the nodule structure has been partially removed whereas the

nodule structure in Figure 4-4(c) is fully intact, most likely due to the shielding effect from the overlying Si cluster during the RCA-1 treatment.

An EDX analysis was also done on a fully annealed AIT sample after the thermal anneal (i.e., without RCA-1 treatment). It shows that Al_2O_3 exists predominately in c-Si cluster free areas (EDX spectra not shown here).
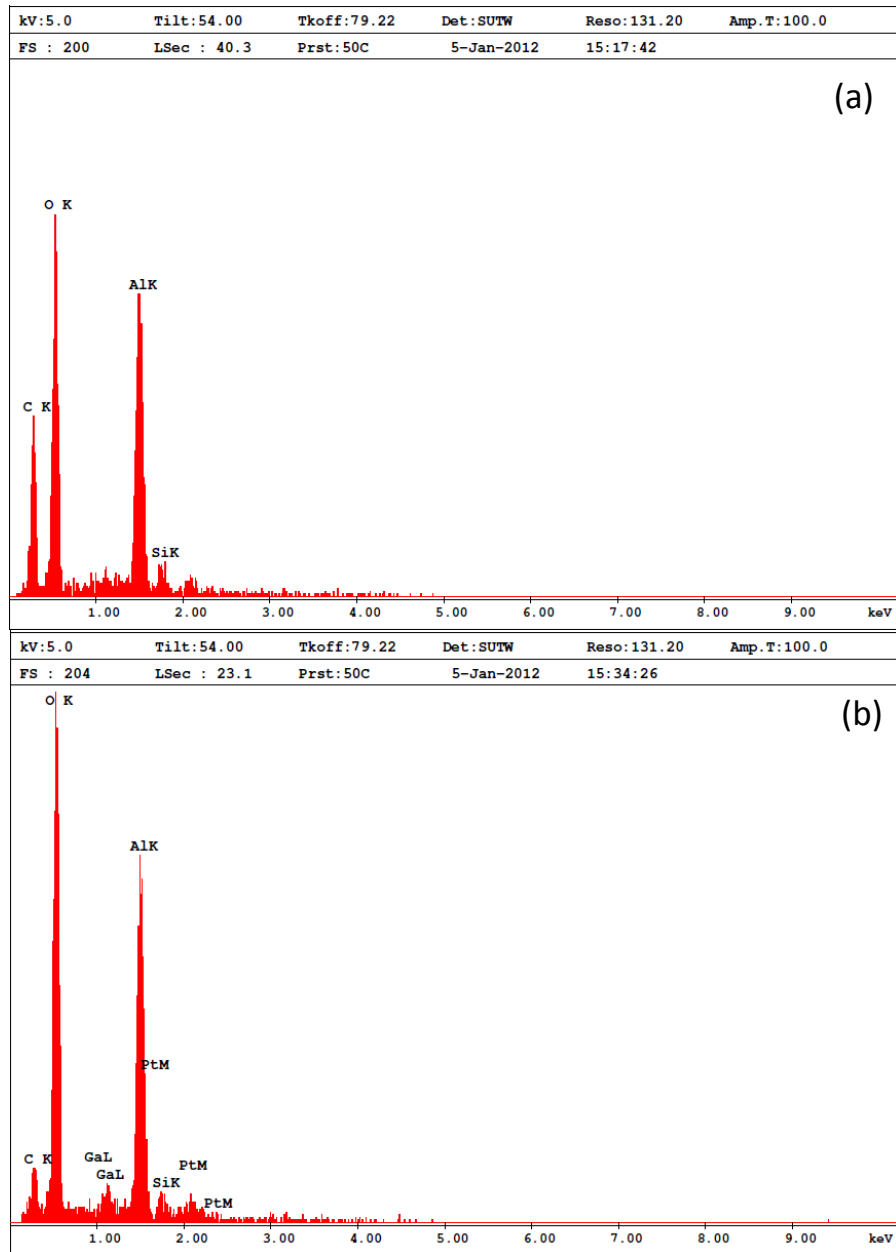
Figure 4-5: EDX results of nodule structures seen in (a) Figure 4-4(c) and (b) Figure 4-4(b). The EDX analysed zone size of (a) is about 0.20 × 0.22 μm^2 and that of (b) is about 0.80 × 0.14 μm^2.

4.3.3.4   AFM analysis of crystalline silicon clusters

AFM was used to study the topology of the c-Si clusters seen in Figure 4-3(a). A top-view image and the corresponding surface plot image are shown in Figure 4-6. They clearly reveal that the c-Si cluster is located above the glass surface. The height difference between the c-Si surface and the glass surface is about 100 nm.
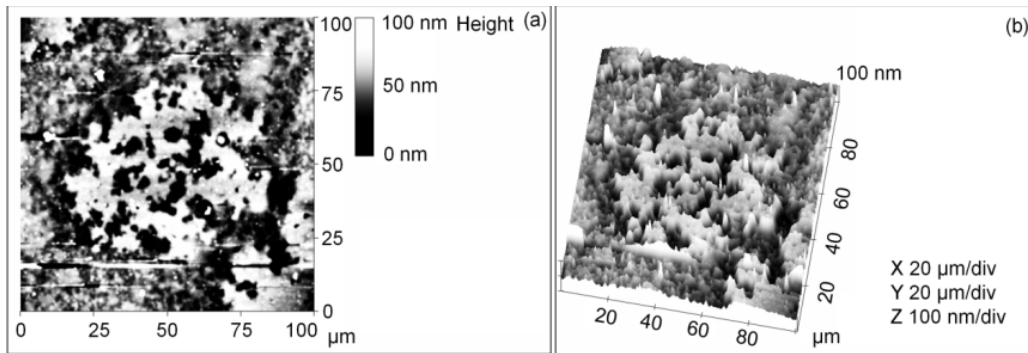
Figure 4-6: AFM image of one silicon cluster on sample A4-1 (after RCA-1 treatment). Scan size 100 μm × 100 μm with 512×512 data points. (a): top view and (b): corresponding surface plot.

4.3.4 XRD analysis

4.3.4.1   *Ex-situ* XRD scan

XRD scans were performed on sample A4-1, both before and after RCA-1 treatment. The RCA-1 treatment was found to introduce negligible changes to the XRD result. Figure 4-7 shows the XRD result obtained from the RCA-treated sample. Only one clear peak (at 28.4 °) is present in the XRD spectrum, suggesting that the c-Si grains formed are preferentially (111) oriented [11].
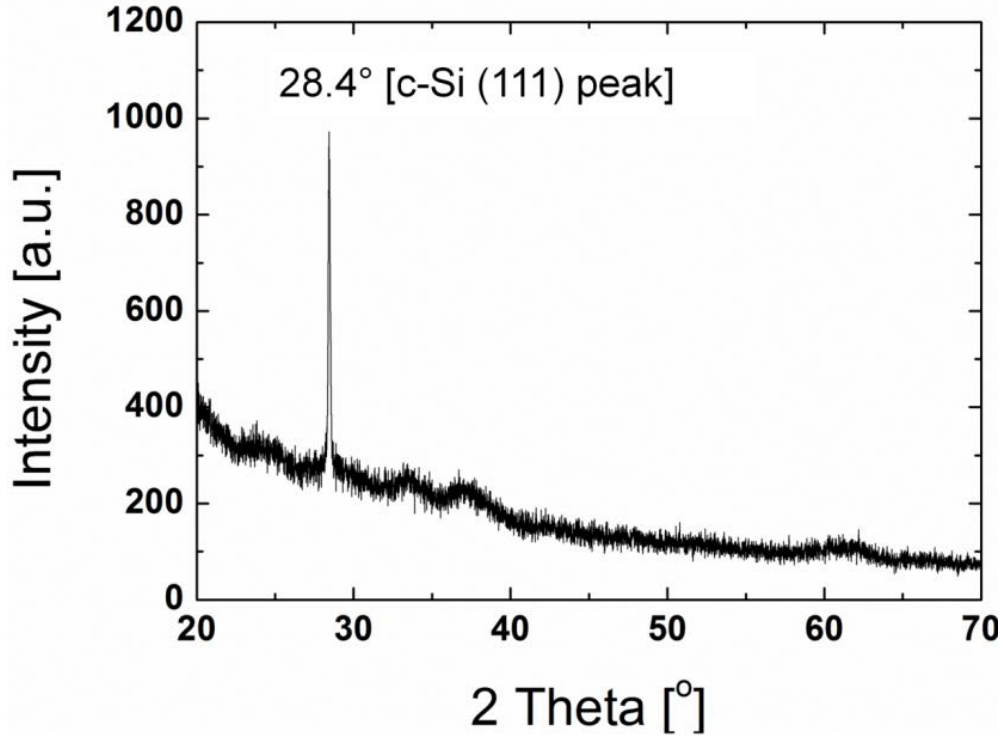
Figure 4-7: XRD scan (performed at room temperature) of AIT sample A4-1 after RCA-1 treatment.

4.3.4.2   *In-situ* XRD analysis and activation energy extraction

Crystalline Si is one of the reaction products in the solid state reaction between aluminium (Al) and glass. We studied the c-Si growth by *in-situ* XRD and used the results to extract the activation energy for the Al-glass reaction. The fraction of c-Si material is determined by using the saturated integrated XRD (111) peak area for each anneal temperature as normalizing reference. The fraction of c-Si material determined by this method was plotted versus annealing time, see Figure 4-8.
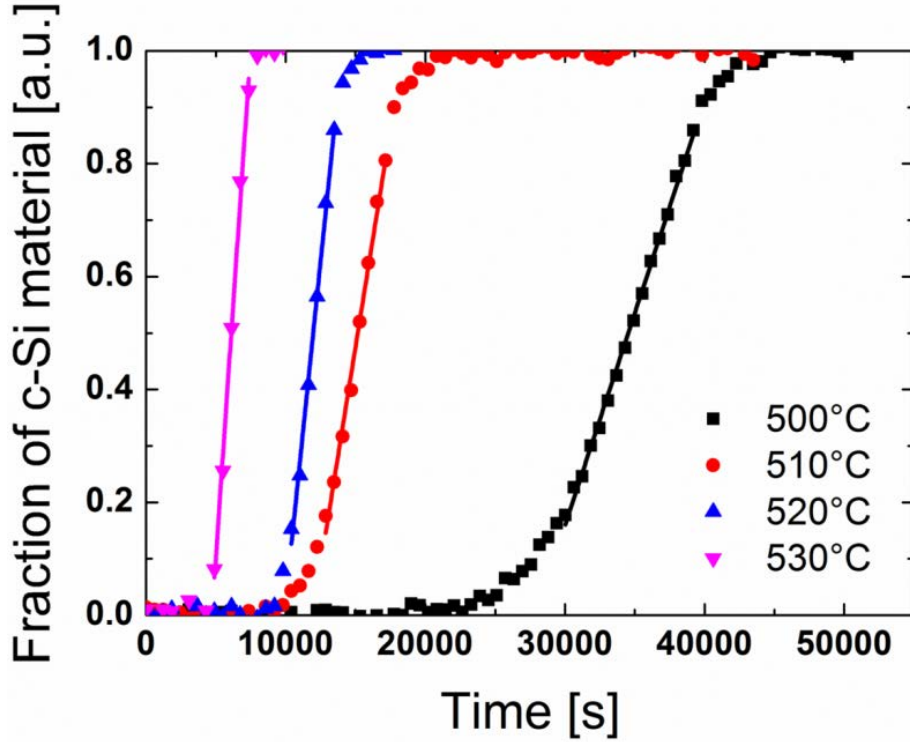
Figure 4-8: Fraction of c-Si material vs. annealing time at temperature 500 °C (sample B1), 510 °C (B2), 520 °C (B3) and 530 °C (B4).

The thermally activated process between Al and SiO_2 exhibits an Arrhenius-type behaviour in the temperature range 200-850 °C [2-6, 12]. The activation energy can be calculated using the Arrhenius equation

$$\text{Reaction rate} = A\exp(-E_a/kT) \qquad (4.1)$$

where A is an arbitrary constant, k the Boltzmann constant, T the absolute temperature, and E_a the activation energy. The slopes of the linear regions of Figure 4-8 are used as the reaction rates. The natural logarithm of the reaction rates at four different temperatures are plotted against $1/kT$ (with unit of eV^{-1}) in Figure 4-9. The slope is the activation energy, which is 3.0 ± 0.2 eV. The activation energy measured in our study is generally slightly higher than the

previously reported values [2-6, 12] (the values were listed in Section 4.1). The presence of other chemical components (such as B_2O_3, Na_2O, etc.) besides SiO_2 inside borosilicate glass could attribute to the slightly higher E_a of the reaction between Al and glass. The high activation energy of 3.0 ± 0.2 eV indicates that, to have a reasonably short process time (less than 3 hours), the AIT annealing process should be carried out at a temperature above 520 °C.
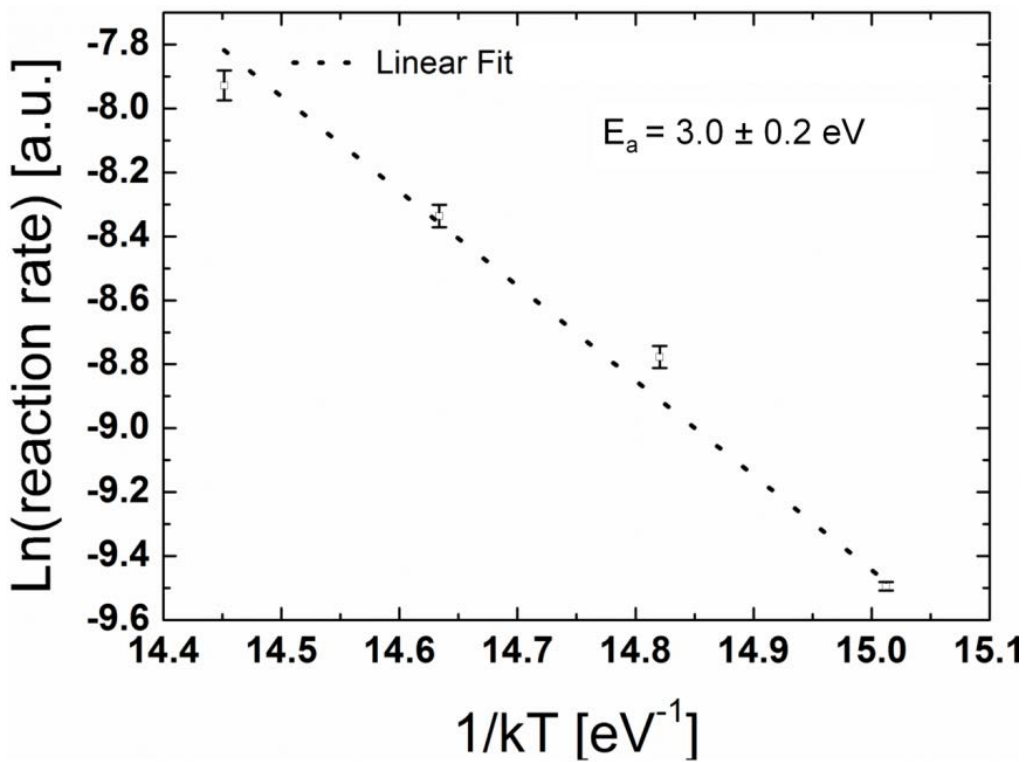
Figure 4-9: Arrhenius plot of the AIT process based on the c-Si growth from four different temperatures (sample B1 500 °C, B2 510 °C, B3 520 °C and B4 530 °C). The activation energy (E_a) was calculated from the slope of the linear fit. The linear fit was obtained by weighting every data point in proportion to its standard error.

4.3.5 Model of AIT process

A phenomenological model of the AIT process is proposed and illustrated in Figure 4-10. During the annealing, the solid state reaction between aluminium

and glass starts at random points at the glass-aluminium interface. The reduced silicon is dissolved into the aluminium layer whereas aluminium oxide starts to grow at the nucleation points, see Figure 4-10(b). At the second stage of the AIT process, the Al_2O_3 grows deeper into the glass in the form of crater shaped nodules and also grows into the aluminium over-layer; the reduced Si from the glass continues to dissolve into the aluminium over-layer and eventually starts to precipitate as crystalline silicon (c-Si) at the glass-Al interface, see Figure 4-10(c). Figure 4-10(d) marks the completion of the chemical reactions. All aluminium has been reacted with glass. Crystalline Si forms separated clusters on the glass surface. Al_2O_3 surrounds the c-Si clusters and also exists in the crater-shaped nodules embedded in the glass. In Figure 4-10(e), the final glass texture is obtained after $HF:HNO_3$ wet etching and a DI water rinse, removing the c-Si and Al_2O_3 reaction products. We suggest that the topology of the glass texture strongly depends on the size, depth and lateral distance of the Al_2O_3 nodules embedded in the glass. Following the reasoning in Ref. [4], we suggest that the silicon removal rate from the reaction sites (i.e., the diffusion of Si atoms through the Al_2O_3 nodules) is the rate limiting step in the AIT process.
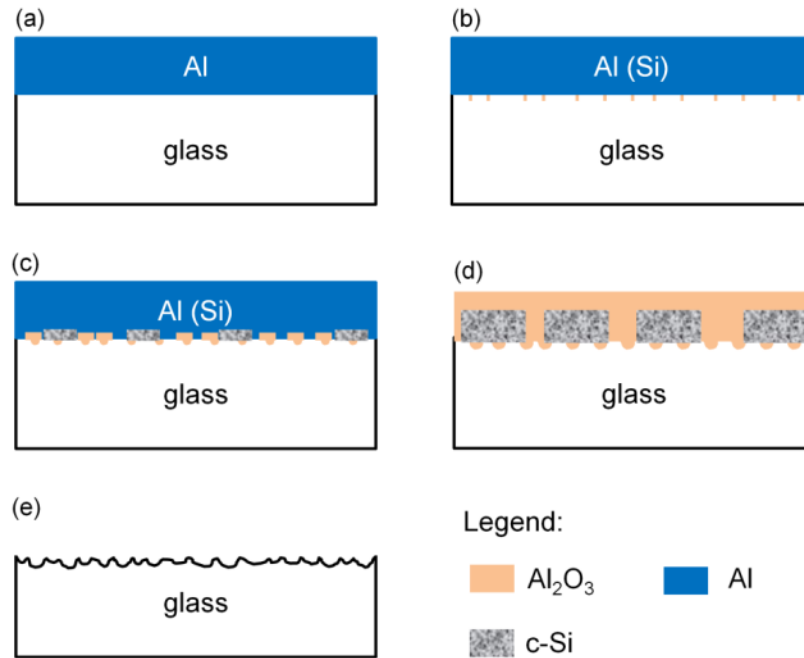
Figure 4-10: Proposed phenomenological model of the AIT process. (a) Al coated on clean and dry planar glass. (b) The solid state reaction between aluminium and glass starts at random points at the glass-aluminium interface. The reduced silicon is dissolved into the Al layer whereas aluminium oxide starts to grow at the nucleation points. (c) Si atoms inside the Al start to precipitate at the glass surface. Al_2O_3 grows deeper into the glass and crater-shaped nodules start to form. Al_2O_3 also grows into the Al over-layer. (d) Reaction completed, with c-Si clusters formed at the glass surface. Al_2O_3 surrounds the c-Si clusters (SEM cross-sectional view of the AIT annealed sample before the SC1 etching shows that there is Al_2O_3 surrounding the c-Si cluster, The SEM image is not shown in the thesis) and also exists as crater-shaped nodules. (e) HF:HNO_3 wet etch followed by a DI water rinse removes the c-Si and the Al_2O_3 and thereby textures the glass surface. The surface topology is highly dependent on the size, depth and lateral distance of the Al_2O_3 nodules.

4.4 Conclusions

In this chapter, we studied the solid state reaction between aluminium and borosilicate glass at an annealing temperature of about 500 °C. We demonstrated that c-Si clusters are formed on the glass surface and that the c-Si clusters are surrounded by Al_2O_3. We also demonstrated that crater shaped nodules, consisting of Al_2O_3, are embedded into the glass, with a width of < 5 µm and depth of < 1 µm. The activation energy of the reaction between sputtered Al

and borosilicate glass was found to be 3.0 ± 0.2 eV based on *in-situ* XRD analysis of the c-Si growth. We suggest that by adjusting the Al deposition thickness and/or annealing temperature, the Al_2O_3 nodules' size, depth and lateral separation can be controlled. As a result, the AIT glass texturing method can be further optimized for applications in thin-film solar cells.

References (Chapter 4)

[1] K. Prabriputaloong and M. R. Piggott, "Reaction between silica and aluminum," Journal of the Electrochemical Society, vol. 121, pp. 430-434, 1974.

[2] J. R. Black, "The reaction of Al with vitreous silica," in Reliability Physics Symposium, 1977. 15th Annual, 1977, pp. 257-261.

[3] R. B. Godfrey and M. A. Green, "High-temperature lifetesting of Al/SiOx/p-Si contacts for MIS solar cells," Applied Physics Letters, vol. 34, pp. 860-861, 1979.

[4] R. Forbes and S. Zukotynski, "High-temperature dielectric breakdown of silicon dioxide films with aluminum electrodes," Journal of the Electrochemical Society, vol. 136, pp. 736-739, 1989.

[5] R. Brendel and R. Hezel, "Infrared observation of thermally activated oxide reduction within Al/SiOx/Si tunnel diodes," Journal of Applied Physics, vol. 71, pp. 4377-4381, 1992.

[6] F. Dadabhai, F. Gaspari, S. Zukotynski, C. Bland, "Reduction of silicon dioxide by aluminum in metal-oxide-semiconductor structures," Journal of Applied Physics, vol. 80, pp. 6505-6509, 1996.

[7] Y. Huang, F. Law, P.I. Widenborg, A.G. Aberle, "Crystalline silicon growth in the aluminium-induced glass texturing process," Journal of Crystal Growth, vol. 361, pp. 121-128, 2012.

[8] W. M. Haynes, "Thermal Conductivity of Glasses", in CRC Handbook of Chemistry and Physics, 92nd edition (international edition 2012) ed. Boca Raton, FL.: CRC Press/Taylor and Francis, 2012.

[9] S.-J. Hwang, J.-H. Lee, C.-O. Jeong, Y.-C. Joo, "Effect of film thickness and annealing temperature on hillock distributions in pure Al films," Scripta Materialia, vol. 56, pp. 17-20, 2007.

[10] J.H. Parker, D.W. Feldman, M. Ashkin, "Raman scattering by silicon and germanium," Physical Review, vol. 155, pp. 712-714, 1967.

[11] R. Kishore, C. Hotz, H.A. Naseem, W.D. Brown, "In situ X-ray diffraction studies of aluminium-induced crystallization of hydrogenated amorphous silicon," Journal of Applied Crystallography, vol. 36, pp. 1236-1239, 2003.

[12] R. Forbes and S. Zukotynski, "Electric-field assisted solid-state reaction of aluminum and silicon dioxide," Journal of the Electrochemical Society, vol. 136, pp. 2651-2653, 1989.

Chapter 5   Optical simulations for poly-Si thin-film solar cells on AIT glass using ASA

5.1   Introduction

In this chapter, the haze and angular intensity distribution (AID) of AIT glass surfaces are calculated by a phase model based on the scalar scattering theory using AFM measured surface height profiles. The calculated haze and AID are compared with the measured ones to validate the phase model (Section 5.2). The haze and AID of textured surfaces calculated by the phase model are entered into ASA to perform optical simulations. Parasitic glass absorption and c-Si absorption in poly-Si thin-film solar cells on AIT glass can be estimated separately using the ASA optical simulations (Section 5.3).

5.2 Haze and AID simulations for AIT glass using a phase model based on the scalar scattering theory

Dominé *et al.* developed a phase model based on the Rayleigh-Sommerfeld diffraction integral. They showed that the phase model can estimate the haze and AID of both micro- and nanotextured TCO surfaces [1]. Jäger *et al.* furthermore showed that the phase model can satisfactorily predict the scattering parameters of rough interfaces between TCO and arbitrary materials, for both transmission and reflection haze and AID measurements [2]. In this section, a similar phase model reproduced in SERIS [3] is used to estimate haze and AID of textured surfaces of poly-Si thin-film solar cells on AIT glass.

Three AIT Borofloat glass samples BF1, BF7, and BF11 (as described in Section 3.2.3 of Chapter 3) were used in this work. Samples BF1, BF7, and BF11 were heavily, moderately, and lightly textured, respectively. Their haze values were measured with an UV/Vis/NIR spectrophotometre (PerkinElmer, Lambda 950), which has a 150 mm diameter integrating sphere. Their AID were measured with a goniophotometre (pab advanced technologies GmbH, pgII) at three wave-lengths (520, 620 and 780 nm). Tapping-mode atomic force microscopy (AFM) (Veeco, Dimension) was used to measure the height profiles of the textured surfaces of the three samples. All four AFM measurements had scan sizes of $10{\times}10$ μm^2 and $512{\times}512$ data points. The haze and AID of the textured samples BF1, BF7, and BF11 were then calculated by the phase model using the AFM height data. The calculated haze values and AID were then compared with the measured haze and AID.

The simulated haze values generally fit the measured haze values well, as shown in Figure 5-1. The root mean square (RMS) roughnesses of samples BF1, BF7, and BF11 are 393 nm, 337 nm, and 198 nm, respectively. Surfaces with lower roughness have a smaller haze. The simulated AID fits the measured AID well at a wavelength of 780 nm, as shown in Figure 5-2 for sample BF1. The simulated AID of sample BF1 at wavelengths of 520 nm and 620 nm, and the simulated AID of samples BF7 and BF11 at wavelengths of 520 nm, 620 nm, and 780 nm, also fit the measured AID well (figures are not shown here). Generally, the phase model satisfactorily estimates the haze and the AID of AIT glass surfaces.
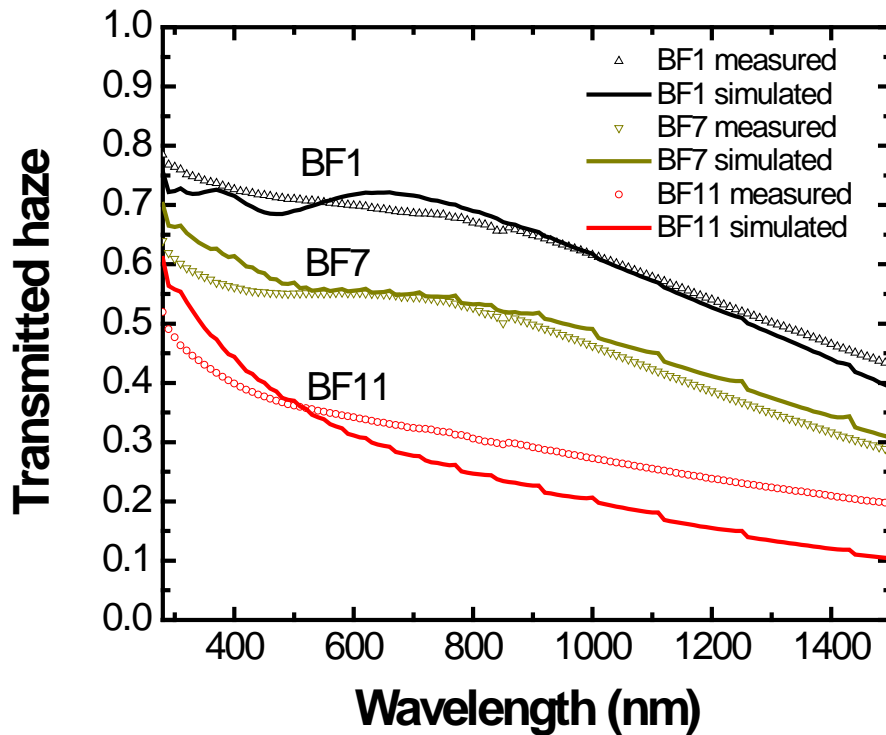
Figure 5-1: Calculated haze by the phase model vs. measured transmitted haze for samples BF1, BF7, and BF11.
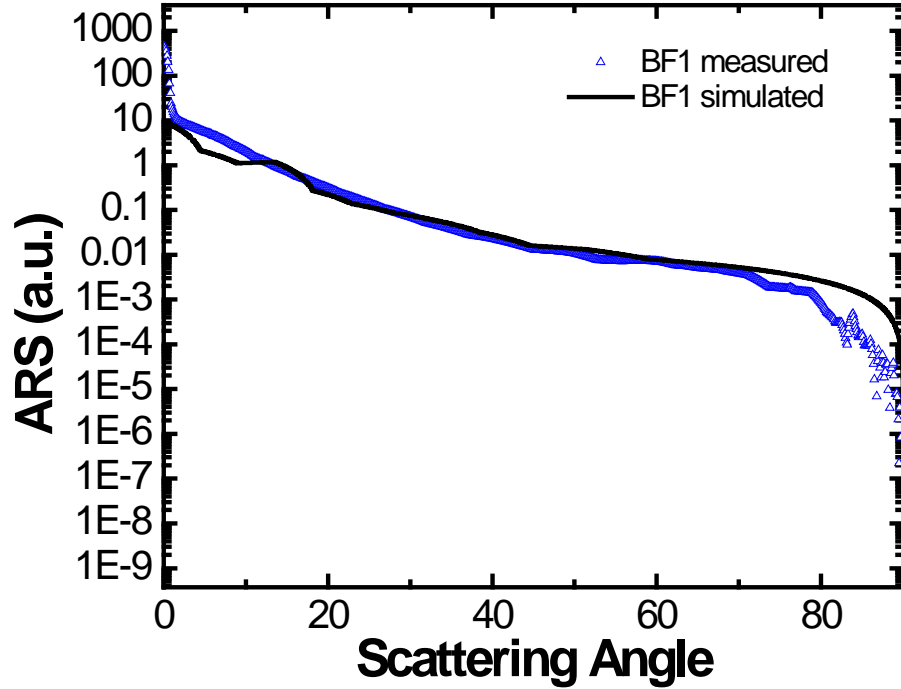
Figure 5-2: Calculated AID, or Angular Resolved Scattering (ARS), by the phase model vs. measured AID at wavelength 780 nm for AIT glass sample BF1.

5.3 ASA optical simulations for poly-Si thin-film solar cells on AIT glass

5.3.1 Introduction

In Ref. [4], Campbell *et al.* developed a ray tracing routine that incorporates random scattering to estimate the total (c-Si and glass) absorption for poly-Si thin-film solar cells on glass. However, the ray tracing routine does not separately calculate the absorption of c-Si and glass. Moreover, the ray tracing routine in Ref. [4] is used to calculate the Lambertian absorptance. In this Section, an optical simulation combining the scalar scattering theory and the commercial

thin-film solar cell simulator ASA is presented. The optical simulation can separately estimate glass and c-Si absorption.

5.3.2 Experimental details

A commercial Borofloat glass sheet (30 cm $\times$ 40 cm) from Schott AG, Germany, was AIT textured and named AIT1. The detailed AIT process is described in Ref. [5]. Glass sample AIT1 was then cleaned in a dish washer (Miele, G7883CD). The transmittances (T) and reflectances (R) of the bare glass sample AIT1 were measured in superstrate configuration using a UV/Vis/NIR spectrophotometer (PerkinElmer, Lambda 1050), which has a 150 mm diameter integrating sphere. The absorptance (A) of the bare glass sample AIT1 was calculated via $A = 1 - R - T$. Using PECVD, the glass sheet AIT1 was then coated with ~ 70 nm of silicon nitride (SiN_x) and a ~1600 nm thick a-Si:H $n^+/p^-/p^+$ diode. The details of the a-Si:H diode PECVD deposition process can be found in Ref. [6]. The a-Si:H thin-film diode then underwent solid phase crystallization (SPC) in a nitrogen purged oven at 600 °C for 12 hours. The device structure of a poly-Si solar cell on AIT glass after the SPC process is illustrated in Figure 5-3 (a). Two 3 cm $\times$ 3 cm poly-Si thin-film solar cells on glass after the SPC process were cut from the centre of the 30 cm $\times$ 40 cm poly-Si on glass sample AIT1. The two textured glass substrates of the two 3 cm $\times$ 3 cm poly-Si thin-film solar cells on glass were named AIT1a and AIT1b. Total (glass + c-Si) absorptance of the poly-Si solar cell on glass sheet AIT1a was measured using the UV/Vis/NIR spectrophotometre via $A = 1 - R - T$. The height profile of the rear Si surface (as indicated in Figure 5-3 (a)) of the poly-Si thin-film solar cell on glass sheet AIT1a was measured by tapping-mode atomic force microscopy (AFM) (Veeco, Dimension). The AFM

measurements had a scan size of 20×20 µm^2 and 512×512 data points. The two 3 cm × 3 cm poly-Si thin-film solar cells on glass sheets AIT1a and AIT1b were then plasma etched by using SF$_6$ gas to fully remove the poly-Si layer and the SiN$_x$ layer, as sketched in Figure 5-3 (b). The plasma etching was done in a 13.56 MHz parallel-plate RF powered plasma etcher (Oxford Plasma 80 RIE system). The absorptances of glass sheets AIT1a and AIT1b after the plasma etching were measured using the UV/Vis/NIR photospectrometre via $A = 1 - R - T$. The height profile of the AIT textured surface (as indicated in Figure 5-3 (b)) of glass sheet AIT1a was measured by the tapping-mode AFM. The AFM measurement had a scan size of 20×20 µm^2 and 512×512 data points.
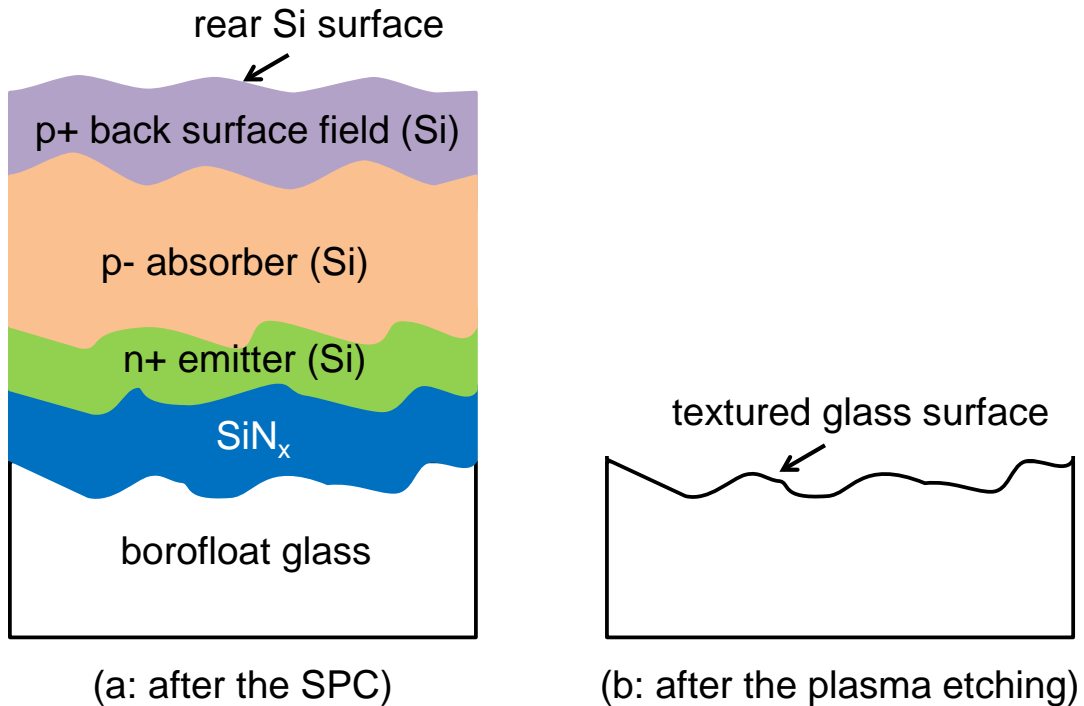
Figure 5-3: Illustration of (a) a poly-Si thin-film solar cell on AIT textured Borofloat glass after the SPC process, and (b) exposed AIT textured glass with poly-Si and SiN$_x$ layers removed by plasma etching.

The real part of the refractive index (n) of Borofloat glass sheets was determined by fitting measured dispersion data with a three-term Sellmeier equation. The effective imaginary part (κ) of the refractive index of glass sheet AIT1a was calculated based on the measured transmittance and the scalar scattering theory. Haze and angular intensity distribution (AID) of the rear Si surface and the textured glass surface were calculated from the AFM measured heights using the phase model based on the scalar scattering theory proposed in Refs. [1, 2]. The calculated n, κ values of textured glass, calculated haze and AID of the textured glass surface and the rear Si surface by the phase model were then loaded into the ASA simulator [7, 8] for optical simulations. In the ASA optical simulations, absorptance in the SiN_x layer is not considered. The sum of the simulated absorptance of c-Si and glass was then compared to the measured absorptance of the poly-Si thin-film solar cell on glass sheet AIT1a to check the validity of the optical simulation method. The impact of the glass thickness on the current densities of c-Si cells and the current loss due to parasitic glass absorption was also evaluated using the ASA optical simulations.

5.3.3 Results and discussion

5.3.3.1　　Absorptance of bare AIT glass and AIT glass after the SPC process

Figure 5-4 shows the measured absorptance of bare textured glass sample AIT1 and glass samples AIT1a & b after the SPC process. To measure the absorption of textured glass sheets AIT1a and AIT1b, the poly-Si and SiN_x layers on glass sheets AIT1a and AIT1b were fully removed by plasma etching. The measure-

ments covered the wavelength range from 250 nm to 1500 nm. The absorption band at around 1400 nm wavelength corresponds to the first overtone of the stretching vibration of water molecules that are hydrogen-bonded to neighbouring silanol groups inside the silica type glass [9-11]. There is a shift of the absorption edge in the UV region and a slightly higher absorption in the near-infrared region above 800 nm wavelength for textured glass samples AIT1a & b, compared to the bare textured glass sample AIT1. The shift of the absorption edge could be related to the moderate temperatures [12, 13] during the PECVD and SPC processes.
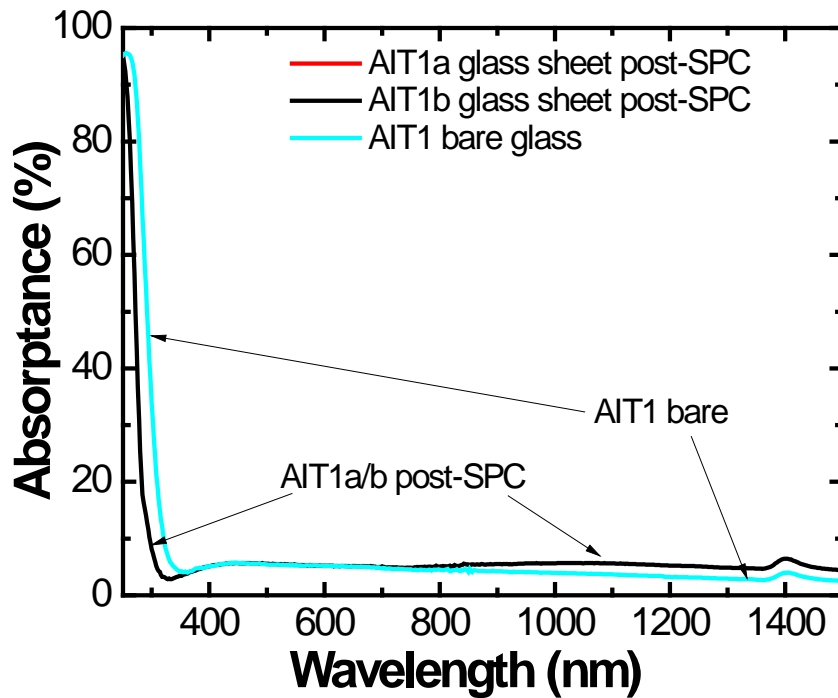
Figure 5-4: Absorptance of bare AIT textured glass sheet AIT1 and two AIT textured glass sheets AIT1a and AIT1b after the SPC process.

5.3.3.2   Calculation of real part of the refractive index (*n*) for AIT textured Borofloat glass

In this work, it is assumed that the real parts of the refractive indices of bare planar Borofloat glass, bare AIT textured Borofloat glass, and AIT textured Borofloat glass after the SPC process are the same. Six sets of measured dispersion data (*n* versus wavelength λ) of the Borofloat glass were retrieved from the website of the Borofloat glass manufacturer [14]. *n* values for other wavelengths were calculated by fitting the retrieved dispersion data with a three-term Sellmeier equation, following a similar procedure as described in Refs. [15, 16]. The three-term Sellmeier equation [19] for the Borofloat glass is found to be

$$n(\lambda) = 1 + \frac{0.001736\lambda^2}{\lambda^2 + 0.000362} + \frac{0.122760\lambda^2}{\lambda^2 - 0.034671} + \frac{1.011537\lambda^2}{\lambda^2 - 0.005044} \tag{5.1}$$

where λ is the wavelength. The retrieved dispersion data and the calculated *n* values based on the three-term Sellmeier equation are shown in Figure 5-5. The wavelength range is from 250 nm to 1500 nm. The retrieved dispersion data are well fitted with the three-term Sellmeier equation.
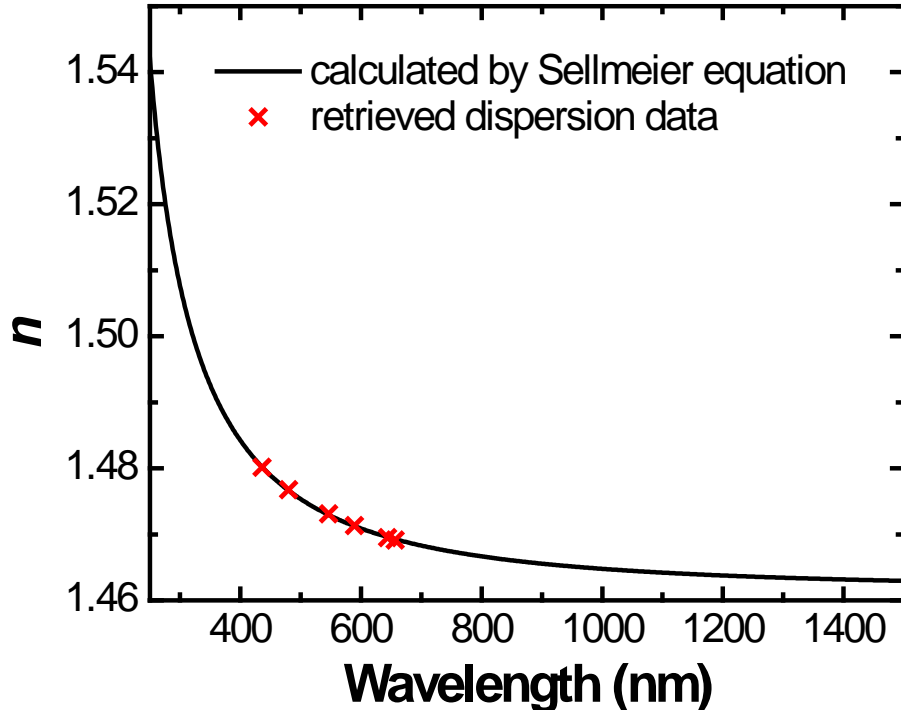
Figure 5-5: Calculation of n values for Borofloat glass by fitting the measured dispersion data with a three-term Sellmeier equation.

5.3.3.3 Calculation of effective imaginary part of refractive index (κ) for AIT textured Borofloat glass

Figure 5-6 illustrates a simplified optical energy flow system inside a glass sheet with one surface textured to obtain multiple internal reflections. *r* is the Fresnel reflectivity of the glass-air interface. It is given by [20]

$$r = \frac{(n-1)^2}{(n+1)^2} \tag{5.2}$$

where *n* is the real part of the refractive index for glass, as calculated in Section 5.3.3.2. Noted that equation 5.2 is a simplified expression of *r*, which is applicable for wavelengths where the imaginary part of the refractive index is several orders smaller than its real part. This simplified expression is valid for

92

silica-type glass in the wavelength range investigated in this work (250 - 1500 nm), according to Ref. [17].

In Figure 5-6, I_0 refers to the intensity of the incident light. d is the physical thickness of the AIT glass sheet, and α represents the effective absorption coefficient. For α, optical pathlength enhancement inside the glass due to glass texturing was taken into consideration. The optical thickness of the AIT glass sheet is termed $d_{optical}$, the optical pathlength enhancement factor [21] inside the glass due to texturing is termed B_{glass}, and the physical absorption coefficient determined by the intrinsic glass material properties is termed as $\alpha_{intrinsic}$. α of the AIT glass sheet is then related to $\alpha_{intrinsic}$ by

$$\alpha d = \alpha_{intrinsic} d_{optical} = \alpha_{intrinsic} B_{glass} d \qquad (5.3)$$

So:

$$\alpha = \alpha_{intrinsic} B_{glass} \qquad (5.4)$$
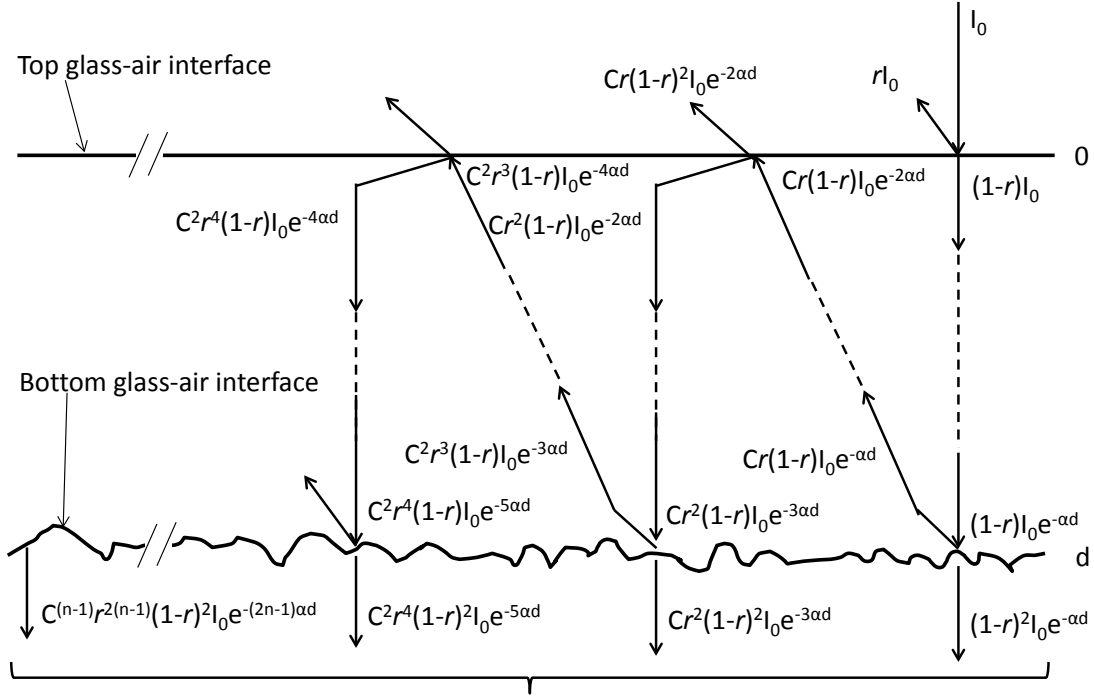
Figure 5-6: Energy flow inside a glass sheet with one textured surface.

For the optical system shown in Figure 5-6, a parameter *C* is introduced and defined by

$$C = \frac{\int_0^{\theta_C} AID_R(\theta)d\theta}{\int_0^{\pi/2} AID_R(\theta)d\theta} \tag{5.5}$$

where θ_C is the critical angle of total internal reflection (TIR) at the top glass-air interface in Figure 5-6. $AID_R(\theta)$ is the angular intensity distribution [22] in reflection at the bottom glass-air interface in Figure 5-6. $AID_R(\theta)$ was calculated with AFM measured heights of the textured side of glass sheet AIT1a, using the phase model based on the scalar scattering theory [1, 2]. The parameter *C* can take any value between 0 (complete TIR case) and 1 (planar case). In the

simplified optical system shown in Figure 5-6, it is assumed that light with a reflection angle larger than θ_C at the bottom glass-air interface is totally internally reflected inside the glass for multiple times until it is fully absorbed by the glass. In other words, these photons do not contribute to transmission. The transmission was then calculated by [20]

$$T = \frac{I_0(1-r)^2 e^{-\alpha d}(1+Cr^2 e^{-2\alpha d}+C^2 r^4 e^{-4\alpha d}+\cdots)}{I_0} = \frac{(1-r)^2 e^{-\alpha d}}{1-Cr^2 e^{-2\alpha d}} \qquad (5.6)$$

The transmission can be measured with a UV/Vis/NIR photospectrometre. The only unknown in equation (5.6) is the effective absorption efficient α. Hence, α can be calculated by solving the quadratic equation (5.6). Once α is calculated, the effective extinction coefficient (κ) can be calculated by [20]:

$$k = \frac{\alpha\lambda}{4\pi} \qquad (5.7)$$

where λ is the wavelength. Figure 5-7 shows the calculated κ value for the bare glass sample AIT1 (k_{bare}) and glass sample AIT1a after the SPC process ($k_{post-SPC}$). The wavelength range is from 250 nm to 1500 nm. The extinction coefficient (κ) for AIT glass sample does not significantly change due to the moderate-temperature SPC process.
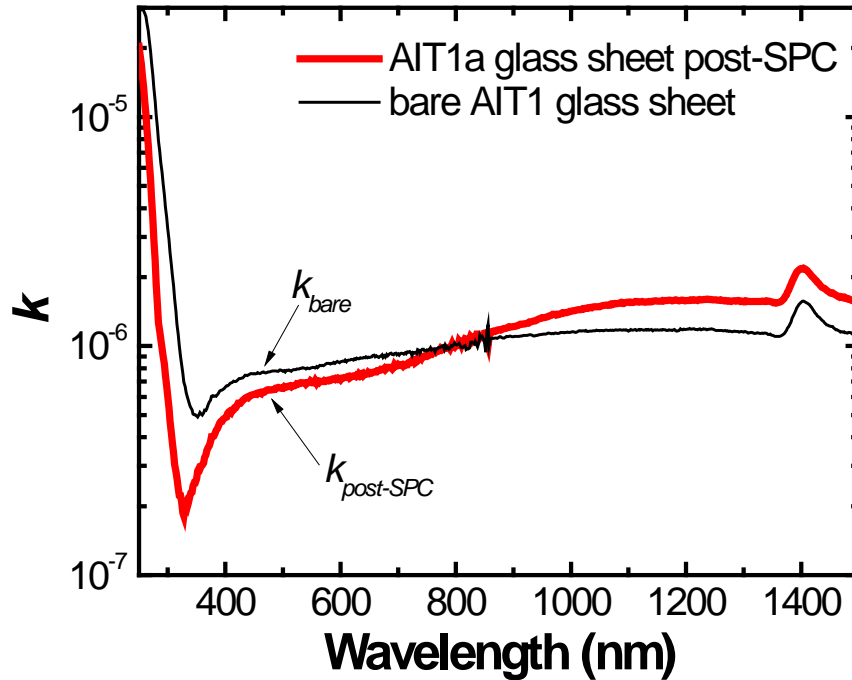
Figure 5-7: Calculated effective extinction coefficient k of bare AIT glass sample AIT1 and glass sample AIT1a after the SPC process.

5.3.3.4 Optical simulation of absorptance of poly-Si solar cells on AIT glass by ASA

Figure 5-8 shows the measured absorptance of poly-Si thin-film solar cell on glass sheet AIT1a after the SPC process, the c-Si absorptance simulated by ASA, the glass absorptance simulated by ASA, and the sum of the simulated glass and c-Si absorptance (labelled "simulated total A" in the figure). The absorptance was measured based on the $A = 1 - R - T$ method. The poly-Si thickness of sample AIT1a was about 1.6 μm. The thicknesses of c-Si and the glass sheet were set as 1.6 μm and 3.3 mm in the ASA optical simulation. To simulate the glass absorptance, the n and $\kappa_{post\text{-}SPC}$ of AIT glass after the SPC process calculated in Sections 5.3.3.2 and 5.3.3.3 were used in ASA.

96

For wavelengths up to 1000 nm, the simulated total absorptance (A) in Figure 5-8, which is calculated by summing the simulated c-Si A and the simulated glass A, generally agrees quite well with the measured absorptance of the sample. Above 1000 nm, the measured absorptance is significantly higher than the simulated absorptance. The difference is likely due to the errors in the R and T measurements, as discussed in Section 2.5.2.3 of Chapter 2. The simulated c-Si A is significantly lower than the measured total absorptance (c-Si + glass). As a result, the current density (J_{ph}) calculated from the measured absorptance of poly-Si on textured glass could significantly overestimate the current density generated by the c-Si absorber. To more accurately estimate the current density generated by the c-Si absorber, it is suggested to subtract the current loss due to glass absorptance from the current density calculated based on the measured absorptance. For example, for the sample shown in Figure 5-8, the 1-Sun current density calculated based on the measured absorptance is 29.53 mA/cm^2 for the 280 - 1100 nm wavelength range. The current loss due to glass absorption calculated based on ASA simulation in the same wavelength range is 3.55 mA/cm^2. Hence, the current density generated by the 1.6 µm thick poly-Si on AIT glass sample with air as the back surface reflector (BSR) is estimated to be 25.98 mA/cm^2.
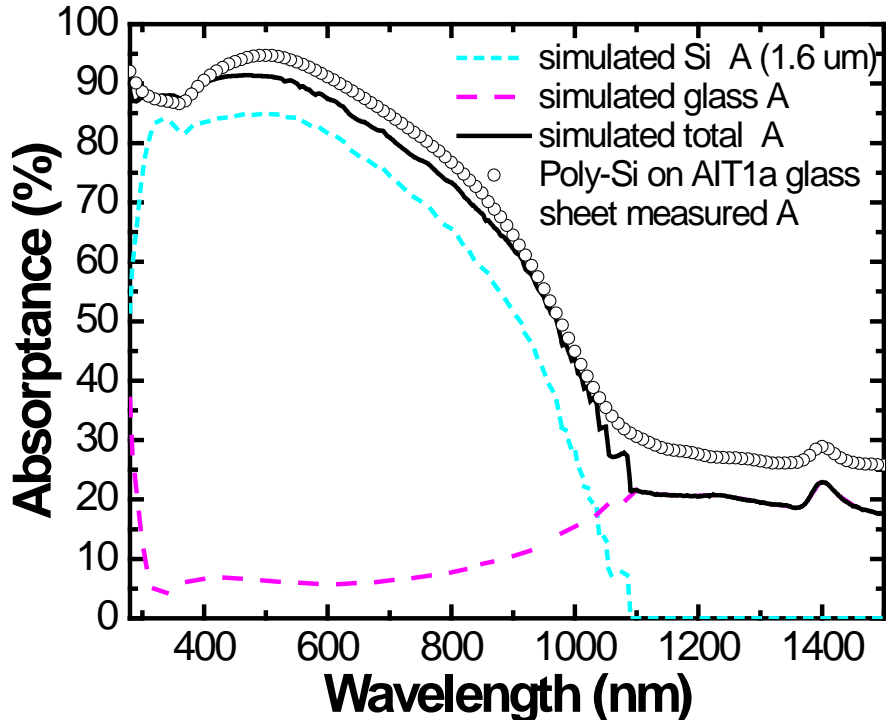
Figure 5-8: ASA simulated absorptances versus wavelength for poly-Si thin-film sample AIT1a (lines). Also shown (circles) is the measured absorptance of the sample.

5.3.3.5 Impact of glass thickness on current density generated by the c-Si absorber and current loss due to parasitic glass absorption

Figure 5-9 shows the current loss due to glass absorption and the current density generated by a 3 µm thick c-Si film on AIT glass, with a stack of silicon dioxide and aluminium as the back surface reflector (BSR). The current loss due to glass absorption and the c-Si current density were calculated by ASA for glass thicknesses from 3.3 mm to 0.3 mm, in steps of 0.3 mm. In this work, the textured glass is assumed to be optically homogeneous. The current loss due to parasitic glass absorption reduces as the glass sheet gets thinner. Correspondingly, as the glass gets thinner, more photons have the chance to re-enter

the c-Si layer from the glass side, which results in a higher current density generated by the c-Si layer. However, the relationship between the reduction of the current loss due to glass absorption by thinning the glass and the current density gain from the c-Si absorber is not one to one. By thinning the glass from 3.3 mm to 0.3 mm, the current loss due to parasitic glass absorption is reduced from 3.74 to 0.46 mA/cm^2, i.e., by 3.28 mA/cm^2. However, the current density of the c-Si layer only improves by 1.98 mA/cm^2 (i.e., by 7.3 %). In the experiments reported in Ref. [18], the J_{SC} improved by 6.3 % on average for poly-Si thin-film solar cells on AIT glass when the glass thickness was reduced from 3.3 to 0.5 mm. The highest J_{SC} enhancement demonstrated in Ref. [18] was 8% when thinning the glass from 3.3 to 0.5 mm. The current density enhancement of 7.3 % estimated by the ASA optical simulations of the present work thus agrees well with the experimental results of Ref. 18. This shows that the optical simulation method presented in this thesis is able to satisfactorily estimate the light trapping performance of poly-Si thin-film solar cells on textured glass.
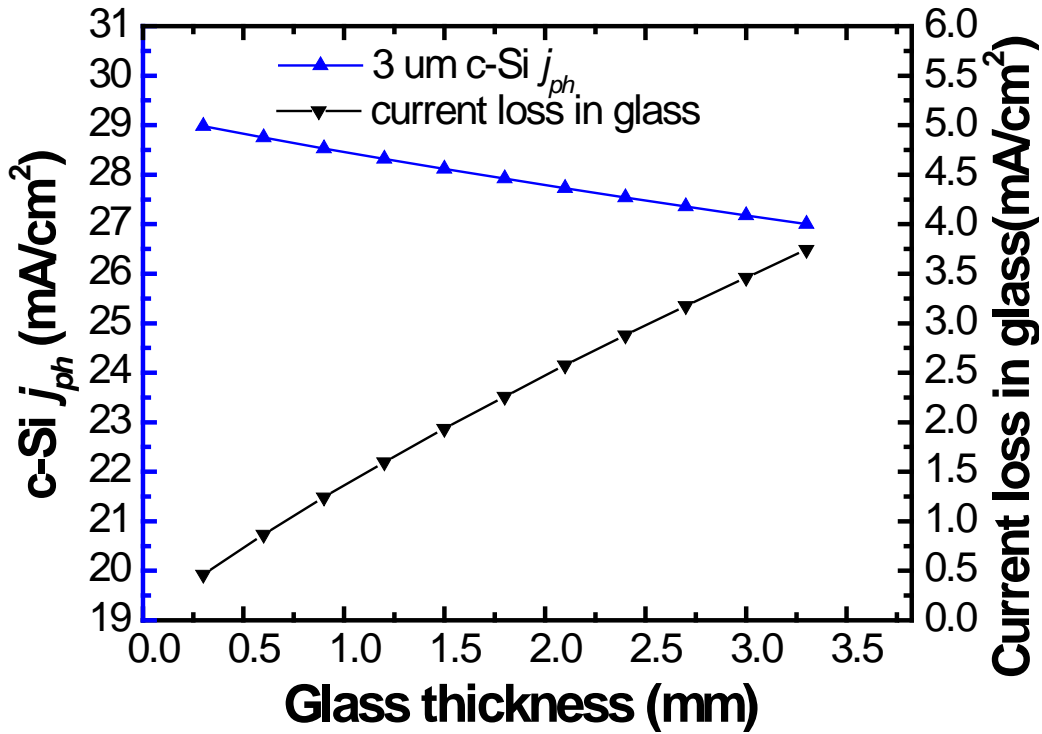
Figure 5-9: Calculated impact of the glass thickness on the current density of the c-Si absorber and the current loss due to parasitic glass absorption. The simulations assumed a fixed c-Si film thickness of 3 μm and a stack of silicon dioxide and aluminium as the back surface reflector.

5.4 Summary

In this chapter, a phase model based on the scalar scattering theory was demonstrated to be able to accurately estimate the haze and AID of rough surfaces in poly-Si thin-film solar cells on textured glass superstrates. The real and imaginary parts of the refractive index of Borofloat glass with one textured surface were calculated. By combining the scalar scattering theory with the ASA thin-film solar cell simulator, the parasitic glass absorption and the c-Si absorption for poly-Si thin-film solar cells on textured glass can be separately estimated. The one-Sun current density was estimated to be enhanced by 7.3 %

if the glass is thinned from 3.3 to 0.3 mm, assuming a 3 µm thick c-Si film on AIT glass and a stack of silicon dioxide and aluminium as the back surface reflector. Using the optical simulation method proposed in this chapter, the light trapping performance of poly-Si thin-film solar cells on textured glass can be evaluated more accurately.

References (Chapter 5)

[1] D. Domine, F.-J. Haug, C. Battaglia, C. Ballif, Modeling of light scattering from micro- and nanotextured surfaces, Journal of Applied Physics 107 (2010) 044504.

[2] K. Jäger, M. Fischer, R.A.C.M.M. Van Swaaij, M. Zeman, A scattering model for nano-textured interfaces and its application in opto-electrical simulations of thin-film silicon solar cells, Journal of Applied Physics 111 (2012) 083108.

[3] N. Sahraei, K. Forberich, S. Venkataraj, A.G. Aberle, M. Peters, Analytical solution for haze values of aluminium-induced texture (AIT) glass superstrates for a-Si:H solar cells, Optics Express, 22 (2014) A53-A67.

[4] P. Campbell, P.I. Widenborg, A.B. Sproul, A.G. Aberle, Surface textures for large-grained poly-silicon thin-film solar cells on glass using the AIT method, Tech. Digest 15th International Photovoltaic Science and Engineering Conference (PVSEC-15), Shanghai, China, 2005, pp. 859-860.

[5] Y. Huang, P.I. Widenborg, A.G. Aberle, Up-scaling of the AIT glass texturing method to pilot line-scale borosilicate glass sheets, Proc. 26th European Photovoltaic Solar Energy Conference (EU PVSEC), Hamburg, 2011, pp. 2750 - 2753.

[6] H. Hidayat, A. Kumar, F. Law, C. Ke, P.I. Widenborg, A.G. Aberle, Impact of rapid thermal annealing temperature on non-metallised polycrystalline silicon thin-film diodes on glass, Thin Solid Films, 534 (2013) 629-635.

[7] M. Burgelman, J. Verschraegen, S. Degrave, P. Nollet, Modeling thin-film PV devices, Progress in Photovoltaics: Research and Applications, 12 (2004) 143-153.

[8] M. Zeman, J. Krc, Optical and electrical modeling of thin-film silicon solar cells, Journal of Materials Research, 23 (2008) 889-898.

[9] D.L. Wood, E.M. Rabinovich, D.W. Johnson, J.B. MacChesney, E.M. Vogel, Preparation of high-silica glasses from colloidal gels: III, Infrared spectrophotometric studies, Journal of the American Ceramic Society, 66 (1983) 693-699.

[10] F. Orgaz, H. Rawson, Characterization of various stages of the sol-gel process, Journal of Non-Crystalline Solids, 82 (1986) 57-68.

[11] M.A. Villegas, J.M. Fernandez Navarro, Characterization and study of Na2O-B2O3-SiO2 glasses prepared by the sol-gel method, Journal of Materials Science, 23 (1988) 2142-2152.

[12] N. Shimodaira, K. Saito, A.J. Ikushima, T. Kamihori, S. Yoshizawa, VUV transmittance of fused silica glass influenced by thermal disorder, in: Proceedings of SPIE 4000, pp. 1553-1559 (2000).

[13] B. Wedding, Measurements of high-temperature absorption coefficients of glasses, Journal of the American Ceramic Society, 58 (1975) 102-105.

[14] Optical properties of Borofloat33 glass, http://www.us.schott.com/borofloat/english/attribute/optical/index.html (accessed on 20 Mar 2014).

[15] I.H. Malitson, Interspecimen comparison of the refractive index of fused silica, Journal of the Optical Society of America, 55 (1965) 1205-1208.

[16] C.Z. Tan, Determination of refractive index of silica glass for infrared wavelengths by IR spectroscopy, Journal of Non-Crystalline Solids, 223 (1998) 158-163.

[17] R. Kitamura, L. Pilon, M. Jonasz, Optical constants of silica glass from extreme ultraviolet to far infrared at near room temperature, Applied Optics, 46 (2007) 8118-8133.

[18] C. Hongtao, Light management for polycrystalline Si thin-film solar cells on glass superstrates, PhD thesis, University of New South Wales, Australia, 2012.

[19] G. Ghosh, Sellmeier coefficients and dispersion of thermo-optic coefficients for some optical glasses, Applied Optics, 36 (1997) 1540-1546.

[20] F. Jenkins, H. White, Fundamentals of Optics, 4th ed., McGraw-Hill Science/Engineering/Math, 2001 Dec.

[21] D. Inns, ALICIA polycrystalline silicon thin-film solar cells, PhD thesis, UNSW, 2007.

[22] S. Schröder, T. Herffurth, H. Blaschke, A. Duparré, Angle-resolved scattering: An effective method for characterizing thin-film coatings, Applied Optics, 50 (2011) C164-C171.

Chapter 6   Enhanced light trapping in polycrystalline silicon thin-film solar cells using plasma-etched submicron textures

6.1   Introduction

Texturing the rear Si surface by KOH wet-etching for e-beam evaporated SPC poly-Si solar cells on planar glass sheets (as described in Section 2.3.2.1 of Chapter 2) is an effective light trapping method [1]. The wet-etching method produces micron-size features and a cell with a short-circuit current density of 26.6 mA/cm^2 has been reported for an absorber layer thickness of 3.6 µm [1]. However, for this device about 2 µm of poly-Si material had to be removed by wet etching, which significantly increases the material consumption. Si surface texturing of multicrystalline Si wafer solar cells by dry plasma etching (Section 2.3.2.2, Chapter 2) was studied by several research groups [2-6]. The authors of Refs. [2-6] demonstrated that dry plasma etching is a feasible method to achieve higher PV efficiency for multicrystalline Si wafer solar cells, by improving J_{SC} and without deteriorating V_{OC} and *FF*.

In this chapter we demonstrate that dry plasma etching using a mix of sulphur hexafluoride (SF$_6$) and dioxygen (O$_2$) can also be used to produce a texture on

the rear Si surface of PECVD SPC poly-Si thin-film solar cells on glass. The resulting rear Si texture (RST) shows reflection haze values of more than 95% at the Si-air interface. Poly-Si consumed by plasma etching is estimated to be around 500 nm for the texture. The average feature size of the texture is around 200 nm. We use a phase model based on the scalar scattering theory to calculate the scattering properties of the textured surface. We also use the thin-film solar cell simulator ASA to evaluate the light trapping and current enhancement induced by the texture. Combining this submicron RST with a micrometre-scale glass texture can produce a multi-scale rear Si surface texture. Assuming a 1900 nm thick poly-Si solar cell on glass with a high-quality back surface reflector (silicon dioxide/silver stack), the calculated photon density absorbed in the poly-Si solar cell with the multi-scale rear Si surface texture corresponds to a 1-Sun short-circuit current density (J_{SC}) of 28.6 mA/cm^2, which is 1.4 mA/cm^2 more than the calculated J_{SC} of a poly-Si solar cell with the same thickness on textured glass but without RST. The calculated current densities have taken parasitic glass absorption into consideration. The main results of the work described in this Chapter have been published in Ref. [7].

6.2 Materials and methods

The commercially available borosilicate glass sheets (30 cm × 40 cm, planar) were cleaned in a dish washer (Miele, G7883CD). Using PECVD, the glass sheets were then coated with about 70 nm of silicon nitride (SiN$_x$) and an ~2400 nm thick a-Si:H n$^+$/p$^-$/p$^+$ diode. The details of the a-Si:H diode PECVD deposition

process can be found in Ref. [8]. The a-Si:H thin-film diode then underwent solid phase crystallization in a nitrogen purged oven at 600°C for 12 hours, followed by 1 minute of rapid thermal processing (RTP) at 1050°C [8] and then hydrogen passivation in a microwave powered plasma [9]. Four 2.5×2.5 cm^2 samples (labelled RST1, RST2, RST3 and RST4) were then cut from the centre of the planar poly-Si sample. The device structure of the planar poly-Si sample is named "planar" and shown in Figure 6-1(a). The reflectances (R) of these four planar samples were measured with an UV/Vis/NIR spectrophotometer (PerkinElmer, Lambda 950), which has a 150 mm diameter integrating sphere. The incident beam entered the samples from the glass side (i.e., superstrate configuration) in all the optical measurements reported in this Chapter. These samples (RST1 - RST4) were then plasma etched in a 13.56 MHz parallel-plate RF powered plasma etcher (JLS Designs Ltd, Mini-lab MPS 2200), which was preconditioned with an isopropyl alcohol clean and an O$_2$ plasma etch of the empty chamber (RF power 400 W, O$_2$ flow rate 10 sccm, chamber pressure 13.3 Pa, and etch time 5 minutes). The RF power for the four samples (RST1 - RST4) was 400, 450, 500 and 550 W, respectively, while keeping the other process parameters constant: SF$_6$ flow rate 40 sccm, O$_2$ flow rate 10 sccm, chamber pressure 26.7 Pa, and etch time 5 minutes. The device structure of these four samples (RST1 - RST4) after the plasma etching is named "RST" (rear Si texture) and is shown in Figure 6-1(c). The transmittances (T) and reflectances (R) of samples RST1 - RST4 after the plasma etching step were measured in super-strate configuration using the UV/Vis/NIR spectrophotometer. The absorptances (A) were calculated via $A = 1 - R - T$. The surface morphology of sample RST4 was then studied by scanning electron microscopy (SEM) (Zeiss, Auriga CrossBeam FIB/SEM workstation, whereby FIB stands for focused ion beam).

The thickness of the remaining poly-Si film of sample RST4 after the plasma etching was measured with the SEM. The required cross-section was created by milling a 10 μm deep trench into the poly-Si sample, using FIB gallium ions. Two other 10×10 cm^2 poly-Si thin-film n$^+$/p$^-$/p$^+$ diode samples, labelled AIT1 and Planar1, with about 1900 nm poly-Si thickness, were prepared on an AIT glass sheet and on a planar glass sheet, respectively. The details of the used AIT glass texturing process are described elsewhere [10, 11]. The poly-Si thin-film preparation steps of samples AIT1 and Planar1 were the same as for samples RST1 - RST4. The device structure of sample AIT1 after the hydrogenation process is named "AIT" and shown in Figure 6-1(b). After the hydrogenation process, the absorptances of samples Planar1 and AIT1 were calculated from the measured R and T data, using $A = 1 - R - T$. Sample AIT1 was then plasma etched using the same process parameters as for sample RST4 (RF power 550 W, SF$_6$ flow rate 40 sccm, O$_2$ flow rate 10 sccm, chamber pressure 26.7 Pa, and etch time 5 minutes). The device structure of sample AIT1 after the plasma etching is named "AIT + RST" and shown in Figure 6-1(d). The reflectance and transmittance of sample AIT1 were measured after the plasma etching step, in superstrate configuration. Tapping-mode atomic force microscopy (AFM) (Veeco, Dimension) was used to measure height profiles of the following surfaces: the AIT textured glass surface of sample AIT1 before the SiN$_x$ coating, the rear Si surface of sample RST4 after the plasma etching step, the rear Si surfaces of sample AIT1 before and after the plasma etching step. All four AFM measure-ments had scan sizes of 20×20 μm^2 and 512×512 data points. Haze and angular intensity distribution (AID) of different interfaces in the four device structures of Figure 6-1 were calculated with the measured heights based on the scalar

107

scattering theory. The calculated haze and AID were then entered into the ASA simulator [12, 13] for optical simulations. For the AIT device (sample AIT1 before plasma etching) and the AIT + RST device (sample AIT1 after plasma etching), the haze and AID of both the front and rear Si surfaces were calculated based on the scalar scattering theory and then used as input in ASA to simulate multiple scattering. Parasitic glass absorption in AIT glass (discussed in detail in Chapter 5) is considered in the ASA simulations. The simulated c-Si absorptance of device AIT is compared with the absorptance of device AIT + RST. The simulated current densities (J_{ph}) of the c-Si layers of the four devices shown in Figure 6-1 were calculated by ASA based on the absorptances.
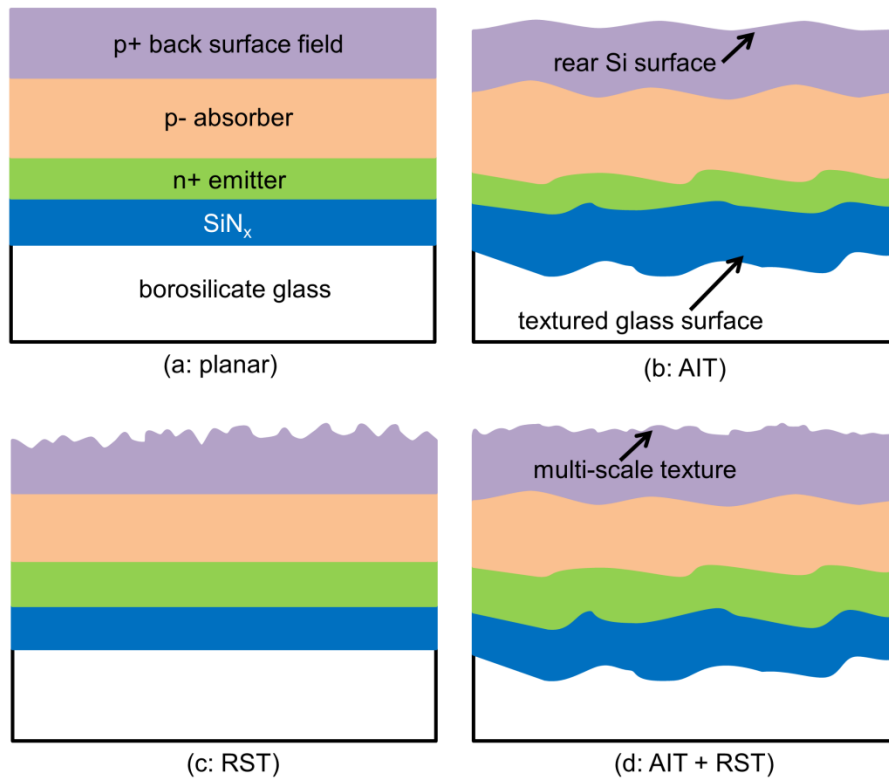
Figure 6-1: Schematic drawings of poly-Si thin-film solar cells before metallization (a): on a planar glass sheet, (b): on an aluminium-induced texture (AIT) glass sheet, (c): on a planar glass sheet with the rear Si surface textured by plasma etching, and (d): on an AIT glass sheet with the multi-scale rear Si surface texture produced by an additional plasma etching step. In the text, we name structure (a) planar, (b) AIT, (c) RST, and (d) AIT + RST. Note that the structure is presented here upside down (i.e., it is illuminated from the bottom).

6.3 Results and discussion

6.3.1 Realization of a highly scattering rear Si surface texture by plasma etching

Figure 6-2 shows the reflectances measured in superstrate configuration on samples RST1 to RST4, before and after the plasma etching step. Only one reflectance curve before the plasma etching is shown, because the reflectances of all four samples were almost identical at this stage. As shown in Ref. [14], the reflectance interference amplitude range (AMP) at ~1500 nm wavelength (as shown in Figure 6-2) can be used as a gauge for the degree of light trapping. The initial AMP of the planar samples (RST1 - RST4) before the plasma etching step was 32%. A decreasing AMP of 20%, 9%, 4% and 2% corresponding to an increasing RF power of 400 W (sample RST1), 450 W (sample RST2), 500 W (sample RST3) and 550 W (sample RST4), respectively, is observed in Figure 6-2. A smaller AMP value indicates a higher scattering efficiency, which in turn results in better light trapping [14]. Hence, the Si rear surface of sample RST 4 after plasma etching has the highest scattering efficiency of the four investigated samples (RST1 - RST4).
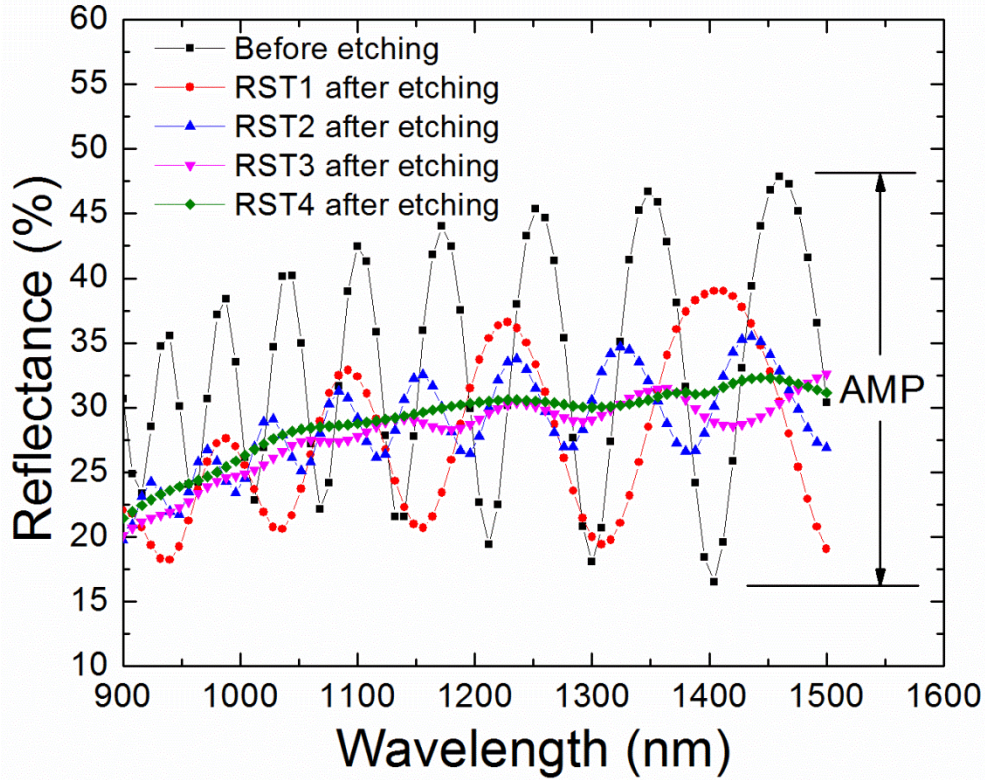
Figure 6-2: The reflectances measured in superstrate configuration of samples RST1 - RST4 before and after the plasma etching step. AMP stands for the interference amplitude range at around 1500 nm wavelength. The RF power of the plasma etching process was 400, 450, 500, and 550 W for samples RST1 - RST4, respectively.

6.3.2 SEM tilt view and cross-sectional view

Figure 6-3 shows the SEM 54° tilt view and cross-sectional view of sample RST4, whose plasma-etched texturization is highly randomising and has sharp tips. The poly-Si thickness of sample RST4 before the plasma etching was obtained by optical fitting, which is about 2400 nm. The poly-Si thin-film thickness of sample RST4 after the plasma etching based on SEM cross-sectional view (Figure 6-3(b)) is about 1900 nm. Thus, about 500 nm of poly-Si material was removed by the plasma etching process.
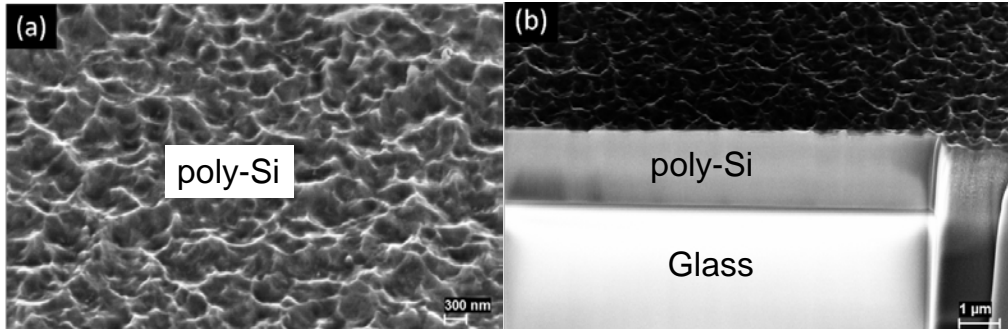
Figure 6-3: (a) SEM tilt view of sample RST4, (b) SEM cross-sectional view of RST4.

6.3.3 AFM measured height profiles of rear Si surfaces

Height profiles of the rear Si surfaces of the RST, AIT, and AIT + RST devices are shown in Figure 6-4. The rear Si surface of sample RST4 after the plasma etching step (Figures 6-4(a) and (b)) has an average feature size of 233 nm. The average feature size value is obtained by using the grain size analysis function of an AFM image processing software (Nanoscope, version 5.30). The surface RMS roughness is 43.7 nm. The autocorrelation length of the rear Si surface of sample RST4 after the plasma etching step is 1.2 µm. Figures 6-4(c) and (d) show the height profiles of the rear Si surface of sample AIT1 before the plasma etching. The lateral feature sizes are in the range of 1-3 µm. The RMS roughness and the autocorrelation length of the rear Si surface of sample AIT1 before the plasma etching was 113.5 nm and 3.0 µm, respectively. The height profile of sample AIT1 after the plasma etching represents the topography of the rear Si surface of the AIT + RST device (Figures 6-4(e) and (f)). The resulting surface has submicron features on top of micro-scale features. Hence, multi-scale texture features are produced. The RMS roughness of the multi-scale rear Si surface of sample AIT1 after the plasma etching step is 289.8 nm. The autocorrelation

111

length is 2.1 μm. One more AFM measurement on the rear Si surface of sample AIT1 after the plasma etching was done at a different location. The measured surface topography (image not shown here) is similar to that of Figures 6-4(e) and (f). The RMS roughness of 289.8 nm is much higher than the sum of the RMS roughness of Figures 6-4(a) and 6-4(c). The much higher achieved RMS roughness results from the fact that the dry plasma etching process started on a rough surface. The sidewalls of the rough surfaces in Figure 6-4(d) are covered with the used etch masking polymer ($Si_xO_yF_z$) and therefore are etched more slowly than the valleys [3]. The higher Si removal rate in the valleys of rough surfaces in Figure 6-4(d) results in steeper trenches, as shown in Figure 6-4(f). Hence, a much higher rear Si surface RMS roughness is produced for the AIT + RST device structure.
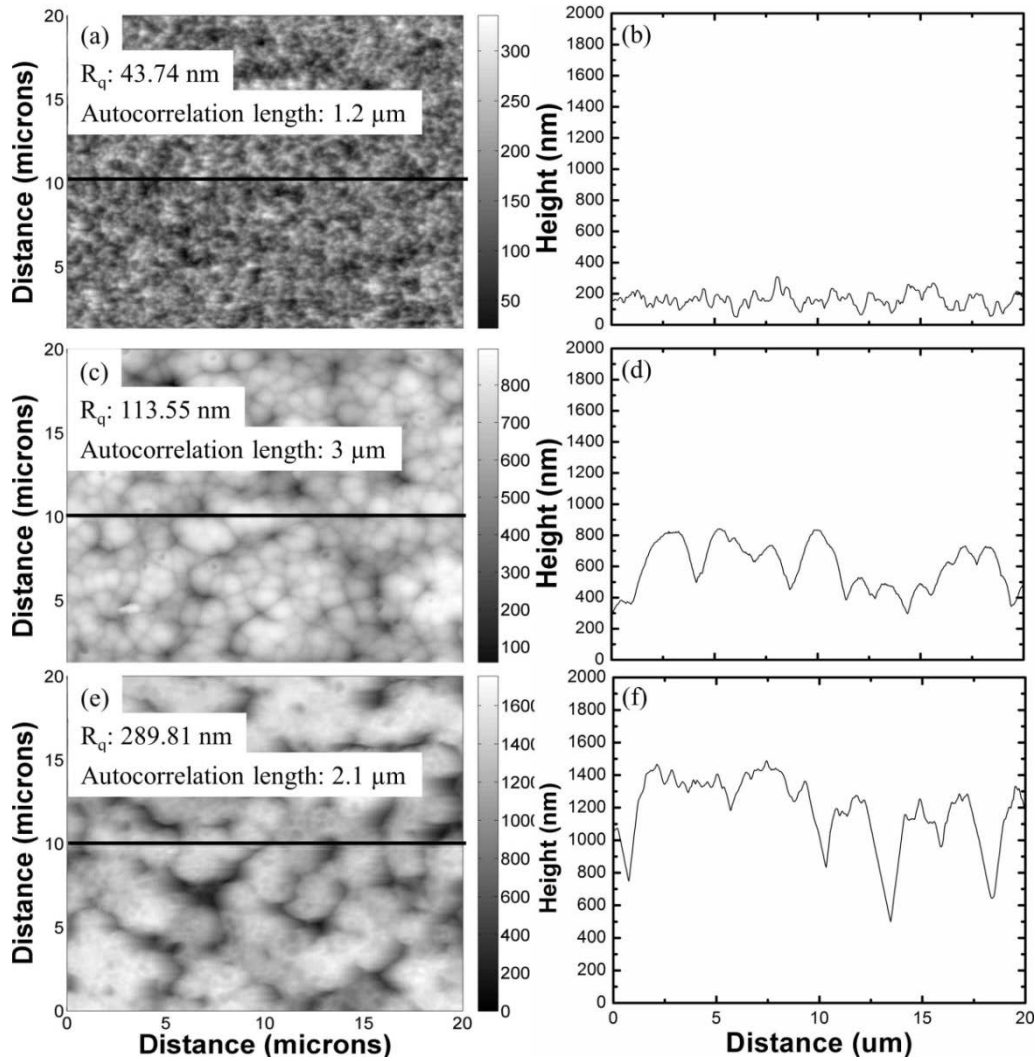
Figure 6-4: The AFM measured height profiles of the rear Si surface of (a): sample RST4 after plasma etching, (c): sample AIT1 before plasma etching, and (e): sample AIT1 after plasma etching. The black lines in (a), (c), and (e) are indications of cross sections. (b), (d), and (f) are their respective height profiles in two-dimensional cross-sectional views.

6.3.4 Haze and AID calculation based on the scalar scattering theory

The haze and AID values were calculated with the phase model presented in Refs. [15, 16], using the height data presented in Section 6.3.3. Figure 6-5(a) shows the calculated haze inside Si at the Si-air BSR interface, for the

113

wavelength range of 280-1100 nm. Figure 6-5(b) shows the calculated AID inside Si at the Si-air BSR interface for a wavelength of 800 nm. The haze and AID values were calculated based on the rear Si surface height data shown in Figure 6-4. Figure 6-5(a) shows excellent haze for rear Si surfaces of all three devices (RST, AIT, and AIT + RST). The haze of the rear Si surface of sample RST4 after the plasma etching step is above 95% across the wavelength range of 280-1100 nm. Figure 6-5(b) shows that at 800 nm wavelength the rear Si surfaces of the AIT and RST devices have similar AID, whereas the rear Si surface of the AIT + RST device scatters more light into larger angles. Based on the AID data in Figure 6-5(b) and using the method presented in Refs. [15, 17], we find that 50% of the light intensity is reflected at an angle larger than 29.2°, 30.3°, and 36.3° at the Si-air interfaces of the AIT, RST, and AIT + RST devices, respectively. Light reflected into larger angles has a longer optical path length in Si. Moreover, if the angle of reflection at the Si-air interface (θ as shown in the inset of Figure 6-5(a)) is greater than the critical angle θ_c of the Si-glass interface, total internal reflection (TIR) occurs at the Si-glass interface. At 800 nm wavelength the critical angle for TIR at the Si-glass interface is 23.4° according to Snell's law, using refractive indices of 1.47 and 3.7 for glass and Si, and assuming a planar glass surface. Based on the AID data in Figure 6-5(b) and using the method presented in Refs. [15, 17], the percentage of light intensities scattered with $\theta > 23.4°$ at the Si-air interface is 62%, 65%, and 72% for the AIT, RST, and AIT + RST devices, respectively. To summarize, the rear Si surface of the AIT + RST device has higher haze than its AIT and RST counterparts and that the rear Si surface of the AIT + RST device scatters more light more obliquely than its AIT and RST counterparts. Moreover, light has a higher chance of TIR at the Si-glass interface for the AIT + RST device than for the AIT and RST devices. Hence, we conclude

that the AIT + RST device with the multi-scale rear Si surface should have better

light trapping performance than its AIT and RST counterparts.
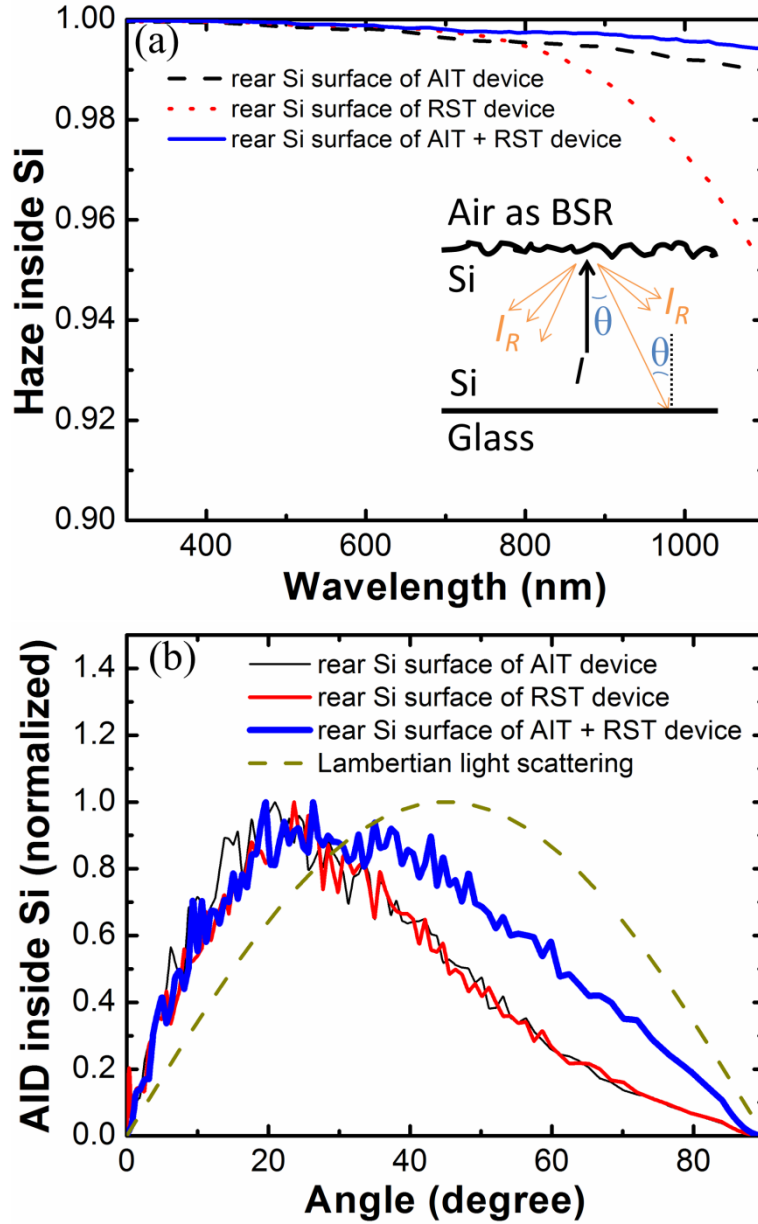
Figure 6-5: (a) Calculated haze inside Si and (b) normalized calculated angular intensity distribution (AID) inside Si at 800 nm wavelength. The haze and AID were calculated based on the height data of the Si rear surface of the RST device (Figure 6-4(a)), the AIT device (Figure 6-4(c)), and the AIT + RST device (Figure 6-4(e)). Light enters from the Si side and is reflected back into Si, as demonstrated in the inset of (a). The AID of a Lambertian light scattering surface is shown as a reference.

6.3.5 Measured absorptance and ASA simulated c-Si absorptance

Figure 6-6(a) shows the measured absorptance (*A*) of samples Planar1, RST4 after the plasma etching, and AIT1 before and after the plasma etching. Compared to sample Planar 1, absorptance is improved in NIR regions (600-1100 nm) for sample RST4 with plasma-etched rear Si surface texturization. Sample AIT1 before the plasma etching has higher absorptance in all wavelength regions than sample RST4 after the plasma etching. It indicates that the AIT glass texturing technique results in higher absorptance enhancement than the rear Si surface plasma-etched texturing technique, assuming the same c-Si absorber thickness.

Since sample AIT1 and sample RST4 went through an identical plasma etching process, the Si layer of sample AIT1 after the plasma etching is estimated to be 500 nm (26% of 1900 nm) thinner than before the plasma etching step. The measured absorptance of sample AIT1 before and after the plasma etching step are almost identical. This indicates that the AIT + RST device with 26% thinner Si layer can achieve comparable absorptance as the AIT device.

Figure 6-6(b) shows the ASA simulated c-Si absorptance of the AIT device with a 1900 nm thick c-Si absorber, and the AIT + RST device with a 1900 nm thick c-Si absorber. In all ASA optical simulations shown in Figure 6-6(b), air was used as the BSR. The AIT + RST device with the multi-scale rear Si surface texture can harvest more photons in the near-infrared wavelength range (700 - 1100 nm) than its AIT counterpart with the same c-Si absorber layer thickness. Boccard *et*

al. reported that multi-scale textures can also be beneficial for micromorph thin-film solar cells [18].

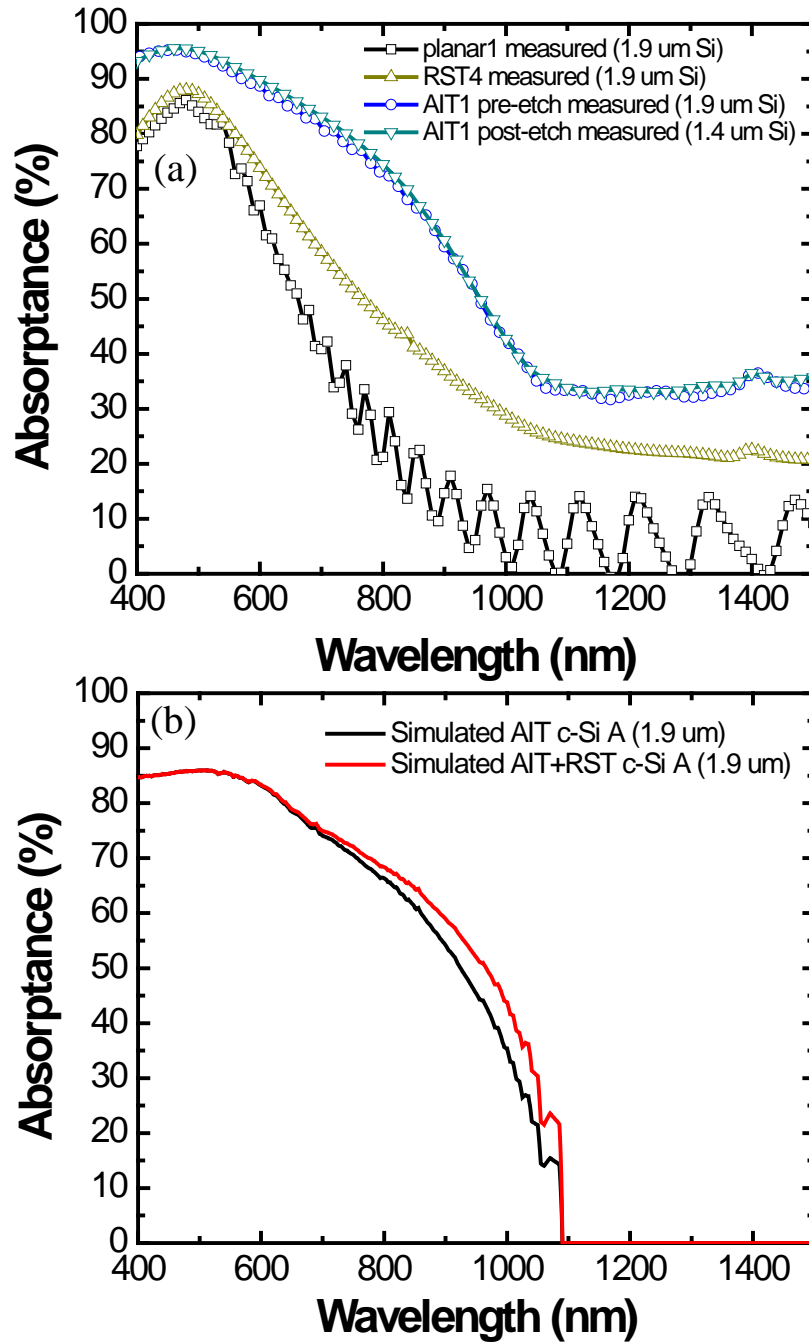Figure 6-6: (a): The measured absorptance of samples Planar1, RST4 after plasma etching, and AIT1 before and after plasma etching. Also shown are the simulated c-Si absorptance of (b) the AIT and AIT + RST devices. In all the simulations in this figure, air was used as the back surface reflector.

Current densities (J_{ph}) of the c-Si layers were calculated based on the simulated c-Si absorptances for the four devices (planar, RST, AIT, and AIT + RST) and two BSRs (a stack of SiO_2 and Al, and a stack of SiO_2 and Ag), assuming a 1900 nm thick poly-Si absorber layer. The calculated current densities are shown in Table 6-1. The AIT + RST device with a stack of SiO_2 and Ag as the BSR has the highest current density of 28.6 mA/cm^2. Current loss due to parasitic glass absorption is considered in these ASA optical simulations.

Table 6-1: Calculated J_{ph} of the four devices with two different BSRs are shown. Thicknesses of glass sheet, SiN_x, c-Si, SiO_2 and metal (Al and Ag) were set in ASA to be 3.3 mm, 70 nm, 1900 nm, 100 nm and 1000 nm. Also shows estimated solar cells efficiency for devices with SiO_2+Ag BSR assuming V_{oc} of 492 mV and FF of 72.1% (values of the 10.4% record cell by CSG).

Devices	Calculated J_{ph} for SiO_2+Al BSR	Calculated J_{ph} for SiO_2+Ag BSR	Estimated efficiency for SiO_2+Ag BSR
Planar	17.5 mA/cm^2	17.8 mA/cm^2	6.31%
RST	23.8 mA/cm^2	25.3 mA/cm^2	8.97%
AIT	26.0 mA/cm^2	27.2 mA/cm^2	9.65%
AIT + RST	27.2 mA/cm^2	28.6 mA/cm^2	10.15%

6.4 Conclusions

In this chapter, submicron textures for light trapping in poly-Si thin-film solar cells were produced and investigated. The textures were produced by SF_6/O_2 plasma etching of the rear Si surfaces. A phase model based on the scalar scattering theory was used to calculate the scattering properties (haze and angular intensity distribution) of the textured surfaces. The textured rear Si surface with the highest scattering efficiency shows over 95% reflection haze at the Si-air

interface. Multi-scale Si surface textures were produced by combining an etched texture at the rear surface of the silicon thin-film diode with a texture at the silicon-glass interface. Aluminium-induced texturing (AIT) was used to texture the glass surface onto which the diode was deposited. Three different systems were investigated: (i) solar cells deposited on planar glass with a rear Si surface textured by plasma etching (RST); (ii) solar cells deposited on AIT glass (AIT); (iii) solar cells deposited on AIT glass with a rear Si surface textured by plasma etching (AIT + RST). It was found that, by comparison, the multi-scale silicon texture of the AIT + RST system has the highest haze and scatters light into larger angles with higher efficiency. These characteristics indicate that the multi-scale texture should show very good light trapping properties. To simulate the performance of the poly-Si thin-film solar cells with the investigated textures, the implemented phase model was combined with the commercial thin-film simulator ASA. The method was also used to estimate the current generation that can be expected from the investigated textures on a 1900 nm thick poly-Si thin-film solar cell. Simulation results show that the multi-scale AIT + RST texture results in a current density of 28.6 mA/cm^2 for a solar cell with a high-quality SiO$_2$/Ag back surface reflector. This current density corresponds to a 5% improvement compared to a single-surface texture (AIT). We believe that the multi-scale texture presented in this chapter has potential to significantly enhance the current generation of actual solar cells. A functioning poly-Si thin-film solar cell with the multi-scale texture investigated here is yet to be realized. It seems worthwhile to further investigate the impact of the multi-scale texture on the PV efficiency of such cells.

References (Chapter 6)

[1] T. Soderstrom, Q. Wang, K. Omaki, O. Kunz, D. Ong, S. Varlamov, Light confinement in e-beam evaporated thin film polycrystalline silicon solar cells, Physica Status Solidi - Rapid Research Letters, 5 (2011) 181-183.

[2] D.S. Ruby, W.L. Wilbanks, C.B. Fleddermann, M.D. Rosenblum, S. Roncin, S. Narayanan, Optimization of plasma deposition and etching processes for commercial multicrystalline silicon solar cells, Proc. 25th IEEE Photovoltaic Specialists Conference, 1996, pp. 637-640.

[3] M. Schnell, R. Ludemann, S. Schaefer, Plasma surface texturization for multicrystalline silicon solar cells, Proc. 28th IEEE Photovoltaic Specialists Conference, 2000, pp. 367-370.

[4] O. Schultz, G. Emanuel, W. Glunz, G.P. Willeke, Texturing of multicrystalline silicon with acidic wet chemical etching and plasma etching, Proc. 3rd World Conference on Photovoltaic Energy Conversion, 2003, pp. 1360-1363 Vol.1362.

[5] D.H. Macdonald, A. Cuevas, M.J. Kerr, C. Samundsett, D. Ruby, S. Winderbaum, A. Leo, Texturing industrial multicrystalline silicon solar cells, Solar Energy, 76 (2004) 277-283.

[6] K.-S. Lee, M.-H. Ha, J.H. Kim, J.-W. Jeong, Damage-free reactive ion etch for high-efficiency large-area multi-crystalline silicon solar cells, Solar Energy Materials and Solar Cells, 95 (2011) 66-68.

[7] Y. Huang, N. Sahraei, P.I. Widenborg, I. Marius Peters, G.K. Dalapati, A. Iskander, A.G. Aberle, Enhanced light trapping in polycrystalline silicon thin-film solar cells using plasma-etched submicron textures, Solar Energy Materials and Solar Cells, 122 (2014) 146-151.

[8] H. Hidayat, A. Kumar, F. Law, C. Ke, P.I. Widenborg, A.G. Aberle, Impact of rapid thermal annealing temperature on non-metallised polycrystalline silicon thin-film diodes on glass, Thin Solid Films, 534 (2013) 629-635.

[9] H. Hidayat, P.I. Widenborg, A. Kumar, F. Law, A.G. Aberle, Static large-area hydrogenation of polycrystalline silicon thin-film solar cells on glass using a linear microwave plasma source, IEEE Journal of Photovoltaics, 2 (2012) 580-585.

[10] Y. Huang, P.I. Widenborg, A.G. Aberle, Up-scaling of the AIT glass texturing method to pilot line-scale borosilicate glass sheets, Proc. 26th EUPVSEC, Hamburg, 2011, pp. 2750-2753.

[11] Y. Huang, F. Law, P.I. Widenborg, A.G. Aberle, Crystalline silicon growth in the aluminium-induced glass texturing process, Journal of Crystal Growth, 361 (2012) 121-128.

[12] M.A. Villegas, J.M. Fernandez Navarro, Characterization and study of Na2O-B2O3-SiO2 glasses prepared by the sol-gel method, Journal of Materials Science, 23 (1988) 2142-2152.

[13] N. Shimodaira, K. Saito, A.J. Ikushima, T. Kamihori, S. Yoshizawa, VUV transmittance of fused silica glass influenced by thermal disorder, in: Proceedings of SPIE 4000, pp. 1553-1559 (2000).

[14] G. Jin, P.I. Widenborg, P. Campbell, S. Varlamov, Lambertian matched absorption enhancement in PECVD poly-Si thin film on aluminum induced textured glass superstrates for solar cell applications, Progress in Photovoltaics: Research and Applications, 18 (2010) 582-589.

[15] D. Domine, F.-J. Haug, C. Battaglia, C. Ballif, Modeling of light scattering from micro- and nanotextured surfaces, Journal of Applied Physics, 107 (2010) 044504.

[16] K. Jäger, M. Fischer, R.A.C.M.M. Van Swaaij, M. Zeman, A scattering model for nano-textured interfaces and its application in opto-electrical simulations of thin-film silicon solar cells, Journal of Applied Physics, 111 (2012).

[17] J.E. Harvey, C.L. Vernold, A. Krywonos, P.L. Thompson, Diffracted radiance: A fundamental quantity in nonparaxial scalar diffraction theory, Appl. Opt., 38 (1999) 6469-6481.

[18] M. Boccard, C. Battaglia, S. Hänni, K. Söderström, J. Escarré, S. Nicolay, F. Meillaud, M. Despeisse, C. Ballif, Multiscale transparent electrode architecture for efficient light management and carrier collection in solar cells, Nano Letters, 12 (2012) 1344-1348.

Chapter 7 Summary, original contributions, proposed further work

7.1 Summary

Light trapping is vital for PECVD deposited SPC poly-Si thin-film solar cells, mainly due to two facts: i) crystalline silicon is weakly absorbing in the NIR wavelength region; and ii) the absorber thickness is thin (usually 1-3 μm).

This thesis investigated advanced light trapping concepts for plasma-deposited SPC poly-Si thin-film solar cells on glass. An effective light trapping system involving elements investigated in this thesis is presented below. It is noted that the potential J_{SC} shown below was calculated for the AM1.5G spectrum in the wavelength range 280-1100 nm.

Table 7-1 summarises all light trapping elements investigated in this thesis and shows their respective contribution to the J_{SC} enhancement based on optical simulations with the ASA software. The thickness of the c-Si thin-film used in these simulations was 2.0 μm. The AFM measured height data of Chapter 6 were used in these ASA optical simulations.

Table 7-1: Light trapping elements investigated in this thesis and their respective contribution to the current enhancement. Also shown is the estimated solar cell efficiency assuming V_{oc} of 492 mV and FF of 72.1% (values of the 10.4% record cell by CSG Solar).

Light trapping element	Calculated 1-sun J_{SC} (mA/cm^2)	Relative J_{SC} enhancement	Estimated cell efficiency
No light trapping (poly-Si on planar glass with air BSR)	15.4	N.A.	5.46%
AIT glass texturing (element 1)	25.8 (with air BSR)	67.5 % (relative to planar)	9.15%
Glass thinning from 3.3 mm to 0.5 mm (element 2)	27.5 (elements 1 + 2 with air BSR)	6.6 % (relative to element 1)	9.76%
Rear Si surface texturing by plasma etching (element 3)	28.4 (elements 1 + 2 + 3 with air BSR)	3.0 % (relative to elements 1 + 2)	10.07%
A stack of SiO$_2$ and Ag as a high quality BSR (element 4)	31.0 (elements 1 + 2 + 3 + 4)	9.2 % (relative to elements 1 + 2 + 3)	11.00%

From the Table it can be seen that AIT glass texturing is the most important light trapping element, as it enhances the current by 67.5 % compared to a planar sample. The second-most important light trapping element is a high-quality BSR, which contributes a 9.2 % current enhancement. Thinning down the glass to 0.5

mm and applying a plasma-etched rear Si surface texture for poly-Si thin-film solar cells on AIT glass further enhances the current by 6.6 % and 3.0%, respectively. A 2 µm thick poly-Si thin-film solar cell on glass with all four light trapping elements implemented could achieve a remarkable 1-sun J_{SC} of 31.0 mA/cm^2. This value demonstrates that the light trapping system investigated and developed in this thesis has the potential for further improving the record current density (29.5 mA/cm^2) reported by CSG Solar for SPC type poly-Si thin-film solar cells on glass. A solar cell efficiency of 11% is achievable with the 31.0 mA/cm^2 J_{SC}, assuming 492 mV V_{OC} and 72.1% FF (V_{OC} and FF of CSG Solar's 10.4% record cell).

7.2 Original contributions

- Demonstration that the AIT glass texturing process can be scaled up with good optical uniformity.

- Development of a partially masked AIT process to create a planar bench-marking device on the same glass sheet.

- Systematic investigation of crystalline silicon growth in the AIT annealing process, and proposal of a phenomenological model of the AIT process.

- Demonstration of using a phase model to satisfactorily estimate haze and AID of textured surfaces in poly-Si thin-film cells on textured glass.

- Separate estimation of parasitic glass absorption and c-Si absorption by ASA optical simulations.

- Development of a plasma etching process to produce highly scattering rear Si surface textures.

- Demonstrate to apply the plasma-etched rear Si surface texture on poly-Si thin-film solar cells on AIT glass can enhance the current density by 3-5 %.

- Demonstration that the light trapping system investigated in this thesis has the potential to achieve over 30 mA/cm^2 current density.

7.3   Proposed further work

Presented below are some areas where the author believes further research efforts are warranted:

- The crystal quality of the silicon product of the redox reaction between aluminium and silicon dioxide can be further studied. It might be used as the seed layer for poly-Si growth.

- The impact of the plasma-etched rear Si surface texture on V_{OC} and *FF* of complete solar cells should be evaluated. The possible plasma damage resulting from the plasma etching process should be investigated. Additional treatments to minimize the plasma damage should be developed.

- Poly-Si thin-film solar cells on AIT glass with double diffusion barriers (silicon nitride and silicon dioxide) could be investigated by secondary ion mass spectrometry (SIMS) to study their impurity levels. More experiments could be carried out to further optimise the diffusion barriers and the control of the impurity levels.

List of publications arising from this thesis

Journal papers

[1] **Y. Huang**, N. Sahraei, P.I. Widenborg, I. Marius Peters, G.K. Dalapati, A. Iskander, A.G. Aberle, Enhanced light trapping in polycrystalline silicon thin-film solar cells using plasma-etched submicron textures, Solar Energy Materials and Solar Cells 122 (2014) 146-151.

[2] **Y. Huang**, F. Law, P.I. Widenborg, A.G. Aberle, Crystalline silicon growth in the aluminium-induced glass texturing process, Journal of Crystal Growth 361 (2012) 121-128.

Conference papers

[1] **Y. Huang**, P.I. Widenborg, A.G. Aberle, Up-scaling of the AIT glass texturing method to pilot line-scale borosilicate glass sheets, Proc. 26th EU PVSEC, Hamburg, 2011, pp. 2750 - 2753.

[2] **Y. Huang**, S. Chakraborty, P.I. Widenborg, A.G. Aberle, Rear surface texturing of polycrystalline silicon thin-film solar cells on glass using plasma etching, Tech. Digest, 22nd PVSEC, Hangzhou, 2012.